ARNE BRENDMO

AN INVESTIGATION OF WAVE-ENERGY ABSORPTION BY SINGLE AND DOUBLE OSCILLATING WATER-COLUMN CONVERTERS

NTH
UNIVERSITETET I TRONDHEIM
NORGES TEKNISKE HØGSKOLE

DOKTOR INGENIØRAVHANDLING 1995:2
INSTITUTT FOR FYSIKK
TRONDHEIM

An investigation of wave-energy absorption by single and double oscillating water-column converters

Arne Brendmo

January 11, 1995

Contents

Preface

This thesis is submitted to the University of Trondheim, The Norwegian Institute of Technology (NTH), Department of Physics, in partial fulfillment of the requirements for the degree of Dr.Ing.

The aim of this thesis is to present theory and some experiments concerning a wave energy converter consisting of two oscillating water columns. We want to investigate discrete phase control by means of controlled air valves. The main aims of such an investigation are to determine how much the power output can be increased due to the phase control, and in which way the air valves should be controlled in order to optimise the useful power.

We also want to determine hydrodynamic parameters characterising the system. Such parameters provide information of the system's ability to absorb wave energy, and they can also be used as a basis of time-domain simulation.

The experiments have been carried out at the Marine Technology Center (MTS), at the Norwegian Hydrotechnical Laboratory (NHL), and at the Department of Physics, NTH. These institutions are all situated in Trondheim. Financial support has been provided by the Research Council of Norway, Department for Scientific and Industrial Research.

I wish to thank my supervisor, professor Johannes Falnes, as well as Per M. Lillebekken and António J.N.A. Sarmento, for their kind help and good advice. I also wish to thank the staff at NHL, for practical assistance and loan of their wave flume.

List of symbols

When referring to complex functions which vary harmonical with time, we use the following notation: $\phi(x,y,z,t) = \hat{\phi}(x,y,z)e^{j\omega t}$. In most derivations all functions are harmonical, and the factor $e^{j\omega t}$ is then omitted. Nonharmonical functions are represented by their Fourier transform in the frequency domain. The Fourier transform is denoted with a tilde, like this: $\tilde{F}(\omega) = \mathcal{F}\{F(t)\}$. Complex conjugation is denoted by an asterisk (*) used as superscript.

The most frequently used symbols are presented in the following list. SI units are included in brackets. Note that the indices e,I, r,I and e, r describes excitation and radiation in the rigid-piston description and the applied-pressure description, respectively (see section 2.1.1).

$\hat{A}$	[m]	Complex amplitude of the incident wave at $x = 0$.
a^-	[m s/Pa]	Far field coefficient (eq. 3.20).
$a_{Q,n}$	[m^3/s]	Complex Fourier coefficients for a nonharmonic periodic volume flux (eq. 2.72).
$a_{p,n}$	[Pa]	Complex Fourier coefficients for a nonharmonic periodic pressure (eq. 2.71).
B	[m^3/(s Pa)]	Radiation susceptance = $Im\{Y\}$.
B_l	[m^3/(s Pa)]	Pneumaitic load susceptance for a linear power take-off (eq. 5.20).
D		$= D(kh)$ = depth function (eq. 2.3).
d	[m]	Flume width.
$e(kz)$		Vertical eigenfunction, incident wave (eq. B.3).
$\eta_{d,I}$	[m]	Diffracted wave in terms of the rigid-piston description (eq. 2.1).
η_i	[m]	Incident wave.
η_{nf}	[m]	Near-field part of the radiated wave in terms of the rigid-piston description (eq. 4.1).
$\eta_{r,I}$	[m]	Radiated wave in terms of the rigid-piston description (eq. 2.1).
η_s	[m]	Reflected wave, including radiated wave (eq. 2.1).
F	[N]	Hydrodynamical force (eq. 2.5).
$F_{e,I}$	[N]	Excitation force (eq. 2.5).
$F_{r,I}$	[N]	Radiation force (eq. 2.5).
F_{tot}	[N]	Total force (eq. 5.1).
f	[Hz]	Frequency.
$f_{e,I}$	[Ns/m]	Excitation force coefficient (eq. 2.5).
$f_{e1,I}$	[Ns/m]	Excitation force coefficient for chamber no. k, where $k = 1, 2$.

G	[$m^3/(s\,Pa)$]	Radiation conductance = $Re\{Y\}$ (eq. 2.2).
G_l	[$m^3/(s\,Pa)$]	Pneumatic load conductance for a linear power take-off (eq. 5.20).
G_{nl}	[$m^3/(s\,Pa)$]	Pneumatic load conductance for a nonlinear power take-off (eq. 2.73).
g	[m/s^2]	Acceleration of gravity.
h	[m]	Flume depth.
h_d	[$m^3/(s\,Pa)$]	Diagonal element of the step response matrix of a twin OWC (eq. 3.3).
h_x	[$m^3/(s\,Pa)$]	Cross element of step response matrix of a twin OWC (eq. 3.3).
J	[W/m]	Wave energy transport (eq. 2.4).
j		Imaginary unit = $\sqrt{-1}$.
k	[rad/m]	Angular repetency (wave number).
k		As subscript: chamber number.
λ	[m]	Wavelength.
Λ	[$m^3/(s\,Pa)$]	Pneumatic load admittance (eq. 2.70).
$m_{r,I}$	[kg]	Added mass (eq. 2.6).
p_a	[Pa]	Atmospheric pressure.
p_k	[Pa]	Dynamic air pressure in chamber no. k, where $k = 1, 2$.
P	[W]	Absorbed power.
P_e	[W]	Excitation power according to the applied pressure model (eq. 2.17).
$P_{e,I}$	[W]	Excitation power according to the rigid piston model (eq. 2.8).
P_r	[W]	Radiation power according to the applied pressure model (eq. 2.18).
$P_{r,I}$	[W]	Radiation power according to the rigid piston model (eq. 2.9).
Q	[m^3/s]	Total volume flux (eq. 2.13).
Q_1	[m^3/s]	Volume flux at the interior surface in chamber 1.
Q_2	[m^3/s]	Volume flux at the interior surface in chamber 2.
Q_{c1}	[m^3/s]	Total volume flux in to chamber 1 (eq. 3.18).
Q_{c2}	[m^3/s]	Total volume flux in to chamber 2 (eq. 3.18).
Q_e	[m^3/s]	Excitation volume flux (eq. 2.14).
Q_r	[m^3/s]	Radiation volume flux (eq. 2.15).
Q_{v1}	[m^3/s]	Volume flux through valve no. 1 (eq. 2.74).
Q_{v2}	[m^3/s]	Volume flux through valve no. 2 (eq. 2.75).
q_e	[m^2/s]	Excitation volume flux coefficient (eq. 2.14).
q_{e1}	[m^2/s]	Excitation volume flux coefficient for chamber no. k, where $k = 1, 2$.
R_f	[Ns/m]	Hydrodynamic mechanical loss resistance(*eq.* 4.14).
$R_{r,I}$	[Ns/m]	Radiation resistance (eq. 2.9).
ρ	[kg/m^3]	Mass density of water.
ρ_a	[kg/m^3]	Mass density of air.

S	[m^2]	Sum of the areas of the water surfaces in the two chambers.
S_k	[m^2]	Area of interior water surface no. k, where $k = 1, 2$.
S_h	[kg/s^2]	Hydrostatical stiffness (section 5.1).
s	[m]	Excursion of interior water surface for a single OWC.
s_k	[m]	Excursion of interior water surface in chamber no. k, where $k = 1, 2$.
T	[s]	Wave period.
T_{reg}	[s]	Registration time length.
t	[s]	Time.
u_k	[m/s]	Vertical velocity of water column no. k, where $k = 1, 2$.
$X_{r,I}$	[Ns/m]	Radiation reactance (sec. 5.1).
x	[m]	Distance along the direction of wave propagation.
Y	[$m^3/(s\,Pa)$]	Radiation admittance of a single OWC (eq. 2.15).
Y_d	[$m^3/(s\,Pa)$]	Diagonal element of radiation admittance matrix (section 2.1.3).
Y_x	[$m^3/(s\,Pa)$]	Cross element of radiation admittance matrix (section 2.1.3).
y_d	[m^3/Pa]	Diagonal element of impulse response matrix (eq. 3.2).
y_x	[m^3/Pa]	Cross element of impulse response matrix (eq. 3.2).
Z_w	[Ns/m]	Radiation impedance incl. mechanical loss resistance (eq. 4.17).
Z_d	[Ns/m]	Diagonal element of the radiation impedance matrix.
Z_l	[Ns/m]	Mechanical load impedance (eq. 5.1).
Z_m	[Ns/m]	Mechanical impedance (section 5.1).
$Z_{r,I}$	[Ns/m]	Radiation impedance (eq. 2.5).
Z_x	[Ns/m]	Cross element of the radiation impedance matrix.
ω	[rad/s]	Angular frequency.

Abstract

In this work we have performed two series of experiments considering a system of two oscillating water columns (OWCs). The system is a 1:10 scale model, where full scale means physical dimensions equal to a test plant built by the company Kværner Brug at Toftestallen on the west coast of Norway.

One of the experimental series was an attempt of phase-controlling the system in regular incident waves. The phase control was discrete and accomplished by means of controllable air valves. The instants for opening and closing of the air valves have been varied from run to run, in order to find an optimum control strategy, providing maximum useful power conversion. It was also of great interest to determine to what extent the useful power could be increased by means of the phase control, compared to a single OWC of the same physical dimensions, but with no phase control. The results from these experiments suggest a control strategy which seems to be satisfactory. A relative power increase of a factor 3 and a factor 1.7 has been achieved for wave periods of 3.0 s and 3.5 s, respectively. The resonance period of the system is approximately 2.1 s. However, because of problems with experimental reproducibility, we do not know whether the control has been optimum. It has also been impossible to determine to what extent small changes of the control instants have affected the power output.

The other experimental series regarded a transient wave radiating from the OWC model. From these experiments the impulse response matrix of the system has been calculated. This matrix has in turn been used to determine frequency domain hydrodynamic parameters, and also, to define the basis of a time-domain mathematical model of the system. Such a model makes it possible to simulate the system in the time domain.

In addition to the experiments mentioned above, there have also been performed experiments considering a single two-dimensional OWC in scale 1:30. The purpose of these experiments has been to determine the amount of linear power loss associated with friction in the water, as well as the loss resistance describing these losses. The experiments have been carried out in two parts, one considering regular incident waves, and the other considering a transient outgoing wave. The power loss for this model has been found to be in the range of 13 - 20 % of the incident wave power, and the loss resistance has been found to be in the range of 2.5 - 5.0 Ns/m.

The work in this thesis also includes derivation of equivalent diagrams, serving as simplifyed description models of the hydrodynamics of a single OWC. Such equivalents are presented both in terms of mechanical and analog electric elements. It has also been an aim to investigate how the loss parameters found in the small-scale experiment may be implemented in an equivalent diagram based on the applied-pressure description model. A computer program has been written, utilising one of these equivalents. The hydrodynamical parameters computed by means of this program seem to be in reasonable agreement with experimental results.

Chapter 1

Introduction

1.1 Historical survey

Wave energy converters (WECs) can be roughly divided into three groups: Point absorbers, attenuators and terminators. Point absorbers are devices which are small compared to one wavelength. Typical for such devices is that the energy capture width may be larger than the physical dimensions of the absorber. The frequency response of a point absorber has typically a sharp resonance maximum and a narrow bandwidth. A power plant based on point absorbers should consist of a large number of units.

Contrarily, a WEC may consist of a floating or fixed structure with a length comparable to, or larger than one wavelength. If such a construction is aligned in the direction of wave propagation, it is termed an attenuator. A terminator is a large construction placed parallel to the prevailing wave front. Terminators and attenuators have a broad bandwidth.

The primary power take-off of a WEC is usually due to the interaction between the waves and some kind of oscillating system. Such a system may be a rigid body, e.g. a buoy, or it may simply consist of a partly enclosed volume of oscillating water. In the latter case, an amount of air may be entrapped above a water volume in a chamber which is open towards the sea some distance beneath the sea surface. The incoming wave will then force the body of water to oscillate, making it possible to pump air through a turbine. Such a device is said to be a WEC of the OWC type, where OWC stands for *oscillating water column.* In terms of the classification above, an OWC of the size considered here may be regarded as a point absorber.

The idea of utilising the energy in ocean waves is not a new one. Proposals for how this could be done, was presented already in 1799 by Girard & Girard [1]. In 1892, A.W.Stahl wrote an extensive paper considering utilisation of ocean wave energy [2]. A paper issued in 1976 by NEL in Scotland [3], giving a survey of the development in this field, mentions 340 British patents for WECs in the period between 1856 and 1973. The first known OWC which produced useful power, was a device made in 1910 by boring a vertical hole in a cliff on the coast of France [4].

OWCs are among the most commonly known types of wave energy converters. The popularity of the OWC is mainly due to its mechanical and structural simplicity. An OWC may be enclosed in a floating structure as well as in a fixed structure sited on

shore. The former concept has been proposed by Masuda [5], and also by research groups in Belfast [6] and at NEL, Scotland [7]. Using a floating structure implies several advantages. Firstly, the OWC may be located off-shore where it is exposed to larger waves, and hence, it will produce more power than a plant close to the shore. Secondly, a device of this type will usually withstand the severe forces from a heavy storm better than a fixed structure. Also, such WECs may be mass-produced in a shipyard and towed to their location, thereby reducing the costs of construction.

Since the first attempt in 1910, more modern OWC designs have been proposed in several countries. Resonant OWC devices were proposed in France in 1952 [8] and in Norway in 1974 [9]. Also in the UK [10], Ireland [11], Portugal [12], and Japan [13], such devices have been investigated for some time.

Most OWCs investigated until today have been fixed structures sited on or close to the shore. There may be several reasons for prefering this approach. One obvious advantage, especially during the phase of research and development, is that a shore-based plant is easily accessible for inspection and maintanance. Moreover, the transmission of useful electric energy will not demand an expensive sea cable.

During the last decade, research on shore-sited OWCs has been performed in Japan [13], Norway [14], India [15] and China [16]. At present, prototypes of OWC power plants are being tested in Japan [13,17], India [18], China [19] and UK [20]. Besides, an EU wave energy research program is in progress, where OWCs form part as an important subject [21].

In the 1970s Masuda [22] proposed a double-chamber OWC with non-return valves providing rectification of the air flow through the turbine. However, the invention of self-rectifying turbines, e.g. the Wells turbine [23], has made WECs of the OWC type possible without rectifying air valves. For this reason, almost all research on OWCs during the last decade, has been concentrated on single OWCs with Wells turbines.

In 1985 the Norwegian company Kværner Brug built a full-scale prototype power converter of the single-OWC type, equipped with a self-rectifying turbine of the Wells type and a generator of 500 kW installed power [14,24,25]. The power plant was shore-located at Toftestallen 40 km north-west of Bergen, and was operable until it was damaged in a storm in December, 1988. The horizontal cross-section of the chamber was approximately triangular, with dimensions 10 m perpendicular to the incident wave, and 10 m in the longitudinal direction. The cross-sectional areas at the chamber mouth and at the interior water surface, were not equal, but 35 m^2 and 50 m^2, respectivily. This may have caused undesired velocity gradients, and hence, increased power losses. Measurements on this prototype have indicated that an optimal air turbine should have a load conductance in the range of 2.5 - 10 $m^3/(s\,kPa)$ [14]. The overall experiences from this power plant emphasised the need for further development of OWC systems.

The effective bandwidth of a WEC can be increased by use of *phase control*, that is, control of the phase of the WEC's oscillatory motion relative to the phase of the incident wave, in order to maximise the energy output. Such control may be realised by means of a continuously adjustable complex load admittance [26]. In this report, an alternative method is presented, namely discrete control realised by trying to stop the oscillatory motion during parts of the oscillation period. This method is commonly termed the *latching* principle, although an OWC is not completelty latched due to air compliance.

Phase control of OWCs using latching, has been considered since the early 1980s [27] - [32]. The latching is carried out by opening and closing an air valve between the chamber and the atmosphere. Hence, a phase lag is introduced as the water column is temporarily held back. For a single OWC, the latching valve is placed in series with a self-rectifying air turbine. The flow of air through the turbine will then be stopped when the valve closes. This may however have disadvantageous effects on the turbine efficiency [32]. For this reason, Budal proposed [33] to use a two-chamber system similar to the system proposed by Masuda [22], but equipped with controlled valves instead of non-return valves. A phase-controlled system of this type, is the main subject for new investigation in the present thesis.

In addition to an optimum phase of the oscillations, there also exists an optimum amplitude, ensuring a maximum power absorption from the incident wave. As we shall see, however, it may not be economically advantagous to satisfy this last condition at all times.

The hydrodynamic theory of OWCs was at first directly adopted from the theory describing rigid bodies in heave. The interior water surface may then be regarded as a massless rigid piston, and the inertia of the water of the OWC is included in the hydrodynamic added mass. Hence, the system is described in terms of the excitation force on, and the oscillation velocity of the interior surface. This description is often refered to as the rigid-piston model. In this thesis we will also use the term *model I.*

Later, a more correct hydrodynamic theory was developed by Sarmento and Falcao, [12] and by Evans [34]. In this theory the hydrodynamics is described in terms of the dynamic air pressure in the chamber and the excitation volume flux, that is, the volume flux by the air-displacing interior water surface, due to the incident wave when the dynamic air pressure is zero. Assuming that the wavelength is large compared to the horizontal dimensions of the OWC, which is true for the experiments described in this report, these two approaches are approximately equivalent. Hence, a problem may be converted from one model to another, interchanging the hydrodynamic variables [35]. In this report, the latter approach, termed the applied-pressure model, or simply *model II*, is preferred when analysing most of the experiments.

1.2 The principles of single and twin OWCs

The physical operation of a single OWC with no phase control is assumed to be well known. Besides, a detailed description of this subject is included in the theory presented in chapter 2. We shall, however, already at this point emphasise some of the features concerning phase control of OWCs in general, and the principles of twin OWCs in particular. Only a brief principle outline is included here, while theoretical details are postponed to the later chapters.

As already mentioned in section 1.1, an oscillating device interacting with an ocean wave may be phase-controlled by holding back the device in parts of the wave period. For the case of a single OWC, this is achieved by means of an air valve in series with the power-converting air turbine. Closing the turbine will slow down, but not entirely stop the oscillatory motion of the water column. The reason for this is partly the compressibility

of the air in the chamber, and partly possible leakage of air.

Considering a regular incident wave, a successful phase control of the OWC may turn out something like sketched in figures 1.1 and 1.2. The figures show an assumed case, where the normalised excitation force is compared to the excursion and vertical velocity of the water surface in the chamber. As shown in the figure 1.2, the phase-controlled OWC have a vertical velocity which, in average, is in phase with the excitation force.

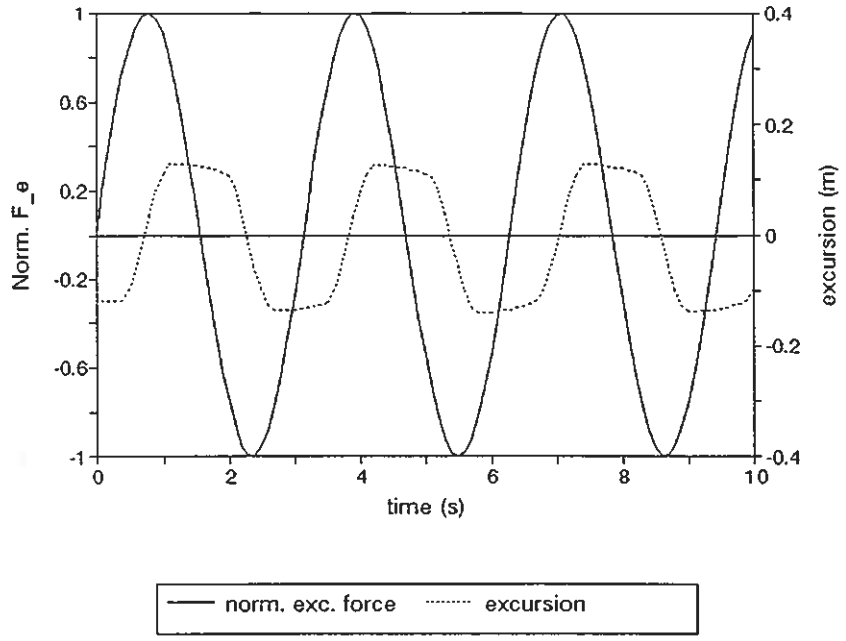

Figure 1.1: Assumed single OWC with phase control. The normalised excitation force and the excursion of the interior water surface are shown as functions of time.

Moving on to a double-chamber OWC, two separate air valves may be utilised, and the air turbine is placed between the chambers. As mentioned in section 1.1, such a modification have earlier been made in order to rectify the air flow through the turbine [22]. This principle is presented in figure 1.3. Since the two valves are passive check valves letting through the air in opposite directions, one of them will open when the water surfaces are rising, and the other will open when the surfaces are dropping. The small arrows in figure 1.3 show the direction of the water surface motion, while the larger shaded arrows represent the direction of air flow.

In the present work we will use valves not only for rectification, but also for phase control. The valves shown in figure 1.3 will thus be opened and closed by means of a control system. The decisions of when the valves should be operated, will be based on information on the phase of the incident wave. Hence, the optimum operation indicated for the case of a single OWC in figures 1.1 and 1.2, will be generalised to a twin-chamber system. The conditions for optimum operation of the air valves will of course be more complicated in such a case. This issue is explained and discussed in detail in the following chapters (see e.g. figure 2.19 in section 2.2.3).

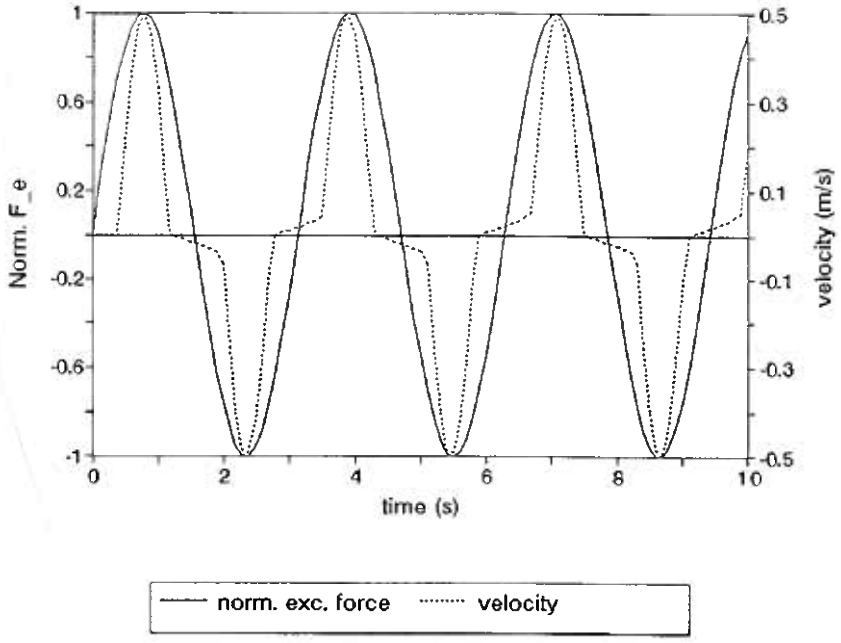

Figure 1.2: Assumed single OWC with phase control. The normalised excitation force and the vertical velocity of the interior water surface are shown as functions of time.

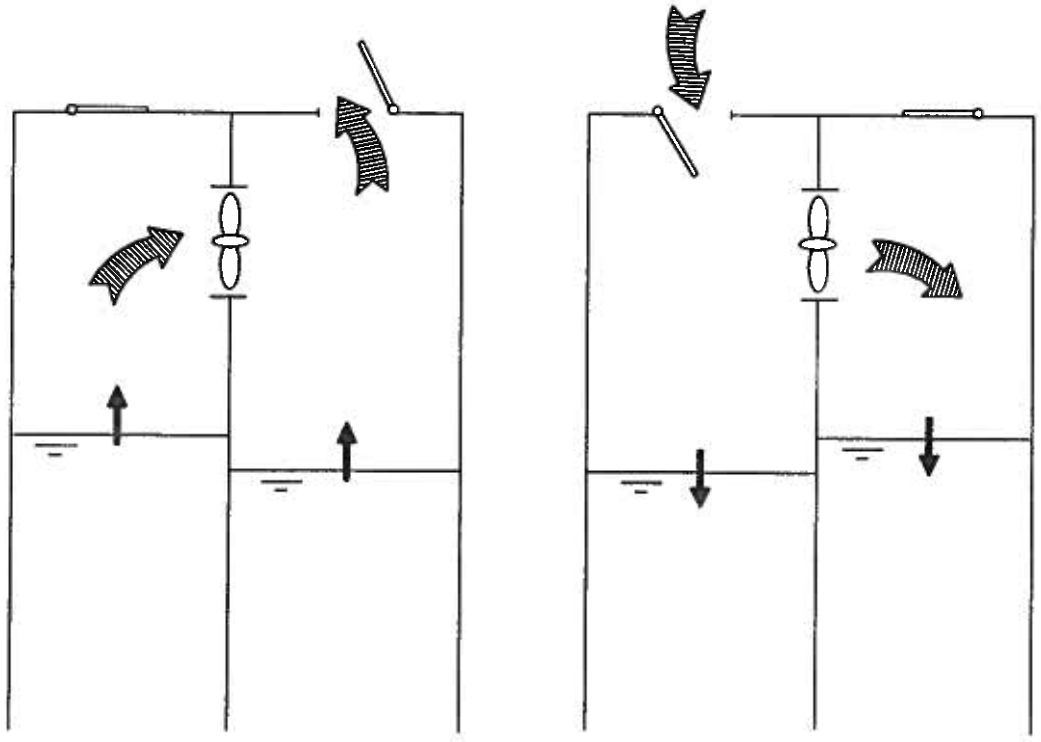

Figure 1.3: Principle of twin OWC with non-return valves: a) rising water level, b) dropping water level.

1.3 Outline of the following chapters

The work presented in this thesis is devided in four separate parts. Each part is described in the chapters 2 to 5.

In chapter 2 we consider a regular incident wave towards a twin-OWC model in scale 1:10, equipped with operable air valves for phase control. In the first part of the chapter, the theoretical basis is presented, as well as an outline of the two hydrodynamical description models mentioned above. Further, the conditions for optimum power absorption is derived, and the phase control of OWCs by means of latching, is described. Theory concerning power take-off is also presented.

After the theory follows a description of the actual experiments and the corresponding results. One purpose of these experiments has been to find an efficient control strategy for the system. It should be noted that the load of an OWC system may be of different types, some linear and some nonlinear. In this work we have used orifices, which are nonlinear elements. As a result, the radiated waves contain higher harmonics, and also, the load conductance is dependent on the instantaneous values of the chamber pressures. However, some of the analysis regarding the power take-off is based on linear theory, in order to allow an easy comparison of the single-chamber case and the twin-chamber case. These specific results should be considered merely as rough approximations. The obtained results are discussed in the last part of the chapter.

Chapter 3 describes a series of experiments considering a transient wave radiated *from* the model. As in the previous chapter, the theory involved is presented in the first part. The presentation includes a description of a time-domain simulation model, based on impulse response functions which has been obtained by means of these experiments.

Afterwards follows a description of the experiments, and it is explained how the transient wave is created by means of a pressure step inside one of the chambers.

Then the obtained results are presented, including hydrodynamic parameters describing the system in the frequency domain, and also, the impulse response functions constituting the basis of the time-domain mathematical model. A discussion of this work concludes the chapter.

Chapter 4 describes a set of experiments which consider a two-dimensional problem, performed in scale 1:30. The main purpose of this work has been to determine viscous losses. The structure of this chapter is similar to the two above mentioned: first there is a short outline of the theory concerning this work, then the experiments and results are presented, followed by a brief discussion.

The work presented in chapter 5 concerns a phenomenological description. It describes a method of simplifying the dynamics of a single OWC, by replacing it by an equivalent diagram. Such a diagram consists of a mechanical oscillating system or an analog electric curcuit, symbolising the real dynamic parameters involved. Equivalent diagrams are developed for both the rigid-piston model and the applied-pressure model. A computer program is developed, based on one of these equivalents. Output from this program shows reasonably good agreement with experimental data.

Chapter 2

Incident wave experiments

In this chapter the twin OWC model is exposed to regular incident waves, and the system is phase controlled by means of operable air valves. The objective of the experiments has been to determine the instants for valve operation which provides maximum useful power. In this work we have calculated the pneumatic power, and compared it to corresponding results from a single OWC without phase control.

2.1 Theory

2.1.1 The hydrodynamics of OWCs

An OWC consists of a chamber where a volume of air is enclosed above the sea surface. The chamber is open towards the sea some distance beneath the water surface. In most cases, useful energy is produced by means of an air turbine, which is placed between the air chamber and the outer atmosphere. An incident wave will force the water column below the air to oscillate, and hence, air is pumped through the turbine (see figure 2.1).

The air flow through the turbine will change direction as the chamber pressure oscillates. For this reason, it is convenient to use a self-rectifying air turbine, e.g. the Wells turbine [23]. A conventional turbine may be more efficient, but will demand the air to be rectified by means of mechanical valves [7,22].

If the horizontal dimensions of the OWC is small compared to the typical wavelength at the actual site, the construction can be regarded as a point absorber. In this paper, only water columns of this size are considered.

Assuming a regular incident wave $\eta_i(x,t)$ with a complex amplitude $\hat{\eta}_i(x,\omega)$, where ω is the angular frequency, we define $\hat{A}(\omega) \equiv \hat{\eta}_i(0,\omega)$. Here, x is the coordinate along the direction of wave propagation, and $x = 0$, i.e. the origin, is chosen to be at the front wall of the OWC model.

The wave reflected from the OWC may similarily be defined

$$\hat{\eta}_s(x,\omega) = \hat{\eta}_{d,I}(x,\omega) + \hat{\eta}_{r,I}(x,\omega) \tag{2.1}$$

where $\hat{\eta}_{d,I}(x,\omega)$ denotes the complex amplitude of the diffracted wave, that is, the reflected wave when the OWC is held fixed. Consequently, $\hat{\eta}_{r,I}(x,\omega)$ is the radiated wave, i.e. the contribution due to the water excursion in the chamber. The index I refers to the

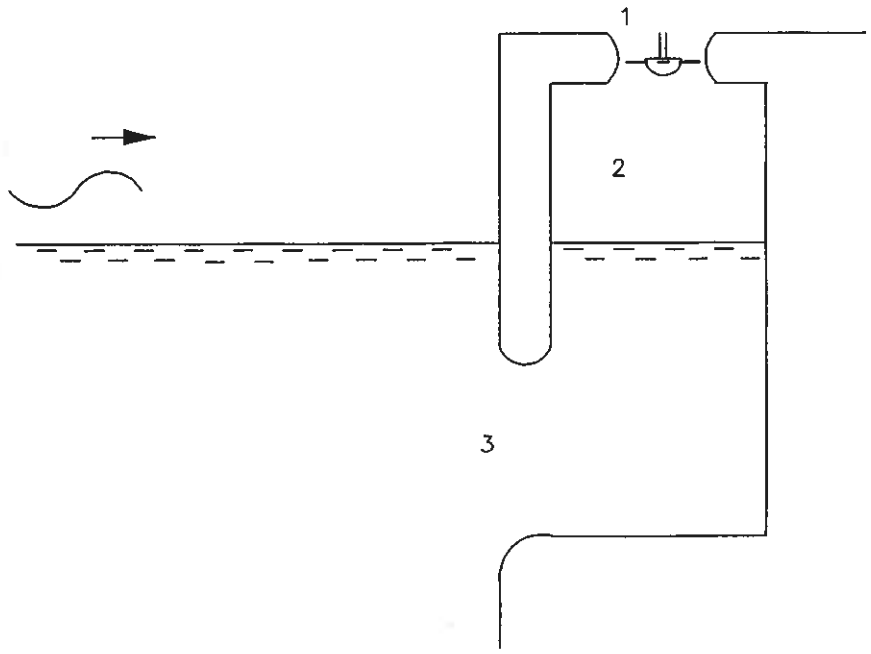

Figure 2.1: A single OWC. *1. turbine, 2. air chamber, 3. mouth.*

hydrodynamical description used in this case (model I). This is explained later in this section.

In the present work we shall refer all waves to the origin ($x = 0$). The coordinate x will hence be omitted from the notation. However, the radiated wave, and hence, the reflected wave, will contain evanescent wave modes in addition to the propagating wave. This is commonly refered to as the *near field* of the radiating device. To avoid interference from these modes, the reflected wave and the radiated wave have to be determined from measurements some distance from the OWC model, and not at the origin. Hence, the phase of these waves have to be corrected correspondingly.

In the following outline of theoretical results, it is assumed that linear theory is applicable. All oscillating variables are represented using complex notation. Then the time-dependent factor $e^{j\omega t}$ may be omitted in linear expressions, and sinusoidally varying variables may be represented by their complex amplitudes. For quantities which are non-sinusoidal, the complex amplitude should be replaced by the Fourier-transform of the quantity. For the sake of readability, dependence on ω is not shown explicitly in formulas.

The power which is absorbed from the waves by an OWC may be expressed as

$$P(\omega) = \frac{d\rho g^2 D}{4\omega}(|\hat{A}|^2 - |\hat{\eta}_s|^2) \tag{2.2}$$

where $D = D(kh)$ is the *depth function*, defined by the relation

$$D(kh) = \tanh(kh) + \frac{kh}{\cosh^2(kh)} \tag{2.3}$$

Here, k is the angular repetency (wave number), which satisfyes the dispersion equation: $\omega^2 = gk\tanh(kh)$. Further, d is the flume width, h is the water depth and g is the acceleration of gravity.

We also introduce the incident *wave energy transport*, which is the incident wave power per unit width of the wave front:

$$J(\omega) = \frac{\rho g^2 D}{4\omega}|\hat{A}|^2 \tag{2.4}$$

The absorbed power may be expressed in terms of the excitation force and the oscillation velocity of the internal water surface. Such a description was originally derived to describe the oscillitary motion of a rigid floating body [36]. However, if we regard the water surface inside an OWC as a massless, rigid piston, this model does apply also in the case of OWCs, although only as an approximation. This approximation is valid if the wavelength is large compared to the horizontal extension of the interior surface, which is true in the case of a point absorber. The rigid-piston description is based on the expression [37,38]:

$$\hat{F} = \hat{F}_{e,I} + \hat{F}_{r,I} = f_{e,I}\hat{A} - Z_{r,I}\hat{u} \tag{2.5}$$

Here, $F_{e,I}(\omega)$ is the *excitation force*, that is, the force on the OWC from the incident wave, when the OWC is held fixed. Hence, $F_{r,I}(\omega)$ is the *radiation force*, due to the oscillatory motion of the OWC. The generally complex proportionality coefficient $f_{e,I}(\omega)$ is termed the *excitation force coefficient* (defined by the expression $\hat{F}_{e,I} = f_{e,I}\hat{A}$). Further, $Z_{r,I}(\omega)$ is the *radiation impedance*, constituting a complex proportionality coefficient between the radiation force and the complex velocity amplitude $\hat{u}(\omega)$ of the excursion of the envisaged rigid piston. The radiation impedance may be written

$$Z_{r,I} = R_{r,I} + j\,X_{r,I} = R_{r,I} + j\omega m_{r,I} \tag{2.6}$$

The real part $R_{r,I}(\omega)$ is here termed the *radiation resistance*, while the imaginary part $X_{r,I}(\omega)$ is termed the *radiation reactance*. Further $m_{r,I}(\omega)$ is frequently referred to as the *hydrodynamical added mass* of the system.

In terms of this description, the absorbed may be expressed as

$$P = \overline{u\,F} = P_{e,I} - P_{r,I} \tag{2.7}$$

Hence,

$$P_{e,I} = \overline{u\,F_{e,I}} = \frac{1}{2}|\hat{u}||\hat{F}_{e,I}|\cos\beta \tag{2.8}$$

and

$$P_{r,I} = \overline{u\,F_{r,I}} = \frac{1}{2}R_{r,I}|\hat{u}|^2 \tag{2.9}$$

Consequently, $P_{e,I}(\omega)$ and $P_{r,I}(\omega)$ are the *excitation power* and the *radiated power* defined in terms of the rigid-piston description (model I). The bars above the expressions denote time averaging, and β is the phase difference between the excursion velocity of the OWC and the excitation force. The above expressions imply that the absorbed power is maximum when $\beta = 0$, that is, when the velocity of the water surface excursion in the chamber is in phase with the excitation force. This is the *optimum phase condition*, and

it corresponds to the situation when the system is in resonance. When this condition is satisfied, the absorbed power becomes

$$P = \frac{1}{2}\left(|\hat{u}||f_{e,I}\hat{A}| - R_{r,I}|\hat{u}|^2\right) \tag{2.10}$$

This expression shows that P is a parabolic function of $|\hat{u}|$, with a maximum value

$$P_{max} = \frac{1}{2}R_{r,I}|\hat{u}|^2_{opt} \tag{2.11}$$

provided that

$$|\hat{u}|_{opt} = \frac{|f_{e,I}\hat{A}|}{2R_{r,I}} \tag{2.12}$$

Equation (2.12) is called the *optimum amplitude condition.*

One reason for using the rigid-piston description, is that it provides an easy visible check of the phase and amplitude conditions. Firstly, if the phase condition is satisfied, the excitation force is in phase with the oscillation velocity of the water column ($\beta = 0$ in equation (2.8)), and secondly, the velocity amplitude of the interior water surface is always 90° out of phase with the excursion amplitude $\hat{s}(\omega)$ ($\hat{u} = j\omega\hat{s}$). Thus, since the excitation force on a OWC in a reflecting wall is in phase with the incident wave, we can tell that the phase condition is fulfilled if the elevation in the chamber is lagging the incident wave with a quarter of a period.

Furthermore, the amplitude condition is satisfied when the elevation amplitude is half of the maximal amplitude which occurs when the chamber is open. This is easily seen by setting $P = 0$ in eq. (2.10). Hence, both conditions can be checked roughly during experiments, merely by visual inspection.

Another advantage of the rigid-piston description, is that it makes it easy to compare the performance of the OWC with WECs consisting of oscillating rigid bodies.

While the above mathematical expressions represent what we will term *model I*, we consider as follows the hydrodynamically more correct applied-pressure description, here termed *model II*. According to this description, developed by Sarmento and Falcao [12], and of Evans [34], the total air volume flux corresponding to the oscillation water surface of the OWC, may be expressed as

$$\hat{Q} = \hat{Q}_e + \hat{Q}_r \tag{2.13}$$

Here, $\hat{Q}_e(\omega)$ represents the *excitation volume flux*, which means the flux caused by an incident wave if the air chamber is open to the atmosphere. Hence, $\hat{Q}_r(\omega)$, the *radiation volume flux*, is the contribution due to the dynamic air pressure in the chamber. Still assuming linearity, these terms may be written

$$\hat{Q}_e = q_e\hat{A} \tag{2.14}$$

and

$$\hat{Q}_r = -Y\hat{p} \tag{2.15}$$

where $q_e(\omega)$ and $Y(\omega)$ are complex coefficients of proportionality. We shall term q_e the *excitation volume flux coefficient*, and Y the *radiation admittance*. Further, $\hat{p}(\omega)$ is the complex amplitude of the dynamic air pressure in the chamber.

The power absorbed from the waves by the OWC may be expressed as [34]:

$$P = \overline{p\,Q} = P_e - P_r \tag{2.16}$$

where

$$P_e = \overline{p\,Q_e} = \frac{1}{2}|\hat{p}||\hat{Q}_e|\cos\gamma \tag{2.17}$$

and

$$P_r = \overline{p\,Q_r} = \frac{1}{2}G|\hat{p}|^2 \tag{2.18}$$

$P_e(\omega)$ and $P_r(\omega)$ are the excitation power and the radiated power in terms of the applied-pressure description. Further, γ is the phase difference between the excitation volume flux and the dynamic air pressure, and $G(\omega) = Re\{Y(\omega)\}$ is here termed the *radiation conductance*. The imaginary part $B = Im\{Y(\omega)\}$ is correspondingly termed the *radiation susceptance*. Here, the optimum phase condition is $\gamma = 0$, that is, the chamber pressure should be in phase with the excitation volume flux. When this is fulfilled, the absorbed power becomes

$$P = \frac{1}{2}\left(|\hat{p}||q_e\hat{A}| - G|\hat{p}|^2\right) \tag{2.19}$$

The maximum absorbed power is

$$P_{max} = \frac{1}{2}G|\hat{p}|^2_{opt} \tag{2.20}$$

occuring when

$$|\hat{p}|_{opt} = \frac{|q_e\hat{A}|}{2G} \tag{2.21}$$

When the rigid-piston approximation is valid, model I and model II are equivalent descriptions [34,35]. However, it should be noted that the terms *excitation*, and hence, also *radiation*, are used differently in the two cases. The excitation *volume flux* is defined as the total flux when the dynamic pressure in the chamber is zero, which means that the chamber is *open*. The excitation *force* is the total force on the surface when it is held fixed. Neglecting the air compressibility, this corresponds to a *closed* chamber. These differences are indicated in the expressions above by use of the different subscripts e,I r,I and e, r.

Throughout the theoretical derivations in this report, we shall use mostly the applied-pressure description (model II), but occasionally also the rigid-piston approximation (model I), when needed.

In the following, we present a way of converting the dynamics of an OWC system from one description model to another, interchanging the hydrodynamical parameters. In addition to the basic equations (2.5) and (2.13 - 2.15), describing the two models, we introduce the relations

$$\hat{Q} = S_k\hat{u} \tag{2.22}$$

and

$$\hat{F} = S_k \hat{p} + \rho g S_k \hat{s} \tag{2.23}$$

The first of the above relations is simply the definition of the volume flux at the interior surface of area S_k. The second relation, which represents balance of forces on the envisaged massless rigid piston, follows from the fact that the buoyancy of the oscillating water mass contributes to the total force. Here, $\rho g S_k$ may be termed the *hydrostatic stiffness* of the system.

Generalised to a double-chamber system, the equations (2.5), (2.13), (2.22) and (2.23) become

$$\hat{\mathbf{F}} = \mathbf{f}_{e,I} \hat{A} - \mathbf{Z}_{r,I} \hat{\mathbf{u}} \tag{2.24}$$

$$\hat{\mathbf{Q}} = \mathbf{q}_e \hat{A} - \mathbf{Y} \hat{\mathbf{p}} \tag{2.25}$$

$$\hat{\mathbf{Q}} = S_k \hat{\mathbf{u}} \tag{2.26}$$

$$\hat{\mathbf{F}} = S_k \hat{\mathbf{p}} + \rho g S_k \hat{\mathbf{s}} \tag{2.27}$$

The boldface symbols denotes vectors and matrices. Hence,

$$\hat{\mathbf{Q}} = \begin{bmatrix} \hat{Q}_1 \\ \hat{Q}_2 \end{bmatrix} \qquad \hat{\mathbf{p}} = \begin{bmatrix} \hat{p}_1 \\ \hat{p}_2 \end{bmatrix} \tag{2.28}$$

$$\hat{\mathbf{F}} = \begin{bmatrix} \hat{F}_1 \\ \hat{F}_2 \end{bmatrix} \qquad \hat{\mathbf{u}} = \begin{bmatrix} \hat{u}_1 \\ \hat{u}_2 \end{bmatrix} \qquad \hat{\mathbf{s}} = \begin{bmatrix} \hat{s}_1 \\ \hat{s}_2 \end{bmatrix} \tag{2.29}$$

$$\mathbf{q}_e = \begin{bmatrix} q_{e1} \\ q_{e2} \end{bmatrix} = q_{e1} \begin{bmatrix} 1 \\ 1 \end{bmatrix} \qquad \mathbf{Y} = \begin{bmatrix} Y_{11} & Y_{12} \\ Y_{21} & Y_{22} \end{bmatrix} \tag{2.30}$$

$$\mathbf{f}_{e,I} = \begin{bmatrix} f_{e1,I} \\ f_{e2,I} \end{bmatrix} = f_{e1,I} \begin{bmatrix} 1 \\ 1 \end{bmatrix} \qquad \mathbf{Z}_{r,I} = \begin{bmatrix} Z_{11} & Z_{12} \\ Z_{21} & Z_{22} \end{bmatrix} \tag{2.31}$$

The indices 1,2 denote chamber numbers. The elements in the vector $\mathbf{q}_e$ are equal because the direction of the incident wave is perpendicular to the front wall of the OWC model. The same is true for the elements of $\mathbf{f}_{e,I}$, for the same reason. Note, however, that when the whole system acts as a single chamber, the quantities q_e and $f_{e,I}$ will be the sum of the elements of the corresponding vectors in the double-chamber case. Since the two chambers are equal, this means that the excitation parameters for the single-chamber case are twice as large as the corresponding parameters for each chamber of the twin OWC:

$$q_e = 2 q_{e1} \tag{2.32}$$

$$f_{e,I} = 2 f_{e1,I} \tag{2.33}$$

Here, q_e and $f_{e,I}$ are parameters for the single-chamber case, while q_{e1} and $f_{e1,I}$ refers to one of the chambers of the double-chamber system.

Combining (2.24) and (2.27), and using that $\hat{u}_k = j\omega \hat{s}_k$, we obtain

$$S_k \hat{\mathbf{p}} = \mathbf{f}_{e,I} \hat{A} - (\mathbf{Z}_{r,I} + \frac{\rho g S_k}{j\omega} \mathbf{I}) \hat{\mathbf{u}} \tag{2.34}$$

where $\mathbf{I}$ is the identity matrix. Inserting (2.26) gives

$$S_k\hat{\mathbf{p}} = \mathbf{f}_{e,I}\hat{A} - (\frac{\mathbf{Z}_{r,I}}{S_k} + \frac{\rho g}{j\omega}\mathbf{I})\hat{\mathbf{Q}} \tag{2.35}$$

and, rearranging the terms:

$$\hat{\mathbf{Q}} = (\frac{\mathbf{Z}_{r,I}}{S_k} + \frac{\rho g}{j\omega}\mathbf{I})^{-1}(\mathbf{f}_{e,I}\hat{A} - S_k\hat{\mathbf{p}}) \tag{2.36}$$

The elements in the radiation impedance matrix $\mathbf{Z}_{r,I}$ and the radiation admittance matrix $\mathbf{Y}$, may be written Z_{kl} and Y_{kl}, respectively, where the indices $k = \{1,2\}$ and $l = \{1,2\}$ denote chamber numbers. Hence, Z_{12} represents the contribution to the radiation force on water column number 1, due to oscillations in chamber number 2.

In general, we have $Z_{12} = Z_{21} \equiv Z_x$ and $Y_{12} = Y_{21} \equiv Y_x$ [34]. Due to the geometrical symmetry of our system, we also have $Z_{11} = Z_{22} \equiv Z_d$ and $Y_{11} = Y_{22} \equiv Y_d$. The indices x and d denote cross terms and diagonal terms, respectively.

After some algebraic manipulation, equation (2.36) gives

$$\hat{Q}_1 = \frac{S_k(Z_d' - Z_x)f_{e1,I}\hat{A} + S_k^2(Z_x\hat{p}_2 - Z_d'\hat{p}_1)}{Z_d'^2 - Z_x^2} \tag{2.37}$$

and

$$\hat{Q}_2 = \frac{S_k(Z_d' - Z_x)f_{e1,I}\hat{A} + S_k^2(Z_x\hat{p}_1 - Z_d'\hat{p}_2)}{Z_d'^2 - Z_x^2} \tag{2.38}$$

where we have introduced the quantity $Z_d' = Z_d + \rho g S_k/j\omega$. Then, comparing the equations (2.37) and (2.38) with (2.25), we obtain

$$q_{e1} = S_k\frac{f_{e1,I}}{Z_d' + Z_x} \tag{2.39}$$

$$Y_d = S_k^2\frac{Z_d'}{Z_d'^2 - Z_x^2} \tag{2.40}$$

$$Y_x = -S_k^2\frac{Z_x}{Z_d'^2 - Z_x^2} \tag{2.41}$$

The three expressions (2.39 - 2.41) show how we may convert the description of the double-chamber system from the rigid-piston model (model I) to the applied-pressure model (model II).

Combining the expressions and rearranging the terms, we obtain

$$f_{e1,I} = S_k\frac{q_{e1}}{Y_d + Y_x} \tag{2.42}$$

$$Z_d' = S_k^2\frac{Y_d}{Y_d^2 - Y_x^2} \tag{2.43}$$

$$Z_x = -S_k^2\frac{Y_x}{Y_d^2 - Y_x^2} \tag{2.44}$$

thus, allowing conversion the other way around.

We can derive similar conversion equations for the single-chamber case, simply by setting $Z_x = 0$ and $Y_x = 0$, and replacing the symbols q_{e1}, $f_{e1,I}$ and Y_d with the corresponding single-chamber parameters q_e, $f_{e,I}$ and Y. Further, we replace the water surface area S_k where $k = 1,2$ with the sum $S = S_1 + S_2 = 2S_k$. Hence, we obtain [35,39]:

$$q_e = \frac{S f_{e,I}}{Z'} \tag{2.45}$$

$$Y = \frac{S^2}{Z'} \tag{2.46}$$

and

$$f_{e,I} = \frac{S q_e}{Y} \tag{2.47}$$

$$Z' = \frac{S^2}{Y} \tag{2.48}$$

where $Z' = Z_{r,I} + \rho g S/j\omega$. Note that that if we include linear losses by replacing $Z_{r,I}$ with $Z_{r,I} + R_f$, where R_f is the loss resistance, this will alter both q_e and Y. The effect of linear losses on the dynamical description in model II is considered more closely in chapter 5.

2.1.2 Maximum absorbed power. Optimum performance of a point absorber

As mentioned previously, the absorbed power is maximum when the pressure has its optimum value. Then half of the excitation power is absorbed, while the remaining half is radiated back to the sea. This can be achieved by proper choice of a complex load admittance. The total volume flux measured on the interior water surface may be written

$$\hat{Q} = \Lambda \hat{p} \tag{2.49}$$

where $\Lambda(\omega)$ in the general case is a complex load admittance, which may partly or completely be due to the air turbine (see appendix C). Combining equation (2.49) with eq. (2.13) and eq. (2.15), we obtain

$$\hat{p} = \frac{\hat{Q}_e}{\Lambda + Y} \tag{2.50}$$

The phase condition is satisfied when $\hat{p}$ and $\hat{Q}_e$ are in phase, which means that $Im\{\Lambda\} = -Im\{Y\}$. The optimum pressure amplitude has been found to be $|\hat{p}|_{opt} = |\hat{Q}_e|/2G$ in equation (2.21). Comparing this with equation (2.50), we see that it corresponds to $Re\{\Lambda\} = Re\{Y\}$ [34]. Thus, both the phase condition and the amplitude condition can be expressed in a single expression:

$$\Lambda = Y^* \tag{2.51}$$

where the asterisk denotes complex conjugation. This relation is analogous to the case of load impedance matching in electric circuits (see section 5.2).

Whereas the optimum phase condition is sought fulfilled by means of phase control, it is not necessarily desirable to satisfy the optimum amplitude condition in all cases. For small wave amplitudes it is straightforward to aim for such an optimum, but if the incident waves are large, we would need a rather large oscillation amplitude to satisfy the condition. This is possible only if the WEC is a large construction. Since the construction costs tend to depend on the physical dimensions of the WEC, such an approach may not be economically advantageous, even though it would provide the maximum absorption of energy from the waves.

Here, we propose another strategy for moderate to large incident waves. Given a rather small construction, and using the terms of the rigid-piston description for clarity, we choose a large load resistance. Then we will have that $|\hat{u}| \ll |\hat{u}|_{opt}$, and $P_{r,I} \ll P \approx P_{e,I}$ (see eqs. (2.12) and (2.7 - 2.9)). That is, essentially all excitation power is absorbed, but most of the total wave power remains in the sea, since there is a negligible radiated wave to interfer destructively with the large incident wave. Hence, we do not attempt to achieve the theoretical maximum absorption, but to take out as much energy as possible given the available capacity of the WEC. Provided that the phase condition is satisfied, this line of action corresponds to a maximum of the absorbed power *per power-plant volume* [39]. This may be an economically preferable approach, as the remaining wave power in the sea is free [40]. (We may note here, that in our experiments we have used only small waves, and not what here have been classified as moderate to large waves.)

A point absorber usually has a resonance frequency considerably higher than the typical wave frequency. For this reason the optimum phase condition will not be fulfilled in the general case. As mentioned previously, however, it is possible to approach the optimal behaviour by use of control equipment [41,42]. A buoy or another rigid oscillating body can be phase-controlled by latching the body mechanically in its outermost positions, and then releasing it at just the right moments to keep the velocity of the body approximately in phase with the excitation force [43,44,45].

The use of phase control improves the performance of the device considerably at wave frequencies lower than its natural resonance frequency. The net result is an increase of the point absorber's effective bandwidth. It should be noted, however, that real sea waves are in general irregular. It can be shown that optimum phase control in the general case requires that the incident wave is being predicted some time into the future [46,47,48].

2.1.3 Applying phase control to OWCs

A single OWC can be phase-controlled by closing and opening an air valve placed in series with the turbine. In this way, the water column can, to some extent, be held back and subsequently released during each oscillation period. However, numerical simulations have shown that a construction of this type will produce pneumatic power that is pulse-like, with extreme maxima and a relatively low average value [32]. This will lead to a low turbine efficiency, and it would also demand a large and expensive turbine in order to utilise the large instantaneous power. Hence, the described approach needs improvement. An alternative way to obtain phase control, as described below, has been proposed by Budal [33].

It turns out that the performance improves considerably if the chamber is divided into

two separate chambers, with the air turbine placed between them. In this case we use two air valves, one for each chamber. One of the valves lets air in *from* the atmosphere, and the other lets air out *to* the atmosphere. Then we have a system with one high pressure chamber and one low pressure chamber. This causes a systematic pressure difference between the two chambers, and hence, a smoothing effect on the pneumatic power input to the turbine. The system also has the advantage that the air flow through the turbine is being rectified. This means that the turbine does not need to be of the self-rectifying type, and a more efficient air turbine may be utilised.

The optimum phase condition becomes more complicated when the WEC consists of two bodies or two water columns [34,49]. The system has to be described in terms of vectors, and for our twin-OWC system we have already introduced the relation (2.25):

$$\hat{\mathbf{Q}} = \mathbf{q}_e \hat{A} + \mathbf{Y}\hat{\mathbf{p}} \tag{2.52}$$

where $\hat{\mathbf{Q}}(\omega)$, $\mathbf{q}_e(\omega)$ and $\hat{\mathbf{p}}(\omega)$ have been described earlier (see eqs. (2.28 - 2.31)). This can also be written

$$\hat{Q}_1 = q_{e1}\hat{A} + Y_{11}\hat{p}_1 + Y_{12}\hat{p}_2 \tag{2.53}$$

$$\hat{Q}_2 = q_{e2}\hat{A} + Y_{21}\hat{p}_1 + Y_{22}\hat{p}_2 \tag{2.54}$$

The indices denote chamber number. The cross terms $Y_{12}(\omega)$ and $Y_{21}(\omega)$ are the mutual radiation admittances between the two chambers. As mentioned in section 2.1.1, we have that $Y_{12} = Y_{21} \equiv Y_x$, $Y_{11} = Y_{22} \equiv Y_d$ and $q_{e1} = q_{e2} \equiv q_e$. The subscripts d and x denote diagonal and cross terms, respectively.

It can be shown that the maximal absorbed power in the two-chamber case is [34]:

$$P_{max} = \frac{1}{2}\,\hat{\mathbf{p}}_{opt}^{T}\,\mathbf{G}\,\hat{\mathbf{p}}_{opt}^{*} \tag{2.55}$$

where $\mathbf{G} = Re\{\mathbf{Y}\}$, the superscript T denotes transposing, and $\hat{\mathbf{p}}_{opt}$ is the optimum pressure amplitude, satisfying the condition

$$\mathbf{G}\,\hat{\mathbf{p}}_{opt} = \frac{1}{2}\,\mathbf{q}_e\hat{\eta}_i \tag{2.56}$$

provided that no amplitude constrictions apply.

In irregular waves this condition for optimum can be satisfied exactly only by controlling the oscillations continuously. In our case, control action is applied only at four instants during each wave period, by opening and closing each of the two air valves. Thus, it is possible to approach the optimum behaviour only approximately.

Each instant a valve opens or closes, the dynamics of the system changes abruptly. Thus, the system is not time-invariant, and the time-dependent variables are no longer harmonic, even if the incident wave is regular. Hence, it is not straightforward to determine the conditions for optimum operation of the air valves. This means that such conditions may preferably be determined experimentally, or alternatively, by means of computer simulation in the time domain.

When designing the phase-control system for a real wave power plant, we want to optimise with respect to maximising the net useful (i.e. electric) power, and not the

power absorbed from the waves. The absorbed power is the sum of the net useful power and all power losses in the system. Loss effects include viscosity and vortex shedding in the water, as well as loss through heat conduction. Some power is also lost through the air valves, partly because of the flow constriction, but also due to air compressibility. The latter effect occur when a valve is opened while the pressure drop across it is non-zero. Finally, there is a loss associated with energy conversion in the turbine and in the electric generator, but these elements are not considered in the present experiments.

The amount of valve loss and nonlinear loss in the water both depend on the instants of valve operation. This means that the control strategy which provides for a maximum useful power production, may not necessarily lead to a maximum of the power absorbed from the waves. In other words, it may pay to increase the losses, provided that the net converted energy also is increased.

Power conversion and losses throughout the system are:

$$P = P_f + P_{pn} \tag{2.57}$$

$$P_{pn} = P_{vl} + P_{tur} \tag{2.58}$$

Here, P is the power absorbed from the waves, P_f is the power loss due to viscous effects in the water, and P_{pn} is the pneumatic power, that is, power transferred to the air in the chambers by the oscillating interior water surfaces. Further, P_{vl} is the power loss due to the valves, and P_{tur} is the power input to the turbine. Losses due to heat conduction have been neglected here.

2.1.4 Power take-off

In a real OWC power plant, the power take-off device will almost always be some kind of air turbine. During the last two decades, most OWCs which have been tested in full scale, have been equipped with the self-rectifying Wells turbine. In our case, the rectification of the air due to the air valves permits the use of a conventional turbine, which may be more efficient.

Both Wells turbines and conventional, non-rectifying turbines may be considered as linear elements for moderate pressure amplitudes. In this case, the term linear means that the volume flux of air through the turbine is proportional to the pressure drop across it. Neglecting air compressibility, this may be expressed in the frequency domain as follows:

$$\hat{Q}(\omega) = G_l(\omega)\hat{p}(\omega) \tag{2.59}$$

where the *load conductance* G_l do not depend on the dynamic air pressure. Hence, if the model OWC in the experiments is equipped with a turbine operating in its linear range, the analysis of the system becomes mathematically simple. In practice, however, a turbine might turn out to be difficult to handle. We might be interested in varying the load impedance of the system throughout the experiments. In the case of a turbine, this may require some sort of adjustable power load, i.e. an electric generator, which will complicate the experiments. Alternatively, we may use several different turbines in turns. This would however be even more unconvinient. Another problem which may arise using

turbines, is that it may easily enter the nonlinear range during parts of the time, and moreover, it may even stall.

To avoid the problems mentioned above, we have used orifices as power take-off devices during this work. This makes the experiments easy to carry out, it reduces the number of parameters, and the load impedance may easily be varied from run to run. The orifices are, however, nonlinear elements. This complicates some of the analysis of the results. According to theory [50], the volume flux through an orifice may be expressed

$$Q_{or}(t) = \mu d_b^2 C_b \frac{p(t)}{\sqrt{|p(t)|}} \tag{2.60}$$

Here, μ is a factor depending on the orifice, d_b is the orifice diameter, $C_b \approx 0.00102$ $\mathrm{m}^{3/2}\mathrm{kg}^{-1/2}$ and p is the pressure drop through the orifice.

A more thorough discussion of this subject is presented in appendix C.

2.2 Experiments and results

Our model tests of the phase-controlled twin OWC serve several purposes. One is to find a best strategy for controlling the air valves, that is, to determine which instants, relative to the incident wave, the air valves should be opened and closed, in order to maximise the net useful power. Another purpose is to determine the energy gain that can be expected, compared to a single oscillating water column without phase control. Finally, such experiments are useful to verify existing theoretical models. In the present work only regular incident waves are considered.

2.2.1 Setup and measurements

A twin-OWC model in scale 1:10 (compared to the prototype at Toftestallen) [14], has been constructed mainly in perspex plates on an aluminium frame. However, the front wall and also the curved edges near the OWC mouth, are made from PVC-foam. As mentioned in the introduction, the interior water surface of the full-scale pilot plant at Toftestallen, was 50 m^2 and approximately triangular. The mouth area was about 70 % of the interior water surface. Contrary to this, the area of the water surfaces in the model are equal to the corresponding mouth areas. Besides, all cross-sections are rectangular, and not triangular (see figure 2.2). The top plate of the model is designed in two different versions. One of the plates is made for model tests of a one-chamber system. At this plate the chambers are directly connected, and hence, act as a single chamber. Instead of a real turbine, an orifice is placed in a duct between the air chamber and the ambient atmosphere. The inner diameter of the duct is varying between 0.11 m and 0.19 m (see figure 2.2). On the other top plate, designed for the two-chamber system, the orifice is placed in a duct with an inner diameter of 0.10 m, connecting the two chambers. There are also two air valves on this plate, placed above each of the air chambers. Water level gauges and pressure transducers are mounted in either air chamber. These are, for simplicity, omitted in figure 2.2.

After each experimental run we have to wait about 10 min. for the water to get calm, before starting the next run. Both valves are closed and opened at certain instants after the zero up-crossing time of the incident wave. This is accomplished by letting the signal from a wave gauge trigger a signal which increases linearly with time (see figure 2.3). This signal is being compared to four stationary voltage levels, which can be set independently. When the signal exceeds each of these levels, the corresponding valve control signal is triggered. The data aquisition is started manually, by pressing a button, as soon as the oscillations in the chambers appear to be stationary.

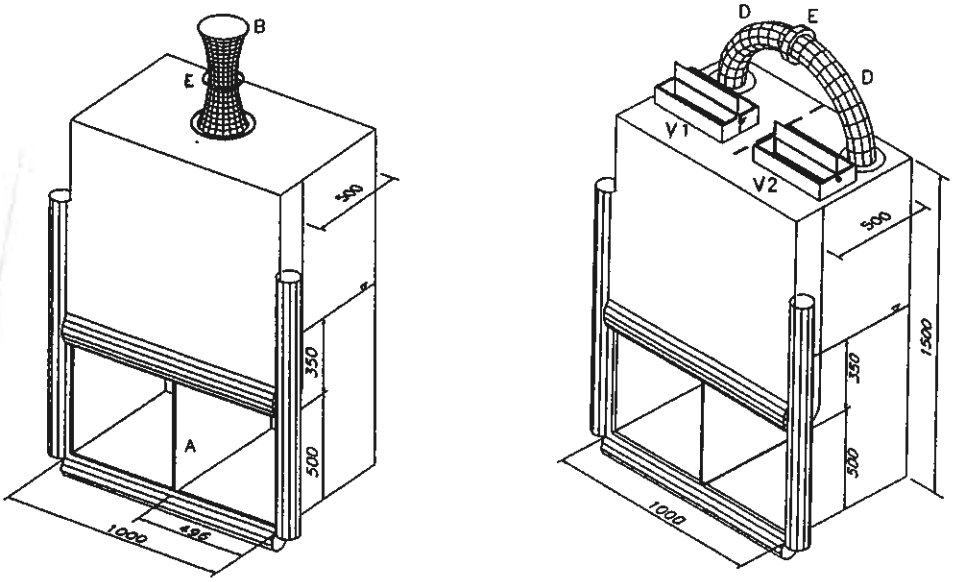

Figure 2.2: 1:10 scale wave power converter with two OWCs and air valves for phase-control. Left: Top plate for the one-chamber system. Right: top plate for the two-chamber system. A: bisecting wall. B: air duct. D: interconnecting air duct. E: orifice. V1, V2: air valves.

The model experiments have been carried out in two separate parts. The first part was accomplished in the 10 m wide ship model tank at the Marine Technology Center (MTS) in Trondheim (see figure 2.4). This was a rather intensive series of experiments during one week, aiming to get an overall knowledge about the system [51]. The model was tested both as a one-chamber system and a phase-controlled two-chamber system. The orifice diameter, the wave period, the wave amplitude, and, for the two-chamber system, the valve operation times, were varied throughout the experiment series. These experiments are in the following referred to as *setup A*.

The second part of the experiments was performed in a 3.8 m wide wave flume at the Norwegian Hydrotechnical Laboratory (NHL), Trondheim (see figure 2.5). The intention was to focus upon details from the first experiment period. Measurements and analysis were done in turns, over a longer period of time. We will call this the *setup B*. Unless otherwise stated, all results and discussions in the following concern setup B.

Figure 2.4 shows the arrangement of setup A. Wave gauges are numbered and marked with a small circle on the figure. The incident wave was measured by gauge no. 3, while

the gauges 1 and 2 measured the interior surface elevations.

At setup B (figure 2.5), the number of wave gauges has been increased. Gauges 3 and 4 were placed one quarter of a flume width from each side wall. This made it possible to detect antisymmetrical cross waves. In addition, there were three gauges (5, 6 and 7) about 8 - 9 m from the model. From these three measurements we could calculate amplitude and phase of both the incident and the reflected wave (including the radiated wave). This, in turn, was used to calculate the absorbed power as the power removed from the waves.

It should be noted that there were differences in the inlet conditions in the two experimental cases. With setup A, the model was protruding into the water, with its back wall attached to the reflecting end wall of the wave tank. With setup B, the model was built into the end wall of the flume. One purpose of this change was to reduce the viscous losses.

All measured signals (water elevations and chamber pressures) were logged by a computer, and could also be displayed directly on an oscilloscope during the measurements. The signal from gauge no. 3 was used to trigger the valve control signals. From the measured quantities, we also derived other quantities, of which the most important (velocities, power, work, etc.) were calculated by the logging program continuously. Thus, time series were available for further analysis shortly after each run.

In order to quantify the power converted by the system, we use the terms *absorption width* and *pneumatic capture width*. The absorption width is defined as

$$d_{abs} = P/J \tag{2.61}$$

where the absorbed power P is defined in equation (2.2), and the incident wave energy transport J is defined in equation (2.4). The definition of d_{abs} implies that it may well exceed the physical width of the OWC device. If it is equal to the flume width, all incident wave power is absorbed.

The pneumatic capture width, d_{pn}, tells us how much of the incident wave energy that is converted to pneumatic energy. The pneumatic capture width is defined as

$$d_{pn} = W_{pn}/(JT_{reg}) \tag{2.62}$$

Here, W_{pn} is the pneumatic work accumulated in the chambers during the registration time T_{reg}, which is chosen to be a multiple of the wave period $T = 2\pi/\omega$. The pneumatic work for the twin-OWC case has been calculated as follows:

$$W_{pn} = \int_0^{T_{reg}} P_{pn}(t)dt = \sum_{k=1}^{2} \left(S_k \int_0^{T_{reg}} p_k(t)\, u_k(t)\, dt \right) \tag{2.63}$$

where $p_k(t)$ is the dynamic air pressure and $u_k(t)$ is the oscillation velocity of the interior water surface in chamber no. k at time t.

We may also define an *orifice capture width*, d_{or}, and a corresponding accumulated orifice energy. Because of experimental uncertainty, such measured quantities are not presented in our results. The terms are, however, described in appendix D.

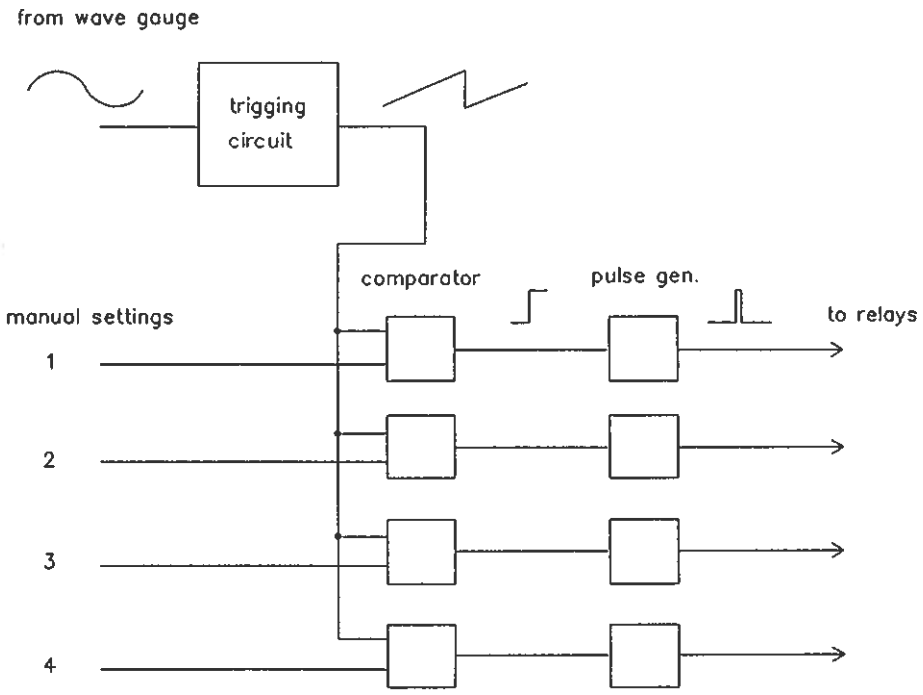

Figure 2.3: Control system for operating the valves. The opening and closing times are set manually before each experimental run.

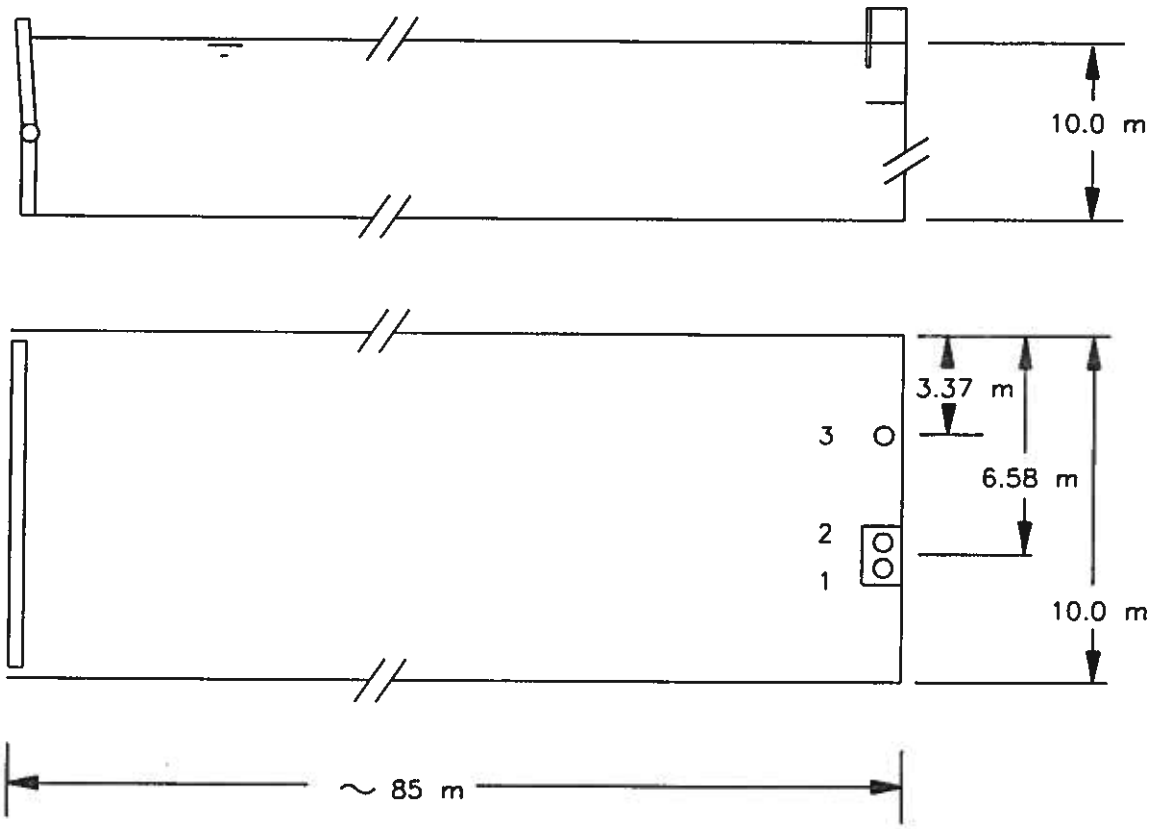

Figure 2.4: Experimental setup A. Numbered circles show positions of wave gauges. The water depth is approximately 10 m.

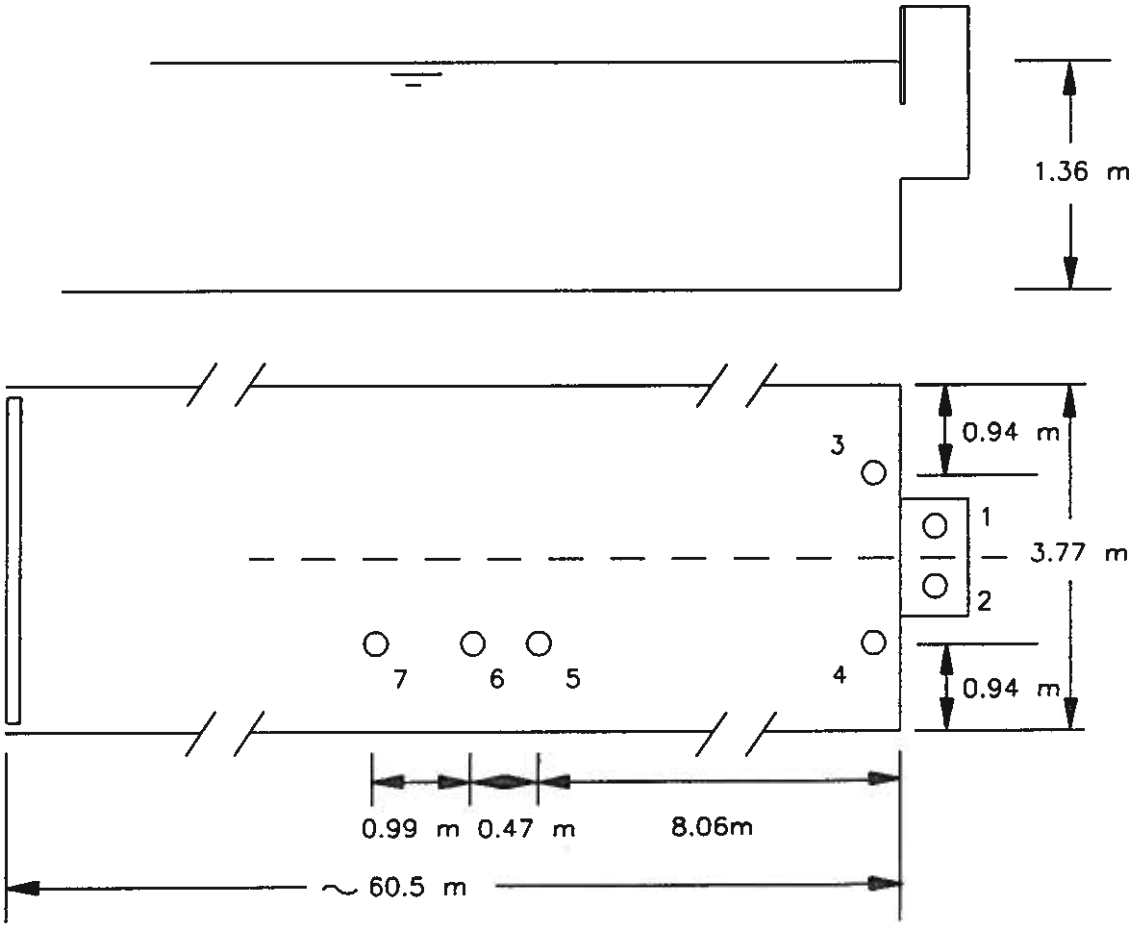

Figure 2.5: Experimental setup B. Numbered circles show positions of wave gauges. The water depth is 1.36 m.

2.2.2 Single OWC

For comparison, a series of experiments have been carried out with the system working as a single OWC with no phase control. Then the two chambers act together as one chamber of double width. The orifice is then placed between the chamber and the outer atmosphere. No air valve is used with this setup.

By varying the incident wave amplitude $\hat{A}$, and then measure the corresponding chamber excursion amplitude $\hat{s}$ when the chamber is open, and the dynamic air pressure amplitude $\hat{p}$ when the chamber is closed, we can determine to what extent linear hydrodynamic theory is applicable. According to model II, we have for an open chamber (see equation 2.14):

$$\hat{Q} = q_e \hat{A} \tag{2.64}$$

and also (see eq. (2.22)):

$$\hat{Q} = \hat{u} S = j\omega \hat{s} S \tag{2.65}$$

Here, S is the area of the total internal water surface ($S = S_1 + S_2$). Hence, we can write

$$|\hat{s}| = \frac{|q_e|}{\omega S} |\hat{A}| \tag{2.66}$$

That is, for a given frequency, the amplitude of the chamber excursion should be proportional to the amplitude of the incident wave, provided that the chamber is open.

When the chamber is closed and air compressibility is neglected, model I gives (see eq. (2.5)):

$$\hat{F} = f_{e,I} \hat{A} \tag{2.67}$$

and (see eq. (2.23)):

$$\hat{F} = S\hat{p} \tag{2.68}$$

where $\hat{F}$ is the force on the internal water surface and $f_{e,I}$ is the excitation force coefficient. It is here assumed that the internal surface oscillates as a horizontal, rigid piston, however with a negligible amplitude. This leads to

$$|\hat{p}| = \frac{|f_{e,I}|}{S} |\hat{A}| \tag{2.69}$$

Thus, when the chamber is closed, the amplitude of the dynamic air pressure in the chamber should be proportional to the amplitude of the incident wave. Further, if the chamber is closed or fully open, no energy is absorbed by the system apart for possible viscous energy loss, and the radiated wave may be neglected. Hence, the elevation just outside the chambers (gauge no. 3) is approximately proportional to the incident wave. By measuring the chamber excursion when the chamber is closed, we have found that neglecting air compressibility in the closed-chamber case, leads to an uncertainty in the pressure of about 10 %.

It should be noted that the term "open chamber" is not entirely precise in describing these experiments, since the top plate is never removed. "Open" only means that there is no orifice present in the duct. There will of course be a certain air flow restriction in the duct anyway, especially when the excursion amplitudes in the chambers are large. Besides, nonlinear loss mechanisms in the water are likely to become more important

when the chamber is open, since the chamber excursion amplitudes then are considerably larger than in the closed-chamber case. Hence, when the incident wave is large, the results obtained with closed chamber are expected to exhibit closer resemblance to linear behaviour than those obtained with open chamber.

The linearity tests have been carried out at a wave period of T = 3.0 s. Figure 2.6 displays the results from these tests. We conclude that the results show good agreement with linear theory. However, the open-chamber case exhibits slight deviation from linearity at larger amplitudes, in accordance with our expectations.

The reasonable agreement with linearity indicates that vortex shedding in the water, which is a nonlinear effect, has been of minor importance during the single-chamber experiments, except, possibly, for the largest wave amplitudes. However, comparing the absorption width and the capture width for various wave periods (figures 2.7 - 2.10), there appears to be significant viscous losses in the water. It should be noted, however, that the absorption-width results are hampered with considerable uncertainties ($\sim 15\%$). Hence, the amount of power loss may be inaccurately estimated (see appendix A). It is consistent with our results to make the convenient assumption of a linear relationship for the losses, since possible nonlinear losses cannot be quantified from the measurements given in figure 2.6.

In the figures 2.7 - 2.10 each bar represents one experimental run. Each figure contains a collection of runs, displayed side by side for comparison. There is no quantity associated with the horizontal axes of these figures. The relative uncertainty in each experimental run is given in percent, rounded to the closest whole number, beside each bar in the figures.

Assuming a linear damper, the load admittance Λ is defined by the expression

$$\hat{Q} = \Lambda \hat{p} \tag{2.70}$$

Here, $\Lambda(\omega)$ may generally be a complex quantity. In experiments the imaginary part of Λ will be due to air compressibility, which may be neglected at our model scale. Hence, Λ is approximated with its real part, that is, the load conductance (see appendix C).

If a Wells turbine is being used, equation (2.70) is fairly accurate for moderate pressure amplitudes. However, in the present work we have used orifices for experimental simplicity. These are nonlinear elements, causing all time-varying quantities except the incident wave and the excitation parameters (Q_e and $F_{e,I}$) to be nonharmonic. Hence, equation (2.70) is no longer valid. Given a periodic incident wave, the other variables may be assumed to be periodic, too. Then the dynamic air pressure and the volume flux may be expressed as Fourier series, that is,

$$p(t) = \sum_{n=-\infty}^{\infty} a_{p,n}(\omega)\, e^{jn\omega t} \tag{2.71}$$

and

$$Q(t) = \sum_{n=-\infty}^{\infty} a_{Q,n}(\omega)\, e^{jn\omega t} \tag{2.72}$$

where $a_{p,n}$ and $a_{Q,n}$ are complex Fourier coefficients, and ω is the angular frequency of the incident wave. The Fourier coefficients may easily be determined by performing FFT

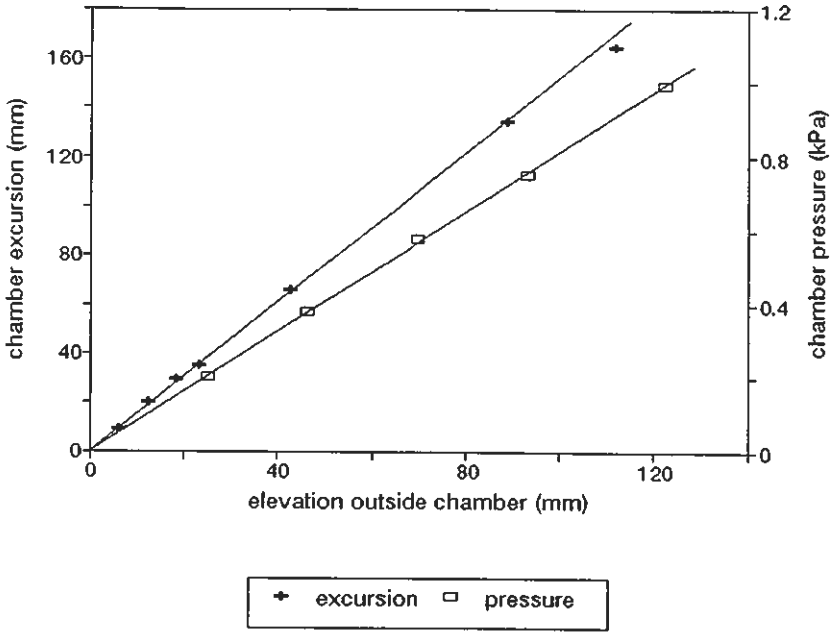

Figure 2.6: Linearity test for the single OWC. The wave period is 3.0 s. With open chamber the elevations have an absolute error of about 3 mm. With closed chamber the relative error in the pressure is less than 5 %. The results are obtained with setup B.

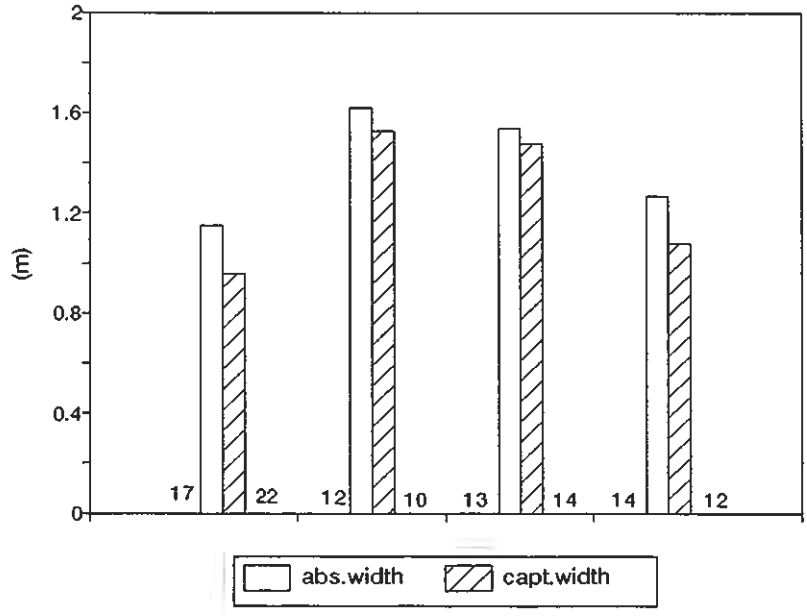

Figure 2.7: Absorption width and capture width for four different runs of the single OWC at wave period 1.8 s (setup B). The relative experimental uncertainty is given in percent, rounded to the closest whole number, beside each bar in the diagram.

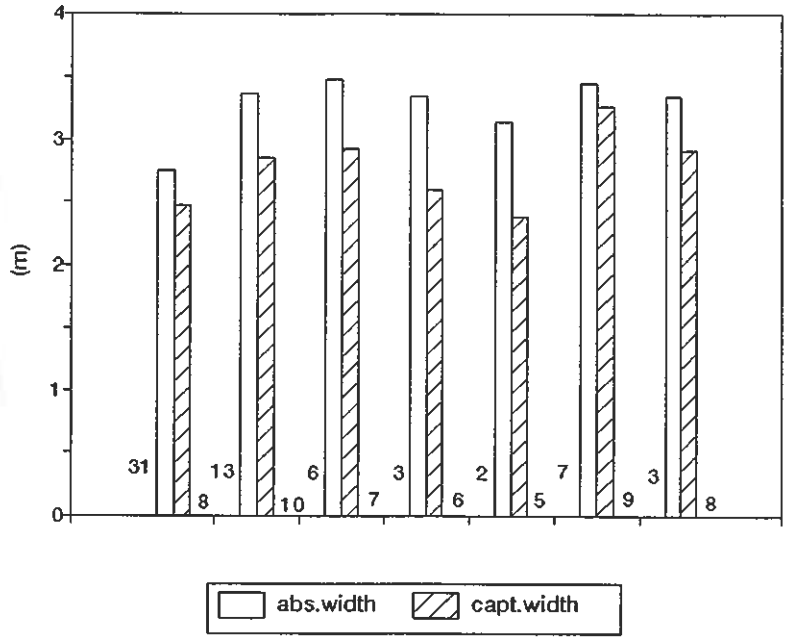

Figure 2.8: Absorption width and capture width for seven different runs of the single OWC at wave period 2.1 s (setup B). The uncertainty is given in percent.

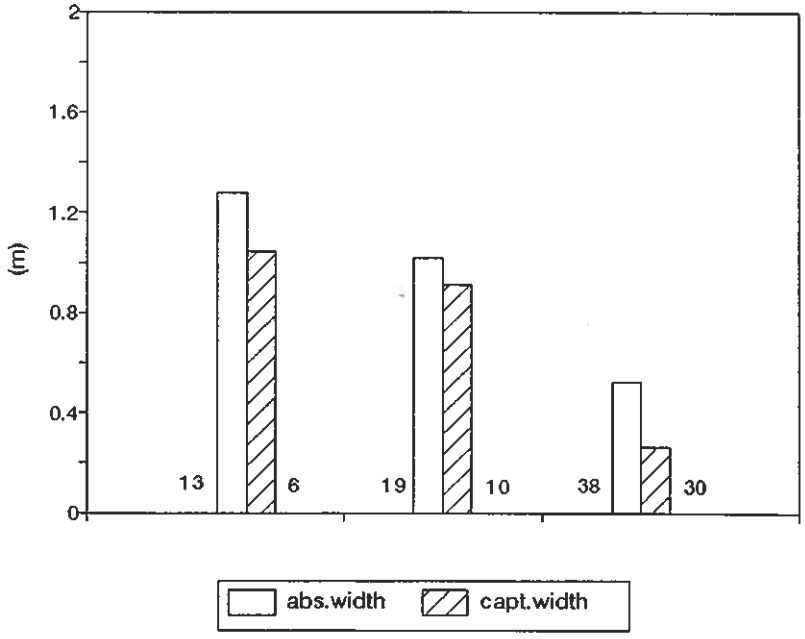

Figure 2.9: Absorption width and capture width for three different runs of the single OWC at wave period 2.6 s (setup B). The uncertainty is given in percent.

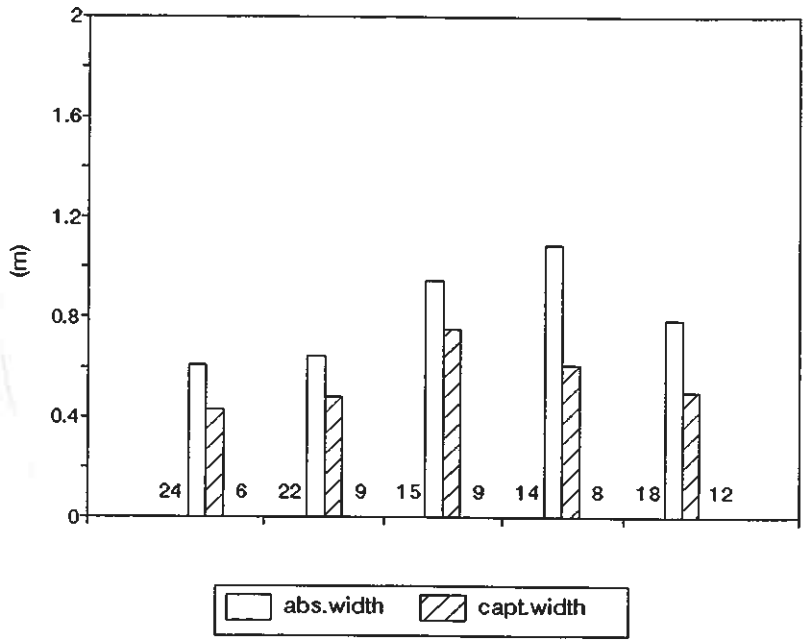

Figure 2.10: Absorption width and capture width for five different runs of the single OWC at wave period 3.0 s (setup B). The uncertainty is given in percent.

on the experimental time series. From the expressions (2.71) and (2.72) we define for this nonlinear case a load conductance, G_{nl}, as follows:

$$G_{nl}(\omega) = Re\{\frac{a_{Q,1}(\omega)}{a_{p,1}(\omega)}\} \tag{2.73}$$

that is, only the first harmonic is taken into consideration.

We have earlier been neglecting the air compressibility in the chamber. It turns out, for instance, that the chamber excursion becomes negligibly small when the chamber is closed. Likewise, the imaginary part of the load impedance, due to the air compressibility, is negligable compared to the load conductance of the power take-off. However, measuring $Q(t)$ at the water surface, the air compressibility will cause a small, but significant phase lag between this volume flux and the dunamic air pressure. This is why G_{nl} is defined as the real part of $a_{Q,1}/a_{p,1}$.

It should be noted that the nonlinearity of the orifices also causes the radiated wave to contain higher frequency components.

According to Sarmento and Falcão [52,53], different runs using an orifice as power take-off will be comparable, provided that the relation $Q(t)/(|\hat{A}|p(t))^{1/2}$ is an invariant function from run to run. In our experiments, however, this has not been the case. Hence, the results mentioned in the following should be taken merely as crude approximations, and no uncertainty estimates are included in the figures 2.11 - 2.14. In figures 2.11 - 2.12, the absorption width and the capture width are expressed as functions of G_{nl}. The figures indicate that the optimum load conductance for frequencies off resonance is in the range of 0.1 - 0.5 $m^3/(s\,kPa)$. For a full-scale power plant, this corresponds approximately to a load conductance in the range of 3.0 - 20 $m^3/(s\,kPa)$. For frequencies close to resonance, figures 2.11 and 2.12 are less conclusive. However, as we shall see later (cf. 2.17), other results indicate that the optimum load conductance may be in the range of 1.5 - 2.2 $m^3/(s\,kPa)$, which means that the optimum result for $T = 2.1$ s lays outside the

displayed range in the figures 2.11 - 2.14. These quantitative results correspond to a full-scale load conductance in the range of 45 - 70 $m^3/(s\,kPa)$. The results from the prototype OWC at Toftestallen indicated that the load conductance should be in the range of 2.5 - 10 $m^3/(s\,kPa)$ [14], a result which is in good agreement with experimental results for frequencies far from resonance. The agreement is poor, however, for frequencies close to resonance. We do not know what the typical wave frequencies have been at Toftestallen. Besides, the geometry of the full-scale prototype is, as explained previously, not in every detail completely comparable to the geometry of the model.

For comparison with the twin-chamber case, the absorption width and the capture width are also displayed as functions of the orifice diameter (figures 2.13 - 2.14). As above, this representation is a crude simplification, as the displayed quantities also depend on the wave amplitude, and we are neglecting higher frequency components. Nevertheless, these graphs are assumed to give a rough indication of the optimum orifice diameter for each wave period. For a wave period of 3.0 s, the optimum orifice diameter for the single OWC seems to be in the range of 55 to 75 mm. For the twin OWC, the optimum orifice diameter is found to be in the range 30 to 45 mm for the same wave period (see section 2.2.3).

The frequency response for the one-chamber system is obtained both for an open chamber, and for the case that the orifice diameter is optimised for each wave period. These results are shown in figures 2.15 and 2.16. Note that the results may have been influenced by cross waves for wave periods shorter than 2.44 s (see appendix B).

In figure 2.17, the load conductance resulting in maximum absorption width and maximum capture width, respectively, is shown as a function of the wave period.

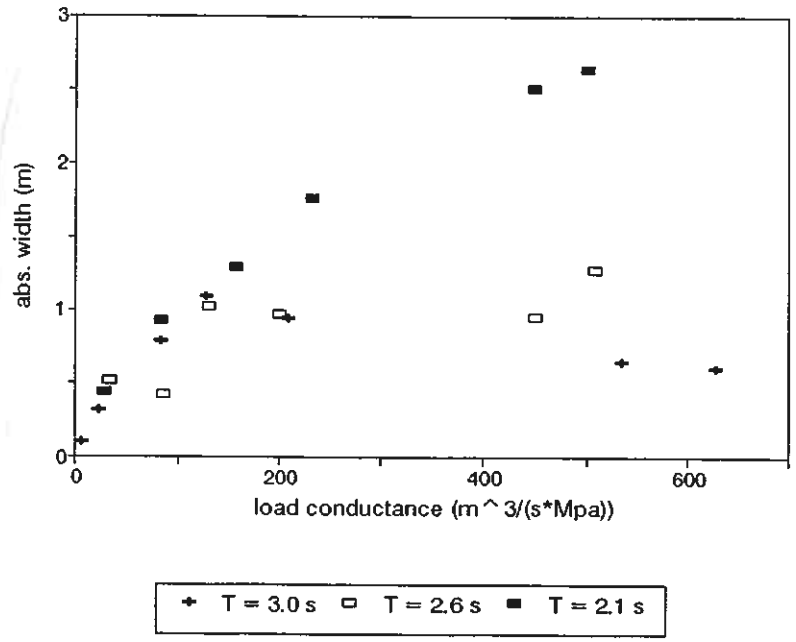

Figure 2.11: Absorption width vs. load conductance for the single OWC at wave periods 2.1 s, 2.6 s and 3.0 s (setup B).

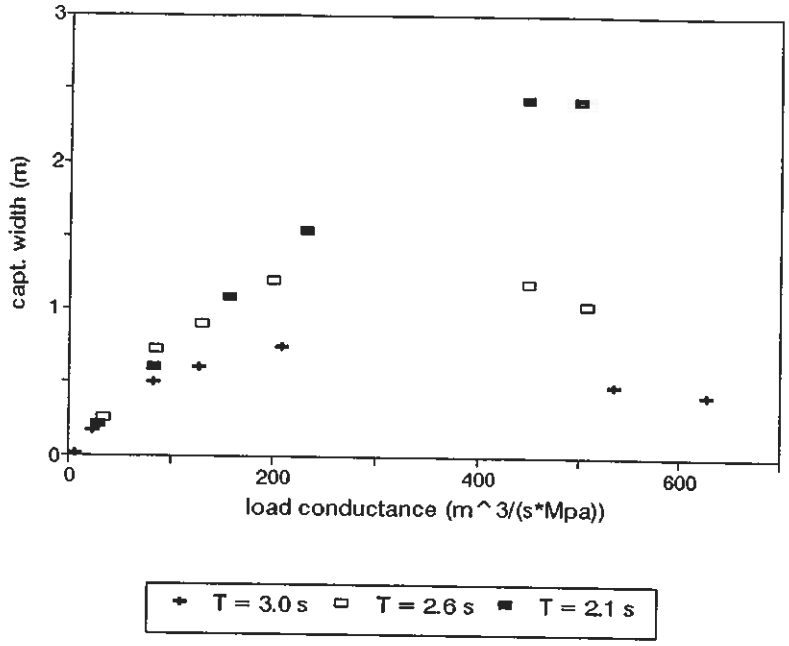

Figure 2.12: Capture width vs. load conductance for the single OWC at wave periods 2.1 s, 2.6 s and 3.0 s (setup B).

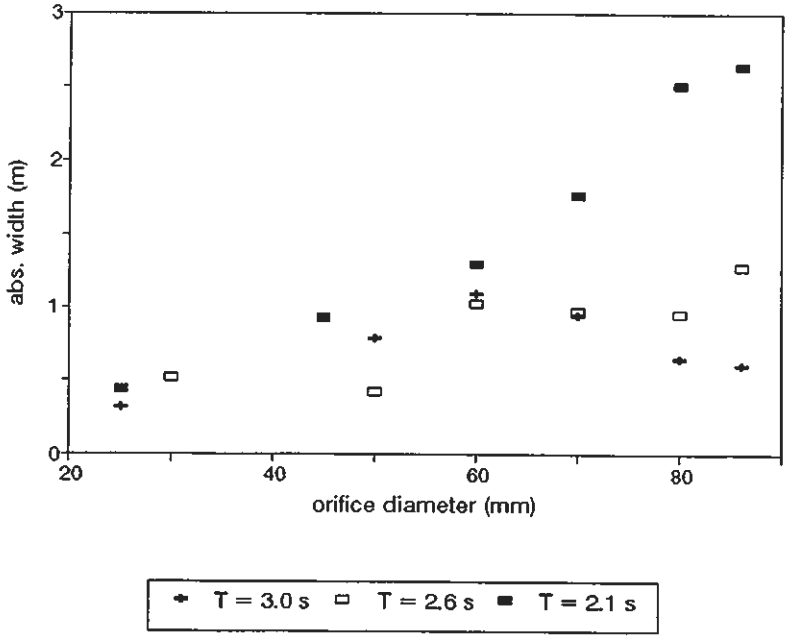

Figure 2.13: Absorption width vs. orifice diameter for the single OWC at wave periods 2.1 s, 2.6 s and 3.0 s (setup B).

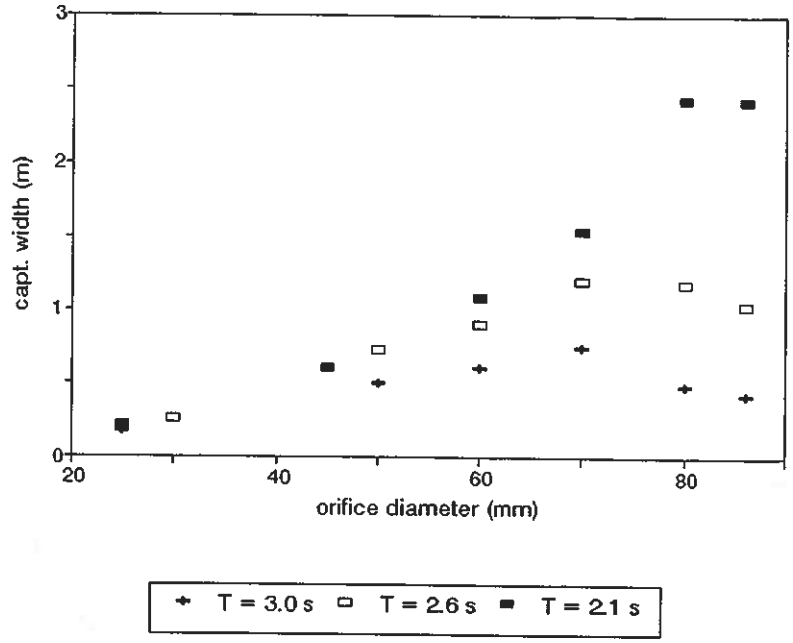

Figure 2.14: Capture width vs. orifice diameter for the single OWC at wave periods 2.1 s, 2.6 s and 3.0 s (setup B). Corresponding results for the controlled double OWC are shown in figure 2.26.

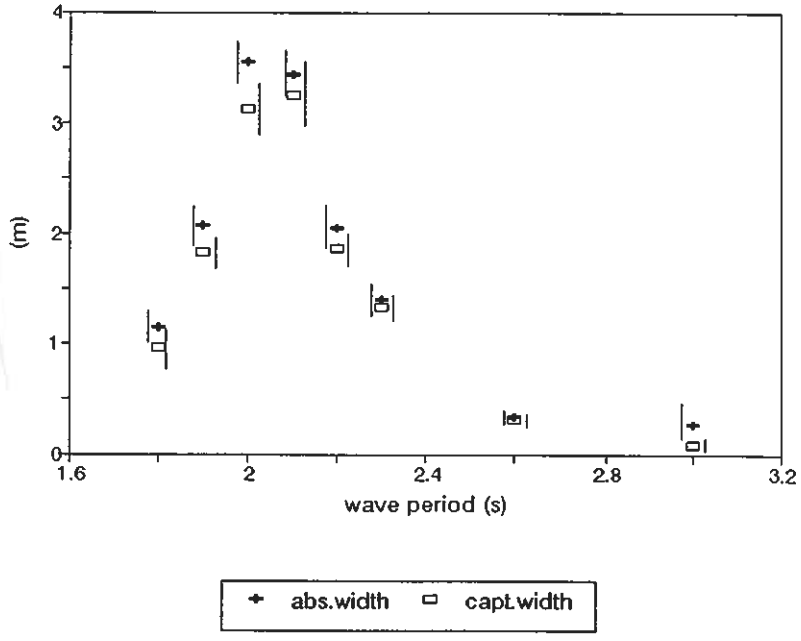

Figure 2.15: Frequency response for the single OWC when the chamber is open (setup B). The uncertainty is marked with vertical lines.

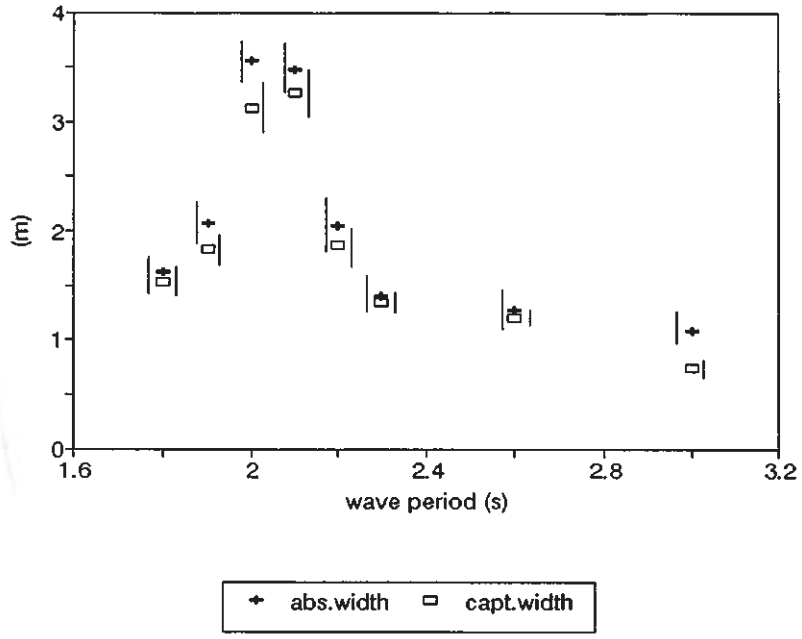

Figure 2.16: Optimum frequency response for the single OWC (setup B). The optimum orifice diameter has been found separately for the absorption width and the capture width, for each wave period. The uncertainty is marked with vertical lines. (It should be noted that the optimum orifice diameter is a function of the wave amplitude, which is attempted held constant throughout the experiment. Hence, possible variations of the incident wave is a source of uncertainty.)

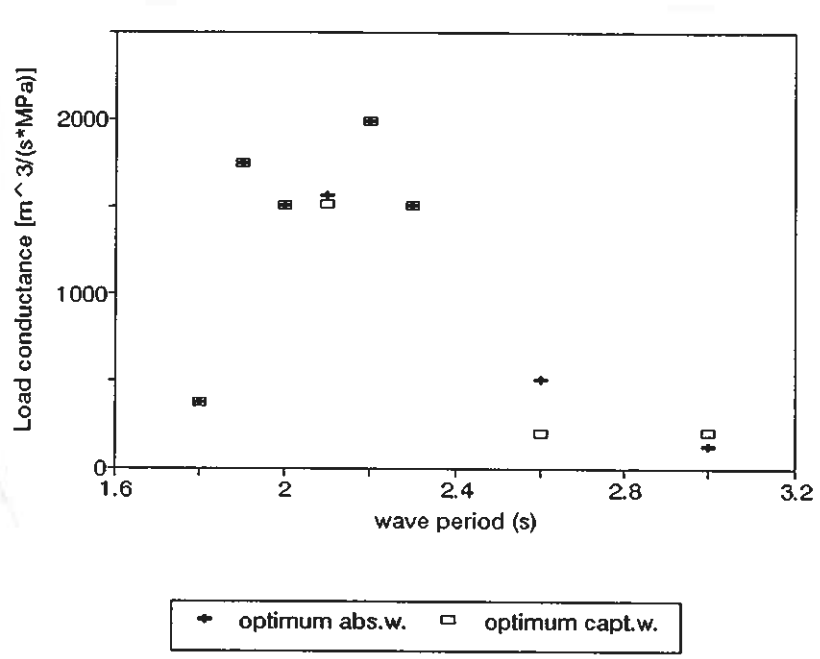

Figure 2.17: Optimum load conductance vs. wave period for the single OWC (setup B). Absorption width and capture width are optimised separately. The relative uncertainty is in the range of 6-12 %.

2.2.3 Twin OWC

One of the intentions of these experiments has been to vary one valve-control instant at a time, and thereby trying to determine how changes in these instants affect the power output. Hence, this should hopefully lead to an optimum combination of these time values.

With setup A, phase control has been carried out at several wave periods. However, due to problems with cross waves, results for only a few periods are included in this thesis. It should be noted that even these results may have been influenced by cross waves to some extent. During these experiments, the orifice diameter has been varied, as well.

With setup B, only one orifice diameter (30 mm) and one wave period (3.0 s) have been investigated for the twin OWC. Because of the smaller flume width, we assume that the influence of cross waves may be neclected for this setup (see appendix B).

The twin-OWC experiments have been hampered with several difficulties. Firstly, the incident waves have not been sufficiently reproducible. The amplitude of the incident wave has been varying somewhat from run to run, even when it was attempted to be kept constant. This may have caused a similar variation in the nonlinear losses. Besides, the optimum orifice diameter depends on the wave amplitude as well as on the wave period. Hence, this reproducibility problem is important to bear in mind when interpreting the results.

There have also appeared power output variations between runs with equal incident wave amplitudes and equal control parameters. This suggests that the conditions may not have been completely stationary during the runs (see appendix A). That is, there may have been slow variations in the incident wave, causing the measured quantities to vary at a time scale larger than one wave period. If this is true, the time elapsed from the start of the wavemaker to the start of data acquisition may have been important. The exact phase of the incident wave at this instant, may also have mattered.

In figure 2.18 results from single-OWC runs and twin-OWC runs are compared. It should be noted that the results for the twin OWC at the periods 1.8 s and 3.5 s have been measured with setup A, while all other data in this figure are obtained with setup B. Possible differences due to cross waves may have caused the results from setup A to be under-estimated, and hence, the real gain due to phase control should be larger at these periods. Besides, we do not know for any of these results whether the valve control has been optimal, although it has been fairly satisfactory. It should be noted that while the results in figure 2.18 for the wave period 1.8 s indicate a smaller capture width for the phase-controlled twin-chamber OWC than for the single OWC, the results in figure 2.22 suggest the opposite conclusion. A possible explanation may be that all the results in figure 2.22 have been obtained with setup A, while the relatively large capture width for the single-chamber case in figure 2.18 have been obtained with setup B. Table B.1 in appendix B shows that the wave period 1.8 s is very close to one of the cross wave modes at setup A. This may have made it impossible to approach the theoretical optimum capture width. Furthermore, these experimental problems may imply that the runs displayed in figure 2.22 are not representative. Besides, the obtained capture widths in this figure are small, and the relative uncertainties are large. Hence, we cannot determine whether the phase control has resulted in any significant energy gain at this particular wave period.

The wave period 3.5 s is also close to a cross wave mode at setup A. Hence, the twin-chamber result in figure 2.18 for this period may have been influenced by cross waves. However, the results in figure 2.20 seem to indicate a significant gain from the phase control. In fact, it is reasonable to expect that the relative energy increase due to the phase control could have been larger at this period (see section 2.3.1).

Figure 2.19 shows a typical example of time-series from a run where the phase control has been relatively successful. A set of criteria for a satisfactory control strategy are stated in section 2.3.

Figures 2.20 and 2.21 show capture widths for the wave periods 3.5 s and 3.0 s, respectivily. These results have been obtained from the experiments with setup A. Absorption widths have not been measured here. Figures 2.23 - 2.25 show results from setup B, where measurements of the absorption widths are included. In figures 2.20 - 2.25, each bar represents one run. The order of the bars is arbitrary. The runs selected for display represent the best achieved results, that is, runs where relatively successful phase control has been achieved. A typical set of valve operation times for such runs are as follows: 0.9 s and 1.9 s for closing and opening of valve V_1, and 2.4 s and 0.7 s for closing and opening of valve V_2. All these instants are relative to the zero up-crossing time of the incident wave within the same wave period, measured close to the barrier wall of the OWC model.

The obtained capture width in the one-chamber case is increased by about 10% with setup B as compared to setup A (figures 2.21 - 2.25). We assume this to be mainly due to the changed inlet conditions (figures 2.4 and 2.5). It may, however, also be an effect due to cross waves (see section 2.3.3).

Figure 2.26 shows that the optimum orifice diameter for the twin OWC at period 3.0 s is in the range of 30 to 45 mm, which is smaller than the corresponding results for the single-chamber case (55 to 75 mm, figure 2.14). It should be noted that the results in figure 2.26 have been obtained with setup A, while the results for the single OWC (figure 2.14) have been obtained with setup B. Hence, each obtained result in one diagram is not directly comparable with the corresponding result in the other. Besides, these figures represent crude approximations, as the displayed quantities also depend on the wave amplitude. We assume, however, that these figures provide sufficient information for a rough comparison of how the capture width vary as a function of the orifice diameter in the two cases. This comparison indicates that a full-scale twin-OWC power plant may need a turbine with a smaller load conductance, that is, a physically smaller turbine, than the more usual single OWC. This is a feature that may represent an additional economic advantage. The load conductance of an orifice is discussed more thorougly in appendix C.

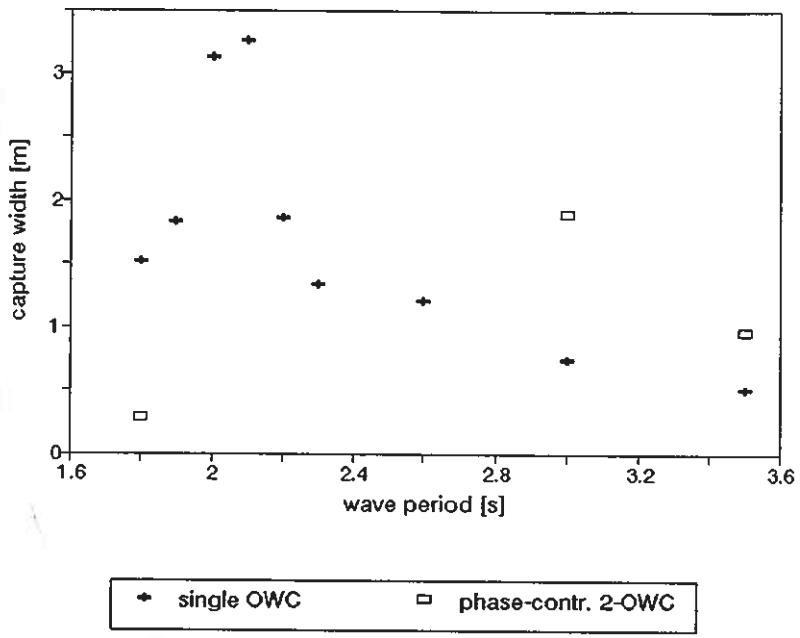

Figure 2.18: Comparison of results for the single OWC with results for the twin OWC (capture width vs. wave period). Twin-OWC results for for T = 1.8 s and both results for T = 3.5 s are obtained with setup A. All other results are from setup B.

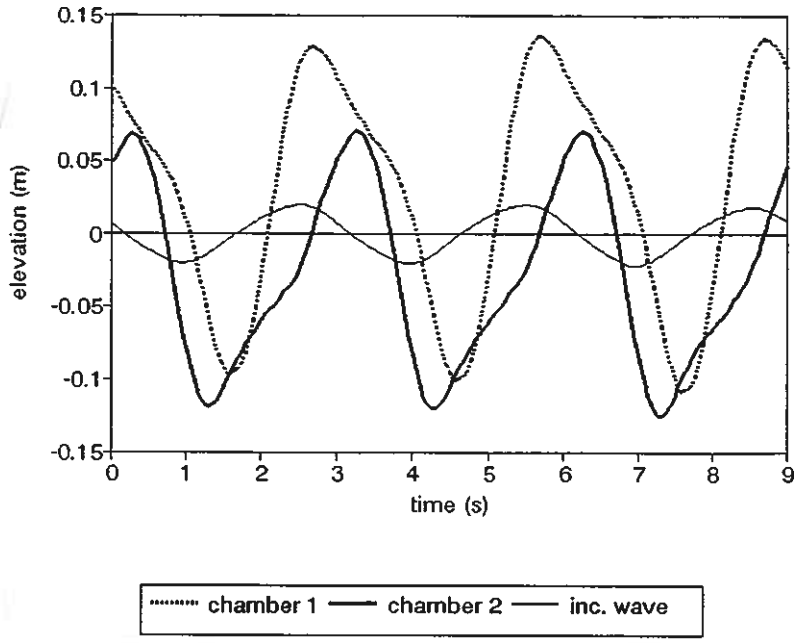

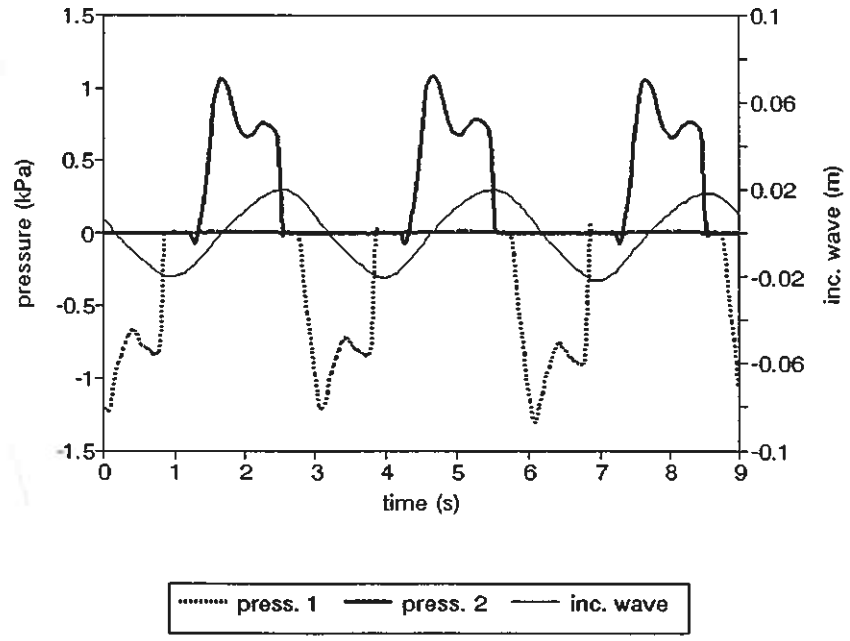

Figure 2.19: Example of successful phase control: a) time-series of exursion in the chambers and the incident wave. The incident wave is measured with gauge 3 in figure 2.5. b) time-series of chamber pressures and the incident wave. The measurements are obtained with setup B.

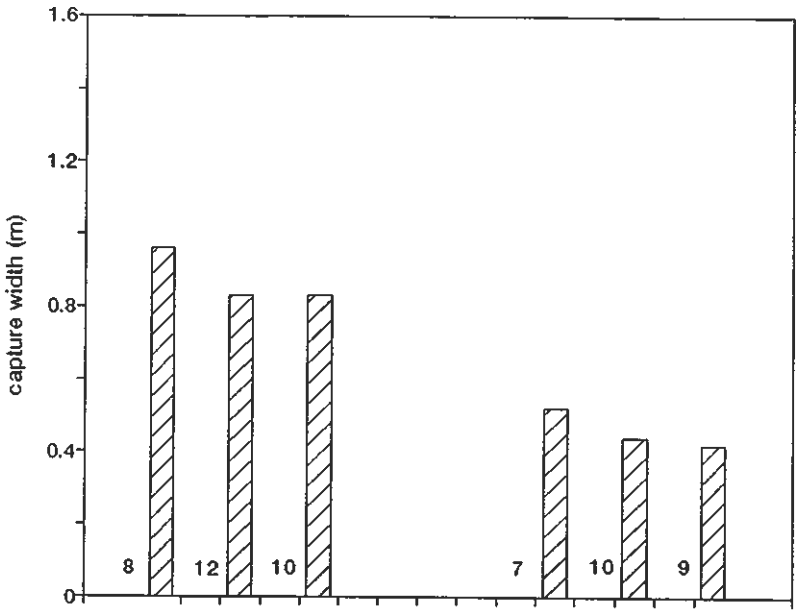

Figure 2.20: Capture width for wave period T = 3.5 s. Measurements from setup A. The bars to the left represent twin-chamber runs, and the bars to the right represent single-chamber runs. The uncertainty is given in percent.

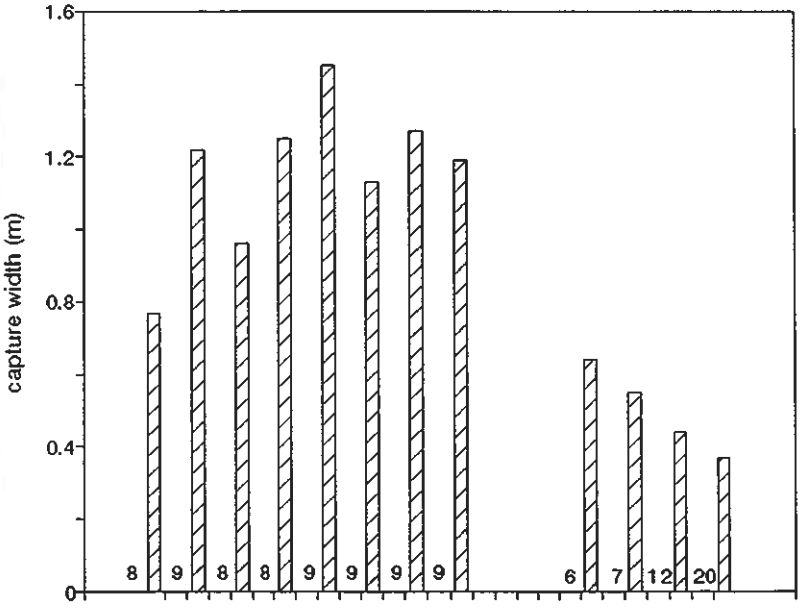

Figure 2.21: Capture width for wave period T = 3.0 s. Measurements from setup A. Twin-chamber results to the left, and single-chamber results to the right. The uncertainty is given in percent.

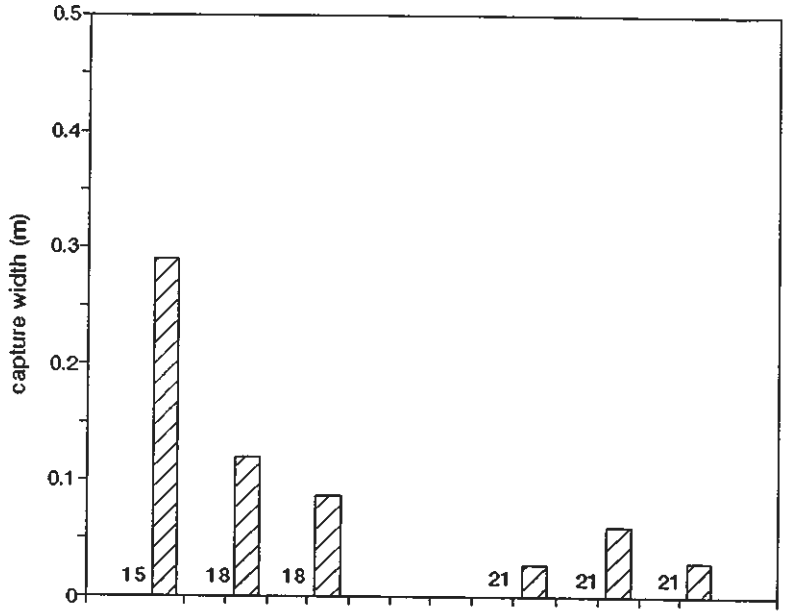

Figure 2.22: Capture width for wave period T = 1.8 s. Measurements from setup A. Twin-chamber runs to the left, single-chamber runs to the right. The uncertainty is marked with vertical lines.

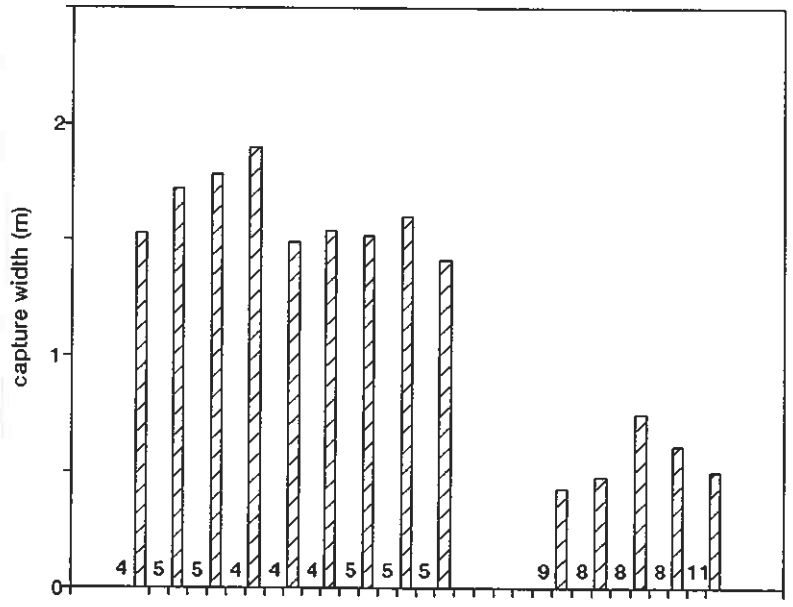

Figure 2.23: Capture width for wave period T = 3.0 s. Measurements from setup B. Twin-chamber results to the left, single-chamber results to the right. The uncertainty is given in percent.

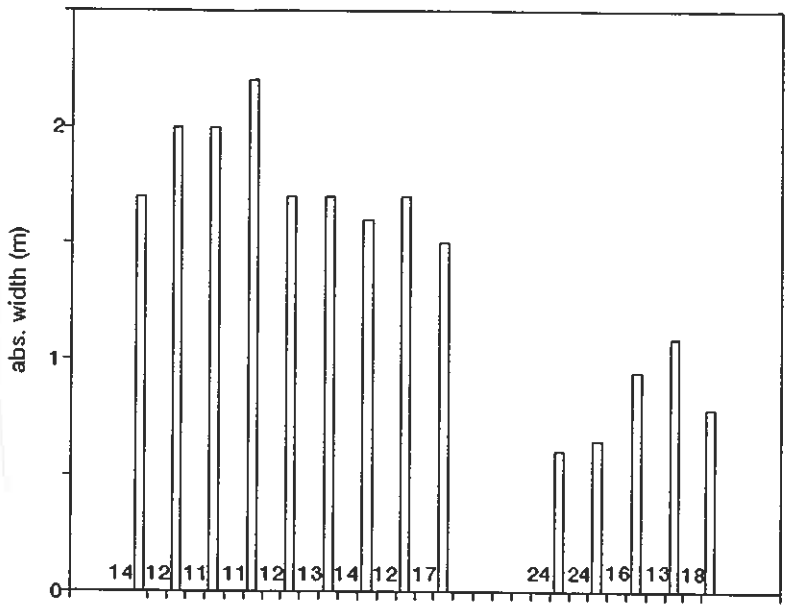

Figure 2.24: Absorption width for wave period T = 3.0 s. Measurements from setup B. Twin-chamber results to the left, single-chamber results to the right. The uncertainty is given in precent.

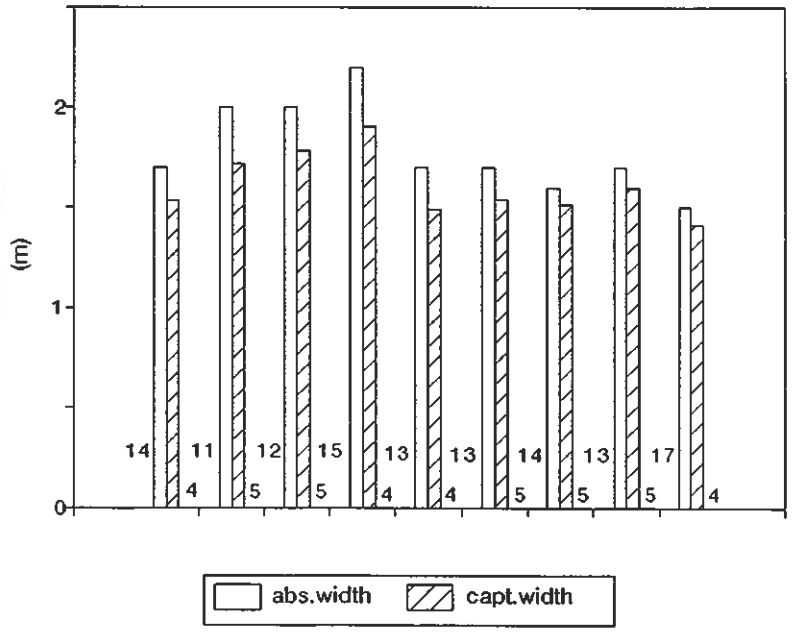

Figure 2.25: Absorption width and capture width for nine different runs of the twin OWC at wave period T = 3.0 s. Measurements from setup B. The uncertainty is given in percent.

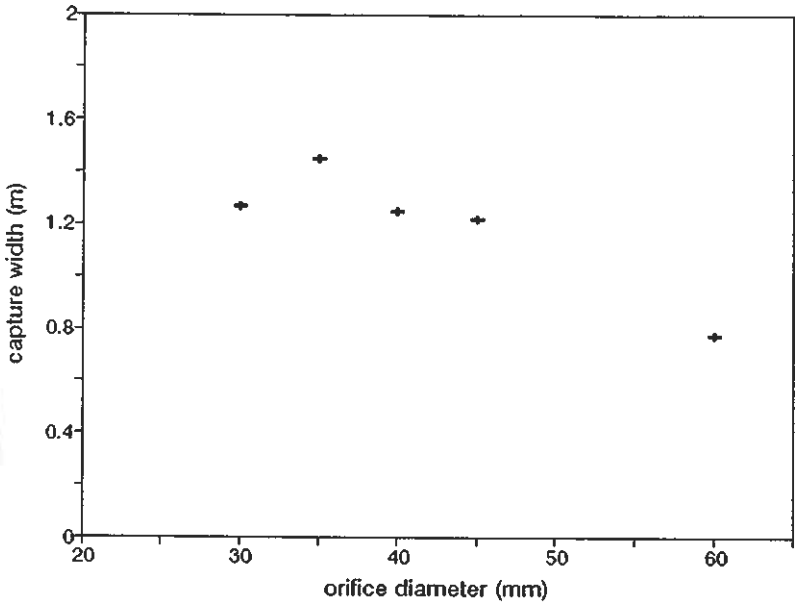

Figure 2.26: Capture width vs. orifice diameter for the twin OWC at wave period 3.0 s (setup A). Corresponding results for the single OWC are shown in figure 2.14.

2.3 Discussion

2.3.1 Discussion of results

An overall evaluation of the results indicates that, with good phase control, an increase of the absorbed energy of a factor approaching 3 can be expected at a wave period of 3.0 s, compared to a single OWC without phase control. When the wave period is 3.5 s (setup A), the increase seems to have been at least of a factor 1.7. However, because this period is close to one of the cross wave modes with setup A, we have reason to believe that this result is not optimal. Besides, from a theoretical point of view, one would expect a larger relative increase with a period 3.5 s, which is more distant from the resonance period than the case with wave period 3.0 s. These periods correspond to about 9.5 s and 11 s for a full-scale power plant. At the resonance period, there will of course be no gain from phase-controlling the system. The model's resonance period is about 2.1 s, which means approximately 6.6 s in full scale. Results from periods lower than resonance are considered to be inconclusive, due to large uncertainty and experimental problems with cross waves in the wave tank. Besides, it is not reasonable to expect a energy gain from latching the system when the natural period of the system is longer than the wave period.

We see from figures 2.11 - 2.14 that the optimum load conductance have been smaller for wave frequencies far from resonance, than for frequencies close to resonance. This is reasonable, since a large load conductance, corresponding to a small load resistance, results in a narrow bandwith. A large load resistance, however, causes the frequency response curve to be broader. Hence, at frequencies far from resonance, this broad frequency response may cause a larger output than the narrow peak resulting from a small load resistance. The broader bandwith means that the off-resonance phase is less distant from the optimum phase.

2.3.2 Control strategy

The experiments have shown that phase control by means of latching is a successful method for improving the energy capture by an OWC system. The results together with theoretical considerations suggest that the achieved energy increase due to phase control may become even larger, provided that the control is optimum, and there is no influence from cross waves. On the other hand, the optimum results for regular waves probably have to be considered as an upper limit for the efficiency increase that can be expected for real sea waves.

Even though we cannot be sure that our phase control has been optimum, the results point out a control strategy that has proved successful. According to our experimental experience so far (see figure 2.19), this strategy can be stated in terms of a set of rules:

1. The valve of the low-pressure chamber should be closed when the corresponding surface elevation is maximum.
2. The valve of the high-pressure chamber should be closed when the corresponding surface elevation is minimum.

3. The valves should be opened in order to make the average of the oscillation velocities in the two chambers in phase with the incident wave.

For experiments with a wave period of 3.0 s, the last rule requires that the low-pressure chamber should be opened approximately 1.5 s before the incident wave elevation is maximum, and the high-pressure chamber should equivalently be opened $\sim$ 1.5 s before the minimum of the incident wave. For regular waves the above rules ensure that only one chamber is held closed at a time. For irregular waves this is not necessarily the case, and hence, high-frequency pressure peaks may arise in the chambers. Such peaks will probably be unefficiently utilised in a real air turbine. Also, if the incident waves become large, we may want to avoid such peaks, since they can entail severe shock forces on the structure. The pressure peaks may be reduced if we modify the rules 1 and 2 in the following way: the valve of the low-pressure chamber should in practice be closed *shortly after* the elevation of the water surface has had its maximum position, and the valve of the high-pressure chamber should correspondingly be closed shortly after the minimum position of the surface elevation. Also, within each wave period, the valve which does not close first after the zero up-crossing of the incident wave, should close at the instant when the chamber surfaces have equal absolute velocities and are moving in opposite directions [54].

2.3.3 Power losses

Before discussing various losses, we wish to remark that our strategy is to maximise the converted useful power, rather than to minimise the various losses. In some cases, it pays to increase the power losses, if this results in an increase of the useful power. Of course, in such a case more energy is absorbed from the waves.

When valve operation is applied, the two water flows through either OWC mouth will be out of phase. This introduces shear forces between them, and possibly, vortex shedding. The shape of the bisecting wall, which in our case is rather sharp-edged, also comes into play. This may give rise to turbulence when the wave amplitude is of the same order of magnitude as the radius of curvature of the wall edge. For our model, this may happen even at relatively small amplitudes. Further, the abrupt changes in the velocity of the water flows, due to the opening and closing of the valves, may also lead to vortex shedding, and hence, contribute to the total losses. Obviously, the amount of these losses will depend on the valve control. Furthermore, these loss mechanisms are nonlinear, and the amount of loss will hence also depend on the amplitude of the incident wave.

However, it is difficult to draw clear conclusions about the connection between the incident amplitude and loss effects. This is partly due to experimental uncertainty, and partly because the load conductance also depend on the incident wave amplitude (see appendix C). The relative uncertainty of the capture width may be as large as 20 %. Results suggest, however, that losses are in the order of 10 - 30 % of the incident power, depending on the actual valve control.

In addition to the frictional and turbulent losses in the water, there is also a certain amount of loss due to the air valves. Firstly, each valve will act as a flow restriction even when it stays fully open. Secondly, power loss will result when a valve is opened

suddenly, and the pressure difference across it is non-zero [55]. The amount of this loss will depend on the instants of valve operation.

In this work we estimate the valve losses by computing the pneumatic energy associated with the volume flux through the valves when each of them are open. Neglecting air compressibility, we may write

$$Q_{v1}(t) = \alpha_1(t)(Q_1(t) + Q_{or}(t)) \tag{2.74}$$

$$Q_{v2}(t) = \alpha_2(t)(Q_2(t) - Q_{or}(t)) \tag{2.75}$$

The sum of Q_{v1} and Q_{v2} then becomes

$$\begin{aligned} Q_v(t) = Q_{v1}(t) + Q_{v2}(t) &= \alpha_1(t)\, Q_1(t) + \alpha_2(t)\, Q_2(t) \\ &= S_k(\alpha_1(t)\, u_1(t) + \alpha_2(t)\, u_2(t)) \end{aligned} \tag{2.76}$$

Here, Q_{or} is the volume flux through the orifice, while Q_1 and Q_2 are the volume flux measured at the water surface in each of the chambers. Further, the functions $\alpha_1(t)$ and $\alpha_2(t)$ describe the state of each valve, that is, $\alpha_1(t) = 0$ means that valve no. 1 is closed, while $\alpha_1(t) = 1$ means that it is fully open. Hence, each term in equation (2.76) is non-zero only if both the velocity and the corresponding valve function are non-zero. The approximate valve loss during one wave period is then given as

$$W_v = S_k \int_0^T (\alpha_1(t)u_1(t)p_1(t) + \alpha_2(t)u_2(t)p_2(t))\, dt \tag{2.77}$$

Experimental analysis based on this expression indicates a valve loss in the order of $\sim$ 10 % of the pneumatic work. For some of the runs, this value differs significantly from the measured difference between the pneumatic energy and the orifice energy. Due to this fact, the orifice energy is omitted in the presented results. The theoretical relations are, however, considered in appendix D. It should be noted that because the amount of valve loss depend on the instants of valve operation, the strategy providing an optimum useful power may differ from the strategy found in this work, since we have considered the pneumatic power, and not the useful power.

As mentioned in chapter 2.2.3, the capture width in the single-OWC case is increased by about 10% with setup B as compared to setup A. This increase is somewhat greater at wave periods close to resonance than at other periods. This suggests that the increase is caused by reduced losses due to the changed inlet conditions, since the chamber excursion amplitude has its maximum value at resonance, and viscous and turbulent losses become more important as the excursion amplitude of the water column increases. However, the different capture widths obtained in the two setups may also be a result of cross waves in the tank in setup A (see appendix B). In setup B, such cross waves have probably been of small importance.

Another fact that may cause the results to differ somewhat in the two setups, is that the water may be considered as *deep* for all wave periods with setup A, that is, $kh \ll 1$. This has not been the case for the flume of setup B.

2.3.4 Experimental problems and uncertainty

During these experiments we have tried to determine the optimal control strategy directly, by varying the valve operation times one at a time. Thus, the aim has been to optimise the energy output with respect to four coupled parameters. In addition to being a complex experimental task, this work have also, as mentioned in section 2.2.3, been hampered with certain problems related to experimental reproducibility. It has, in other words, been practically difficult to control all significant parameters in the total setup. These problems have to some extent led to ambigious results, and it has not been possible to determine an optimal control strategy as accurate as we hoped for. The reproducibility problems have also made it difficult to investigate phenomena such as power loss effects, and sensitivity of the power output with respect to the valve operation time and load conductance.

There may also have been cross waves in the flumes, disturbing the obtained results. Cross waves are possible, provided that $n\lambda \leq 2d$ (see (B.7)). Here, n is a positive integer, λ is the wavelength, and d is the flume width. This means that cross waves have probably been present in many of the runs with setup A, because the flume has been rather wide (10 m). In setup B, we would normally not expect the presence of cross waves, because the flume width is smaller than half the wavelength of the incident wave. However, due to the phase control, the wave radiated from the model have contained components with higher frequencies. Such higher harmonics may have satisfied the inequality (B.7), and thus made cross waves possible. In the results concerning setup B in this chapter, we have however not taken such influences into consideration.

The experimental problems mentioned above have made it desirable to develope an alternative approach, allowing a check of the obtained results. The transient experiments presented in chapter 3 constitute one part of such an approach.

2.3.5 Validity for a full-scale power plant

An important question at this point, is to what extent these results do apply to a full-scale power plant operating in a real sea state. There are several features that call for caution when implementing the results to a real power plant. One such feature concerns the scaling itself. The hydrodynamic parameters will be scaled correctly only if the stationary pressure is being scaled, too. This means that the stationary pressure during the 1:10 model experiments should not be equal to the atmospheric pressure, but rather ten times lower (which is not easy to achieve in a laboratory). As seen from appendix C, it would have been possible to compensate for the ten times too big ambient air pressure p_a by having a ten times larger air volume V_0. But this would have been impractical in the experiment. The extra effort this would cause, did not seem to be necessary concerning the main purposes of our experiment.

Another important fact is that we have only been using orifices as load elements, and hence, certain features of a real turbine are not included in the model. If, for instance, the pneumatic power exceeds a certain level, a real turbine may stall. That is, the high ratio of air flow speed to turbine rotation speed causes the air to separate at the low-pressure side of the turbine blades. As a result, the turbine efficiency drops considerably. A Wells turbine typically needs a minimum of time to recover to a normal state of operation after

stalling. This may cause the turbine to be unefficient in utilising high frequencies and large amplitudes (peaks) of the pneumatic power.

We have throughout the experiment neglected the effect of air compressibility in the chambers. This is a resonable approximation in the model case. In full scale, however, this term may be significant.

Lastly, we should remember that the full-scale power plant will be exposed to irregular waves. This probably means a somewhat lower efficiency, and what is more important, it requires an accurate method of predicting the incident waves in order to approach the theoretical optimum.

Chapter 3

Transient wave experiments

In this chapter we consider a transient wave radiating from the OWC model on otherwise calm water. The duct between the chambers is closed, while one of the air valves is open and the other is initially closed. A stationary pressure is applied to the closed chamber, and shortly ~~before~~ after the start of the data acquisition, the corresponding air valve is opened. Hence, the water columns start to oscillate, and a wave is radiated from the model. From this experiment we can calculate the impulse response matrix of the system. This matrix is subsequently used to determine frequency-domain hydrodynamic parameters. It may also be used in the formulation of a time-domain mathematical model of the system.

3.1 Theory

3.1.1 Radiation interaction due to an applied pressure transient

The method to be described here was first utilised in an earlier experimental work performed by Sarmento on a single OWC [56]. In the present work the method has been generalised to the case of a twin-OWC system. In these experiments there is no incident wave, and valve V_1 (see figure 3.1) is open at all times. Thus, eq. (2.52) may be written

$$\tilde{\mathbf{Q}}(\omega) = \tilde{\mathbf{Q}}_r(\omega) = -\mathbf{Y}(\omega)\,\tilde{\mathbf{p}}(\omega) = -\begin{bmatrix} Y_d(\omega) & Y_x(\omega) \\ Y_x(\omega) & Y_d(\omega) \end{bmatrix} \begin{bmatrix} 0 \\ \tilde{p}_2(\omega) \end{bmatrix} \tag{3.1}$$

The tilde denotes the Fourier transform of a general time function (not necessarily periodic). By performing the inverse Fourier transform, the equations may be transfered to the time domain

$$\begin{bmatrix} Q_1(t) \\ Q_2(t) \end{bmatrix} = -\int_{-\infty}^{\infty} \begin{bmatrix} y_x(\tau) \\ y_d(\tau) \end{bmatrix} p_2(t-\tau)\,d\tau \equiv -\begin{bmatrix} y_x(t) \\ y_d(t) \end{bmatrix} * p_2(t) \tag{3.2}$$

It follows from this description that $-y_d$ and $-y_x$ are impulse-response functions of the system. Since it is experimentally difficult to apply an impulse pressure to the system, we shall determine these functions indirectly, by first obtaining the step response experimentally. We introduce the step response functions $h_x(t)$ and $h_d(t)$, which are

related to the impulse response functions through the relations $dh_x(t)/dt = -y_x(t)$ and $dh_d(t)/dt = -y_d(t)$.

The physical interpretation of the step response functions $h_x(t)$ and $h_d(t)$ are the volume fluxes $Q_1(t)$ and $Q_2(t)$ created in the chambers as a result of a unit pressure step function in chamber no. 2. A finite pressure step cannot cause an infinite acceleration of any of the interior water surfaces. The velocities of the surfaces and the volume fluxes resulting from this pressure step, will hence have to be continuous at every instant. In other words, the step responses $h_x(t)$ and $h_d(t)$ are continuous functions.

Utilising that the impulse response functions are causal, that is, $y_x(t) = 0$ and $y_d(t) = 0$ for all $t < 0$, eq. (3.2) may be written

$$\begin{bmatrix} Q_1(t) \\ Q_2(t) \end{bmatrix} = \frac{d}{dt}\begin{bmatrix} h_x(t) \\ h_d(t) \end{bmatrix} * p_2(t) = -\begin{bmatrix} h_x(0^+) \\ h_d(0^+) \end{bmatrix} p_2(t) + \int_0^\infty \begin{bmatrix} h_x(t-\tau) \\ h_d(t-\tau) \end{bmatrix} \frac{dp_2}{d\tau}(\tau)\, d\tau \tag{3.3}$$

We now assume that the pressure applied to chamber no. 2 is an ideal step function:

$$p_2(t) = \left\{ \begin{array}{ll} p_0 & , t < 0 \\ p_0/2 & , t = 0 \\ 0 & , t > 0 \end{array} \right\} = p_0 H(-t) \tag{3.4}$$

where $H(t)$ is the Heaviside step function. Then we have $dp_2(t)/dt = -p_0\delta(t)$. For $t \geq 0$, equation (3.3) then gives

$$\begin{bmatrix} h_x(t) \\ h_d(t) \end{bmatrix} = -\frac{1}{p_0}\begin{bmatrix} Q_1(t) \\ Q_2(t) \end{bmatrix} \qquad , t \geq 0 \tag{3.5}$$

For $t < 0$, equation (3.3) becomes

$$\begin{bmatrix} Q_1(t) \\ Q_2(t) \end{bmatrix} = -p_0\begin{bmatrix} h_x(0^+) \\ h_d(0^+) \end{bmatrix} \qquad , t < 0 \tag{3.6}$$

Since $Q_1(t)$ and $Q_2(t)$ are obviously zero for $t < 0$, (3.6) means that $h_x(0^+) = 0$ and $h_d(0^+) = 0$. Further, the definitions $dh_x(t)/dt = -y_x(t)$ and $dh_d(t)/dt = -y_d(t)$ together with the fact that $y_x(t)$ and $y_d(t)$ are causal functions, mean that $h_x(t)$ and $h_d(t)$ have to be constants for all negative time values. Hence, it follows from continuity:

$$h_x(t) = 0 \qquad , t \leq 0 \tag{3.7}$$

$$h_d(t) = 0 \qquad , t \leq 0 \tag{3.8}$$

Now, returning to the case of a general pressure function $p_2(t)$, eq. (3.3) may finally be written

$$\begin{bmatrix} Q_1(t) \\ Q_2(t) \end{bmatrix} = \begin{bmatrix} h_x(t) \\ h_d(t) \end{bmatrix} * \frac{dp_2}{dt}(t) \tag{3.9}$$

By measuring the initial pressure and the volume flux in both chambers, $h_x(t)$ and $h_d(t)$ can be derived, and hence $y_x(t)$, $y_d(t)$ can be obtained by differentiation of $h_x(t)$ and $h_d(t)$. Further, Fourier transforming $y_x(t)$ and $y_d(t)$ gives $Y_x(\omega)$ and $Y_d(\omega)$, which

are the elements of the radiation admittance matrix. This matrix is of great importance when investigating a WEC, as it shows the system's ability to radiate waves, and hence, to absorb energy at various wave frequencies.

The volume flux in the chambers is derived experimentally from the relation $Q_k(t) = S_k ds_k(t)/dt$, where s_k denotes the water excursion in chamber no. k. It should be noted, however, that the measured time series $s_2(t)$ have to be corrected for the time values $t < 0$. The FFT program considers a periodic extension of each signal taken from $t = 0$ to $t = T_{reg}$. The actual excursion in chamber no. 2 is however non-zero for all $t < 0$:

$$s_2(t) = s_{2-}(t) + s_{2+}(t) \tag{3.10}$$

where

$$s_{2-}(t) = \left\{ \begin{array}{ll} s_0 & , t < 0 \\ s_0/2 & , t = 0 \\ 0 & , t > 0 \end{array} \right\} = s_0 H(-t) \tag{3.11}$$

and

$$s_{2+}(t) = \left\{ \begin{array}{ll} 0 & , t < 0 \\ s_0/2 & , t = 0 \\ s_2(t) & , t > 0 \end{array} \right. \tag{3.12}$$

Here, $s_0 = -p_0/\rho g$ is the initial water level in chamber no. 2.

The step functions involved are discussed more closely in section 3.3. The elements of the radiation admittance matrix becomes

$$Y_x = -\frac{S_k}{p_0}\omega^2 \mathcal{F}\{s_{1+}(t)\} \tag{3.13}$$

$$Y_d = -\frac{S_k}{p_0}\omega^2 \mathcal{F}\{s_{2+}(t) + s_{2+}(0)H(-t)\} \tag{3.14}$$

where $\mathcal{F}$ denotes the Fourier transform, while $s_{1+}(t)$ and $s_{2+}(t)$ are the recorded chamber excursions for $t > 0$. Further, $H(t)$ is the Heaviside step function.

The time integrals of the quantities $Q_1(t)$ and $Q_2(t)$ taken from 0 to ∞, must be equal to the initial volum displacement in the chambers, caused by the applied air pressure:

$$\int_0^\infty \left[\begin{array}{c} Q_1(t) \\ Q_2(t) \end{array} \right] dt = \left[\begin{array}{c} 0 \\ S_k s_0 \end{array} \right] \tag{3.15}$$

where S_k is the surface area of each chamber, and $s_0 = -p_0/(\rho g)$ is the initial displacement of the water surface in chamber no. 2. Further, p_0 is the initial applied pressure, ρ is the water density, and g is the acceleration of gravity. These are known quantities, and hence, equation (3.15) provides a check of the measured results [57]. The experiments and the obtained results are described in section 3.2.

3.1.2 A time-domain mathematical model

Now, having determined the impulse response functions of the system, we utilise this information to develope a time-domain mathematical model, allowing simulation of the system. The impulse response functions are included in the model as kernels in convolution integrals. In fact, the frequency-domain volume flux balance in eq. (2.52) may be expressed in the time domain as

$$\begin{bmatrix} Q_1(t) \\ Q_2(t) \end{bmatrix} = q_{e1}(t)\begin{bmatrix} 1 \\ 1 \end{bmatrix} * \eta_i(0,t) - \begin{bmatrix} y_d(t) \\ y_x(t) \end{bmatrix} * p_1(t) - \begin{bmatrix} y_x(t) \\ y_d(t) \end{bmatrix} * p_2(t) \tag{3.16}$$

In terms of the step response functons $h_d(t)$ and $h_x(t)$, equation (3.16) becomes

$$\begin{bmatrix} Q_1(t) \\ Q_2(t) \end{bmatrix} = q_{e1}(t)\begin{bmatrix} 1 \\ 1 \end{bmatrix} * \eta_i(0,t) + \begin{bmatrix} h_d(t) \\ h_x(t) \end{bmatrix} * \frac{dp_1}{dt}(t) + \begin{bmatrix} h_x(t) \\ h_d(t) \end{bmatrix} * \frac{dp_2}{dt}(t) \tag{3.17}$$

Note that Q_1 and Q_2 are the volume fluxes at each interior water surface. We now introduce the symbols Q_{c1} and Q_{c2}, denoting the total volume flux out of each chamber. Hence, we have

$$\begin{bmatrix} Q_{c1}(t) \\ Q_{c2}(t) \end{bmatrix} = \begin{bmatrix} Q_1(t) \\ Q_2(t) \end{bmatrix} - \frac{V_0}{\gamma p_a}\frac{d}{dt}\begin{bmatrix} p_1(t) \\ p_2(t) \end{bmatrix} \tag{3.18}$$

where the last term is due to air compressibility. In our model scale, this term will be of negligible importance, but for a full-scale power plant, it may be significant. Here, V_0 is the time-average air chamber volume, γ is the adiabatic exponent, and p_a is the atmospheric pressure. This term follows from linearising the adiabatic relation $pV^\gamma = K$, where K is a constant [58].

One way to obtain the function $q_{e1}(t)$ is to derive the inverse Fourier transform of $\tilde{q}_{e1}(\omega)$, which may be found from the radiated wave, using the reciprocity relation (a generalised Haskind relation):

$$\tilde{q}_{e1}(\omega) = \frac{d\rho g^2 D(kh)}{\omega} a^- \tag{3.19}$$

This relation was derived by Evans [34] for the two-dimensional case. It is applicable in our case if there are no influence from cross waves. Here, $D = D(kh)$ is the previously defined depth function (see eq. (2.3)). Further, a^- is called the *far-field coefficient*. This coefficient is defined by the asymptotic relation [36]:

$$\tilde{\eta}_r(x_0,\omega) \sim a^- \tilde{p}_2(\omega)\, e^{-ik|x_0|} \tag{3.20}$$

Here, $\tilde{\eta}_r(x_0,\omega)$ is the Fourier transform of the radiated wave measured a distance $x_0 \sim 8m$ from the OWC model, and $\tilde{p}_2(\omega)$ is the Fourier transforms of the dynamic chamber pressure. The radiated wave is here defined in terms of our model II. That is, it is proportional to the dynamic air pressure in the chamber. However, in this experiment there is no incident wave, and hence, no diffracted wave either. From this reason, the radiated wave in this case is equal to the total outgoing wave. Moreover, we have

$$\eta_r(t) = \eta_{r,I}(t) = \eta_s(t) \tag{3.21}$$

where $\eta_{r,I}$ is the radiated wave defined in terms of model I, as presented in section 2.1.1, and η_s is the total outgoing wave from the OWC in the general case.

The relation (3.20) is only valid when the radiated wave is measured in the far field, a sufficiently large distance x_0 from the origin $x = 0$, which is chosen to coincide with the front wall of the OWC.

Because of influence from cross waves in the flume, and large relative uncertainty in the radiated wave, the excitation volume flux coefficient is not derived on experimental basis. Instead, it is calculated from the excitation force coefficient for one chamber, $f_{e1,I}(\omega)$, which may be determined approximately by means of theoretical relations [59]. According to these relations, we have

$$f_{e1,I}(\omega) = \rho g d \frac{sinh(kh - ka) - sinh(kh - kb)}{k\, cosh(kh)} \tag{3.22}$$

Here, a is the vertical distance from the mean water level to the upper edge of the mouth, b is the corresponding distance to the lower edge of the mouth, d is the width of one chamber, and h is the water depth outside the chambers. From $f_{e,I}$, we may derive q_e as follows (see eqs. (2.45) and (2.48)):

$$q_{e1} = \frac{f_{e1,I}\, Y}{2S_k} \tag{3.23}$$

or, alternatively (see eqs. (2.39), (2.43) and (2.44)):

$$q_{e1} = \frac{f_{e1,I}(Y_d + Y_x)}{S_k} \tag{3.24}$$

Here, Y is the radiation admittance when the system acts as a single chamber, while Y_d and Y_x are the diagonal element and cross element of the twin-OWC radiation admittance matrix, respectively. Note that the relations (3.23) and (3.24) are good approximations only if the frequency is so small that the interior water surfaces oscillate as horizontal plane surfaces.

Combining (3.23) and (3.24) we also obtain the relation

$$Y = 2(Y_d + Y_x) \tag{3.25}$$

The left side of eq. (3.18) may be expressed as

$$Q_{c1}(t) = Q_{V1}(t) - Q_T(t) \tag{3.26}$$

$$Q_{c2}(t) = Q_{V2}(t) + Q_T(t) \tag{3.27}$$

where $Q_{Vk}(t) = \alpha_k(t)\, K_V\, sgn(p_k(t))\, \sqrt{|p_k(t)|}$ is the flux through valve V_k $(k = 1, 2)$ [50], and $Q_T(t)$ is the turbine air flow. Depending on the turbine characteristics, this will in general be a nonlinear function of $p_2 - p_1$. The valve function $\alpha_k(t)$ is equal to unity when valve V_k is fully open, and zero when it is closed. Further, K_V is a constant of the valve.

The expressions (3.17 - 3.18) together with (3.26 - 3.27) constitute our time-domain model. The dynamic air pressure p_1 and p_2 can be calculated for each instant t. Because of

the nonlinearity, the calculations have to be carried out by means of successive iterations, e.g. the Newton-Raphson method [60].

A computer program for accomplishing these calculations is presently being developed as a separate project. In this program the valve operation times, the incident wave and the load impedance (or orifice diameter) may be freely chosen, while the impulse response functions are obtained experimentally, as previously described. Simulation runs of this program may be used to check the experimental results presented in chapter 2. It can also be a helpful tool to determine the optimum load admittance, and to investigate various control strategies.

3.2 Experiments and results

3.2.1 Setup and measurements

These experiments have been performed with setup B (see figure 2.5). By means of a vacuum cleaner, a stationary pressure p_0 is initially established in one of the air chambers (chamber 2, see figure 3.1). An adjustable leak valve is mounted at the top plate of the model, to permit adjustment of the pressure to a desired initial level.

During the transient experiments the duct between the chambers is closed, and valve V_1 is open all the time. The air creating the stationary pressure is supplied through a hose connected to chamber no. 2, while air valve V_2 is closed. By means of an electric signal, data acquisition is initiated and, one or two sample periods later, valve V_2 is opened. This is achieved by operating just one switch for both purposes, with the appropriate time delay implemented in the electronic circuit. The delay is necessary in order to admit the initial pressure level to be recorded by the logging program. When valve V_2 opens, the water columns start to oscillate freely, and a wave is radiated from the model. Signals of the initial pressure, the radiated wave and the chamber excursions are logged and stored in a computer. From these measurements, the step response functions $h_d(t)$ and $h_x(t)$ as given by equation (3.5), are derived.

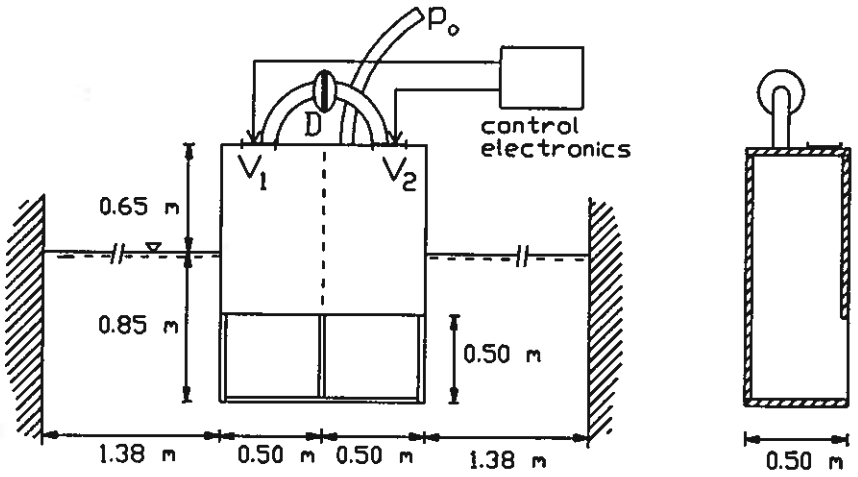

Figure 3.1: Model of twin OWC (front view and side view (cut section)). The air valves are labeled V_1 and V_2, while D is the duct connecting the two air chambers. The front of the model is flush with the vertical end wall of the flume.

Additional experiments have been performed, where the system is working as a single OWC. Then the duct between the chambers is open, and both valves are initially closed and then opened simultaneously.

Several runs have been performed both for the twin-chamber system and the single-chamber system, each with different initial chamber pressures. The results presented in the following are selected from runs considered to be representative.

Each run has been logged with a sampling period of 35.2 ms and a recording time of 36.0 s. This results in 1024 samples, which is convenient for FFT analysis.

The registration time should ideally be as long as possible, but in practice the data logging must be terminated before any reflections from the wavemaker reach the wave gauges. This restriction results in a truncation of all time series, which in turn leads to a certain error. To estimate the quantity of this error, the time series have been extended to infinity by means of assumed mathematical expressions considered to be a more relevant approximation than just zero. These extensions are discussed in section 3.3. Measured quantities with the assumed extensions are shown in figures 3.2 to 3.4. The extensions are included when deriving the hydrodynamic parameters in the frequency domain.

The elements of the step response matrix are shown in figure 3.5 for $t < 36$ s. The diagonal element of the step response shown in figure 3.5 has a somewhat irregular behaviour. The amount of such irregularities has been varying from run to run, depending on the initial pressure. Since the step response is proportional to the volume flux, and hence, obtained by time derivation of the chamber excursion, it is rather sensitive with respect to disturbances on the water surfaces. One source of such disturbances is interior oscillations, which are mentioned in section 3.3.

The step response function for the fsingle-chamber case is shown in figure 3.6 for $t < 36$ s.

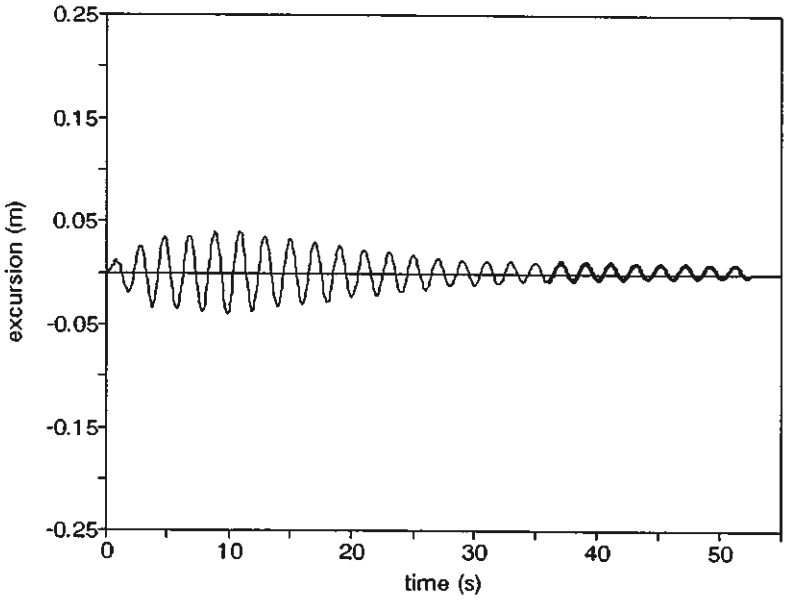

Figure 3.2: Elevation in chamber 1. Measured values for $t < 36$ s. Assumed extension for $36 < t < \infty$ s is shown in bold line style for the time interval $36 < t < 52$ s.

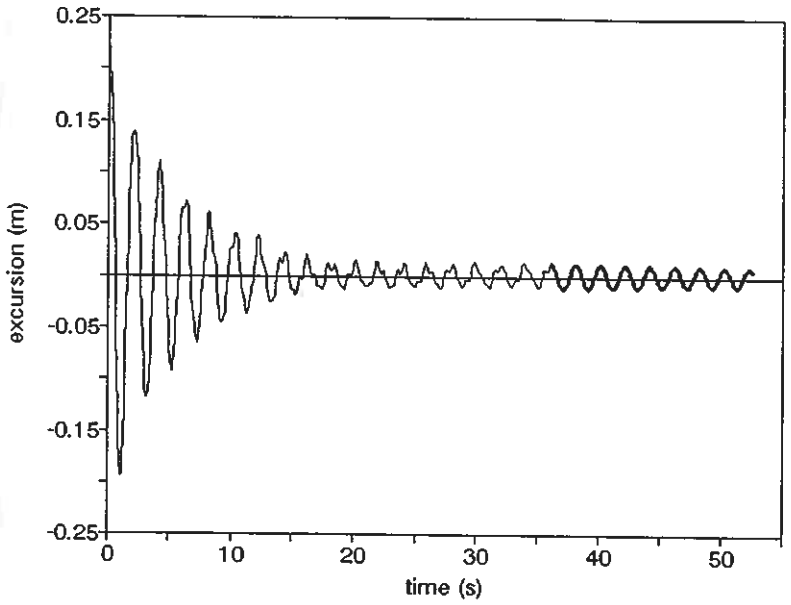

Figure 3.3: Elevation in chamber 2. Measured values for $t < 36$ s. Assumed extension for $36 > t > \infty$ s is shown in bold line style for the time interval $36 < t < 52$ s.

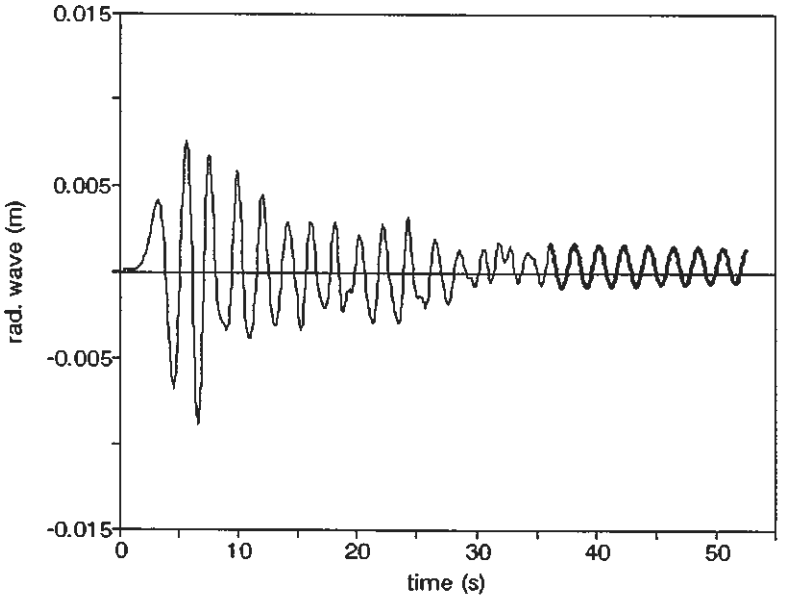

Figure 3.4: Radiated wave. Measured values 8 meters from the model, for $t < 36$ s. Assumed extension for $36 > t > \infty$ s is shown in bold line style for the time interval $36 < t < 52$ s.

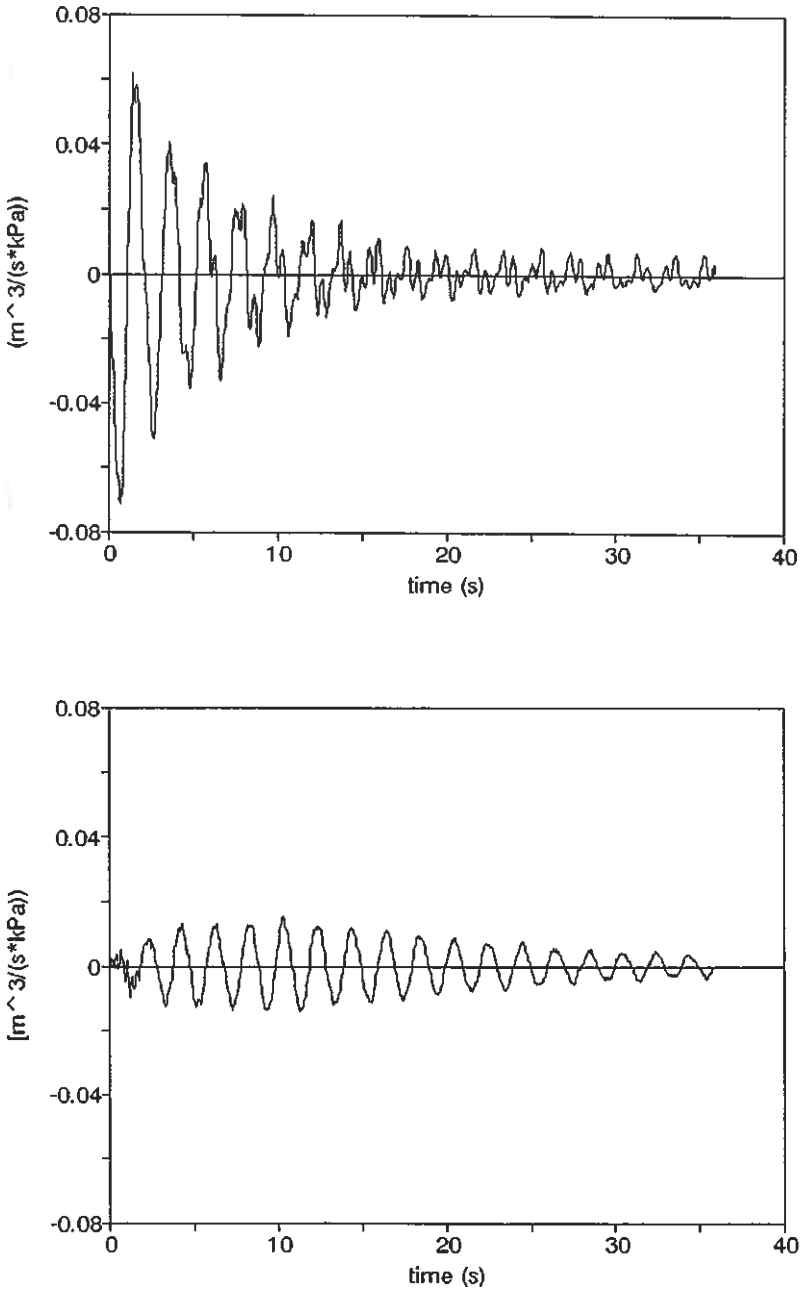

Figure 3.5: Step response. a) Diagonal term $h_d(t)$. b) Cross term $h_x(t)$. (Extensions for $t > 36$ are not included here.)

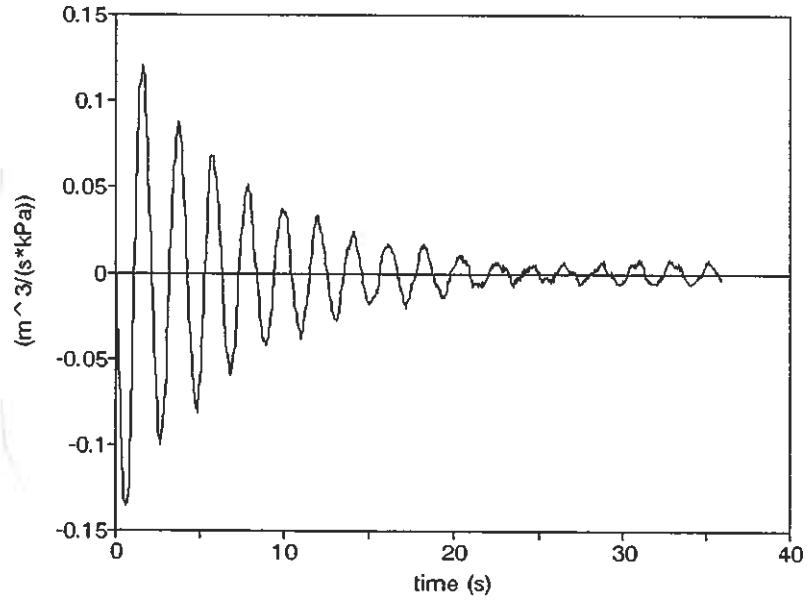

Figure 3.6: Step response for the single-chamber system, based on water level measurements in both chambers. Extension for $t > 36$ is not included here.

3.2.2 Hydrodynamical parameters

By performing FFT analysis of the time-domain results, the radiation admittance matrix $\mathbf{Y}(\omega)$ is easily derived (see equations (3.13 and 3.14)). The single-chamber radiation admittance $Y(\omega)$ is determined similarily. The excitation volume flux coefficient vector $\mathbf{q}_e(\omega)$ is derived from $Y(\omega)$ and $f_{e,I}(\omega)$ (see equation (3.23)), where $f_{e,I}(\omega)$ is the theoretically determined excitation force coefficient. The results are shown in figures 3.7 to 3.10. These have been corrected according to the assumed extensions of the time series for $t > 36$ s. From the figures we see that the main resonance frequency of the system is in the range of 3.00 - 3.15 rad/s, which corresponds to a wave period in the range of 2.00 - 2.10 s. Using the approximation $\omega_0 = \sqrt{g/l}$ where l is the effective length of each water column, a resonance frequency of $\omega_0 = 3.1$ rad/s corresponds to an effective length of 1 m, which is in good agreement with expectations.

There is also a significant peak in the spectra at about 8 rad/s. This is probably a result of interior resonances in the chambers, which is discussed more thoroughly in appendix B. We assume that these minor peaks in the hydrodynamical parameters tend to be somewhat over-estimated. This is discussed in section 3.3. One feature suggesting that the results may not be reliable for angular frequencies higher than about 4 rad/s, is that $G_d(\omega) = Re\{Y_d(\omega)\}$ turns out to be negative in the range of 4 - 8 rad/s, which cannot be correct. According to linear theory, the radiated power from one chamber when the other chamber is open, may be expressed

$$P_r = \frac{1}{2} G_d |\hat{p}_k|^2 \tag{3.28}$$

As this radiated power can never be negative, the diagonal radiation admittance G_d do also have to be non-negative for all frequencies. It is, however, difficult to determine the accuracy of each hydrodynamical parameter for frequencies in this range and above. These matters are more closely discussed in section 3.3.

The standard deviation of results from runs with equal experimental settings, are about 10 % for the peak values, and smaller for other frequencies.

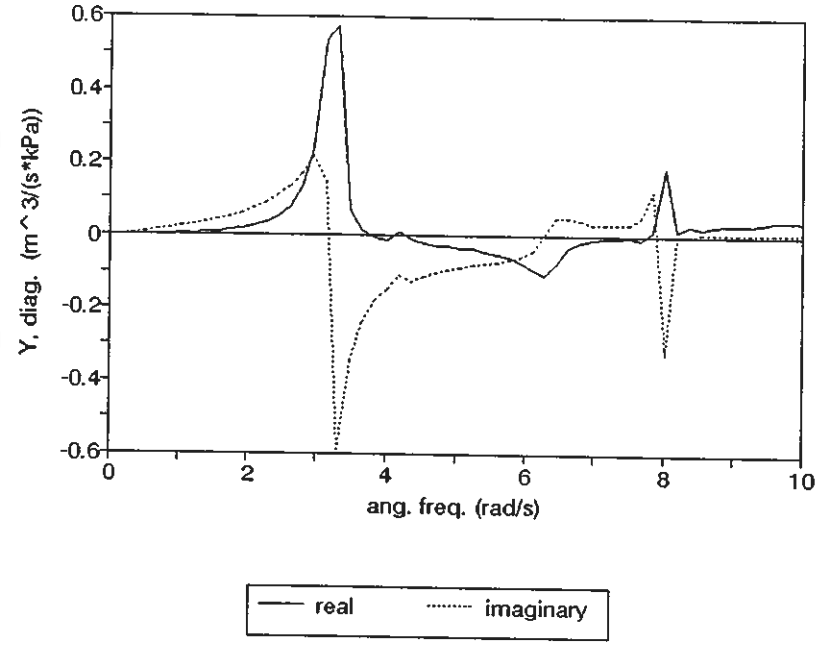

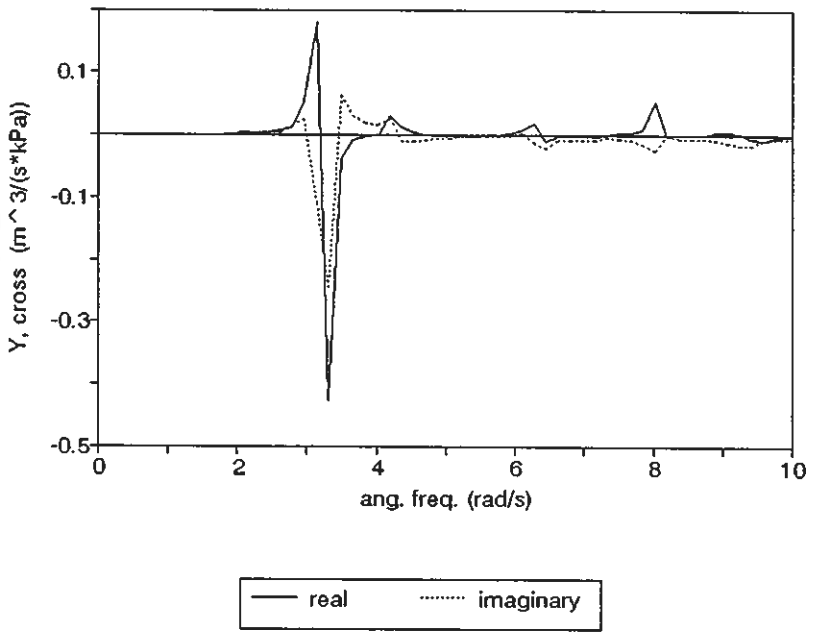

Figure 3.7: The real and imaginary parts of the radiation admittance matrix elements $Y_d(\omega)$ (a) and $Y_x(\omega)$ (b). Note that here (and in the following graphs of fig.3.8 to fig.3.20) the computed spectra are discrete, with a spacing between adjacent points of 0.175 rad/s. For visual convenience, straight lines are drawn between values. The Fourier transform of the time-series extensions are included when deriving the parameters.

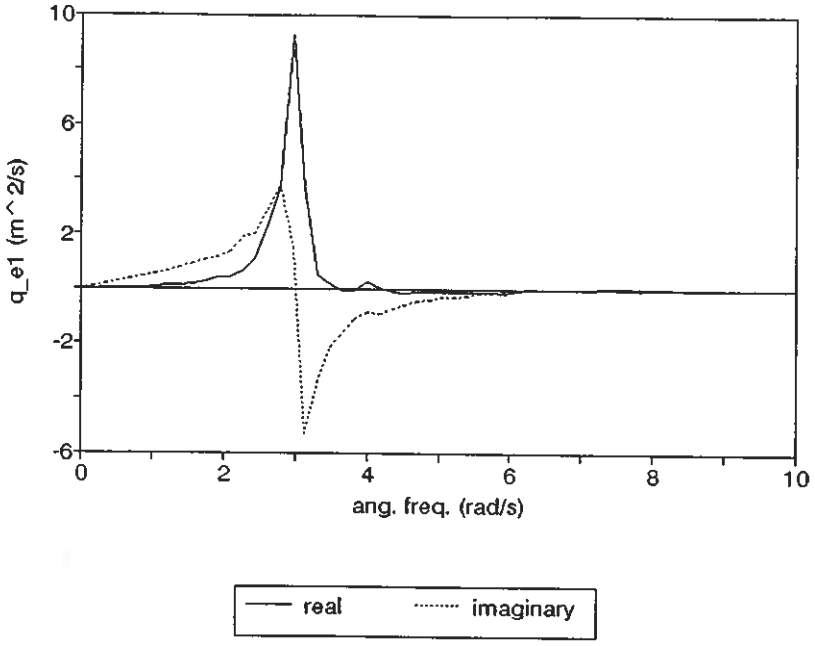

Figure 3.8: The real and imaginary parts of the excitation volum flux coefficient $q_{e,1}(\omega) = q_{e,2}(\omega)$ for the twin-chamber system.

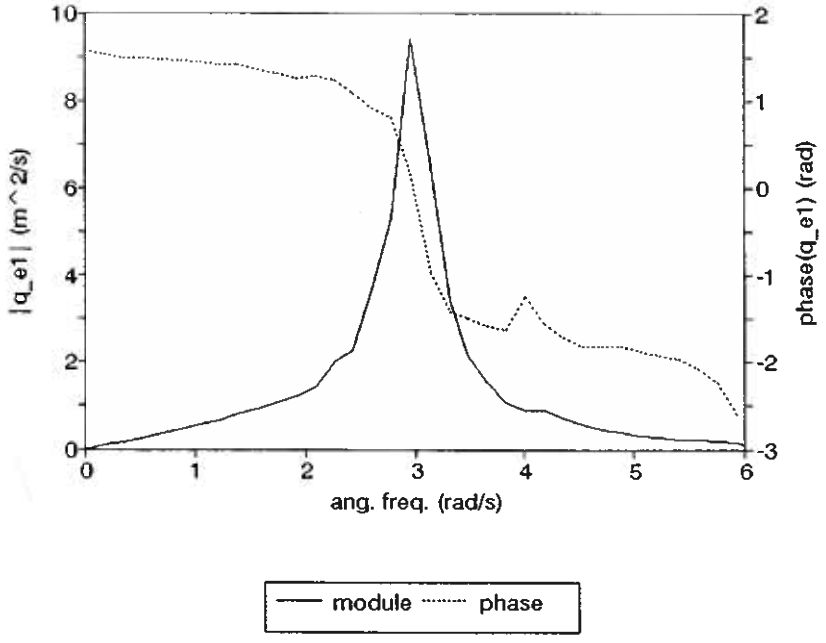

Figure 3.9: The module and phase of the excitation volum flux coefficient $q_{e,1}(\omega) = q_{e,2}(\omega)$ for the twin-chamber system.

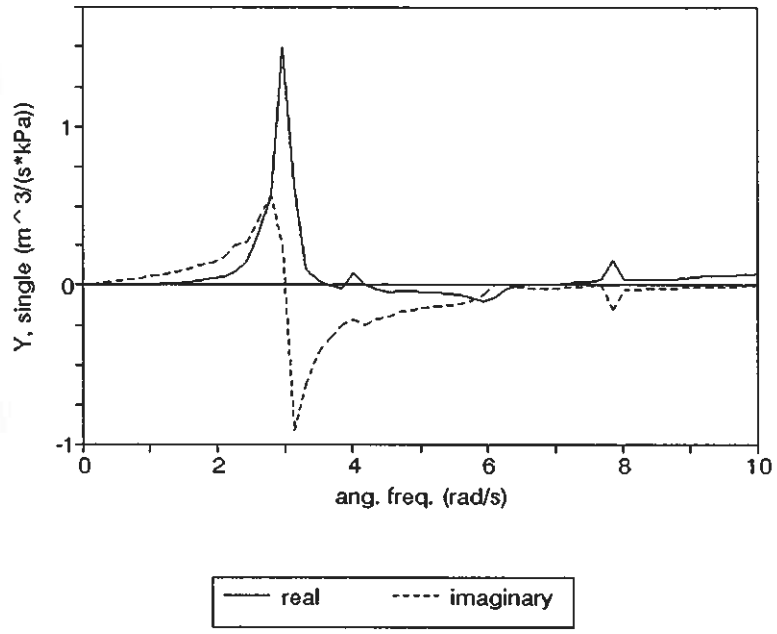

Figure 3.10: The real and imaginary parts of the radiation admittance $Y(\omega)$ for the single-chamber system. The Fourier transform of the assumed time-series extensions are included.

3.3 Discussion

The FFT algorithm always considers a periodic extension of the input signal, with a fundamental period equal to the registration time T_{reg} (36.0 seconds in our case). Hence, the frequency spectrum found by means of the FFT analysis will be discrete, and the spacing between any two adjacent points in the frequency domain is $\Delta\omega = 2\pi/T_{reg}$. In most of the frequency range, the obtained discrete spectra provide sufficient information. However, since the peaks of the spectra are rather sharp, the correct peak value may easily be under-estimated if the main resonance frequency has not been equal to an integer multiplied by the sampling frequency. To determine the continuous frequency spectrum of the measured time series, we carry out the following correction:

Considering the measured signals only, we know that these are time series which are zero for $t < 0$ and $t > T_{reg}$. Hence, the correct spectra are continuous, and not discrete. The continuous spectra may be obtained by calculating the convolution of the discrete FFT spectrum of each measured quantity, and the Fourier transform of a single square pulse [61,62]:

$$F(\omega) = \frac{1}{2\pi} F_p(\omega) * W(\omega) \tag{3.29}$$

where F_p is the discrete spectrum of the measured quantity (erroneously considered to be periodic by the FFT algorithm), and $W(\omega) = \mathcal{F}\{w(t)\}$, where

$$w(t) = \begin{cases} 0 & , t < 0 \\ 1 & , 0 < t < T_{reg} \\ 0 & , T_{reg} < t \end{cases} \tag{3.30}$$

Because F_p is non-vanishing only for discrete values of ω, the convolution integral becomes a sum, namely:

$$F(\omega) = \sum_{n=-\infty}^{\infty} F_p\left(\frac{2\pi n}{T_{reg}}\right) \frac{\sin \sigma_n}{\sigma_n} e^{-j\sigma_n} \tag{3.31}$$

where $\sigma_n = \omega T_{reg}/2 - n\pi$. As seen from equation (3.31), the index n should run from $-\infty$ to $+\infty$. In practice, however, the series has to consist of a finit number of terms. Hence, we include only the terms for which F_p is assumed to be non-negligible. However, this is not easy to determine with certainty. According to theory, both the real and the imaginary part of F_p are assumed to approach zero for high frequencies. The spectrum of the measured time series is however rather irregular for higher frequencies, and it is not obvious for how high frequencies it is reasonable to include terms into the series.

Although the above correction provides a continuous function, we will in practice only be able to present the results as a discrete set of data, in a spreadsheet or a data file. We may however choose the spacing between adjacent frequency values as short as we wish. Since we only want to use the correction as a check of the obtained peak value, we assume that it is sufficient to consider a set of discrete frequencies which is five times denser than the original spectrum. Such a check is presented for the real part of the diagonal radiation admittance Y_d, in figure 3.11. It turns out that the correction of the peak value due to this resampling is smaller than the correction following from the assumed extension of the time series.

As mentioned in section 3.1.1, we have to correct the measured time-series for $t < 0$. In chamber no. 2 both the air pressure and the excursion should have a constant non-zero value for $t < 0$, that is, before data logging is started. This means that a term involving a step function should be added to the corresponding time series. For the excursion in chamber 2, the added term is (see also eq. (3.11)):

$$s_{2\_}(t) = \begin{cases} s_0 & , t < 0 \\ s_0/2 & , t = 0 \\ 0 & , t > 0 \end{cases} \tag{3.32}$$

The Fourier transform of $s_{2\_}(t)$ becomes [63]:

$$\tilde{s}_{2\_}(\omega) = s_0(\pi\delta(\omega) + j/\omega) \tag{3.33}$$

A similar correction applies for the air pressure in the same chamber (no. 2). As we consider nonzero frequencies only, the Dirac-delta functions are of no concern.

We also have to investigate what happens when $t > T_{reg}$. As mentioned in section 3.2.1, we have made extensions of the time series from $t = T_{reg}$ to infinity. These extensions are simply damped sinusoidal functions, where the frequencies and damping coefficients are chosen to match the measured data prior to the end of the registration period. It may be noted that such an extension is not in accordance with the asymptotic behaviour of free oscillation of a heaving body, as studied by Ursell [64]. It is believed, however, that the difference is too small to have any significance in our case. We see from the figures 3.12 and 3.13 that the extensions leads to a correction of the peak values, and no significant changes otherwise. It should be noted, however, that the frequency of the extension terms is assumed to coincide with the peak frequency of the measured spectrum. If this assumption is not correct, the correction due to the extension should not lead to a significant change in the original peak, but rather a small shift in the peak frequency.

Another question which should be considered, is how high in the frequency range the hydrodynamic parameters are valid. One such upper limit may be found by stating that the hydrodynamic parameters of model I will not be meaningful for wavelengths shorter than the smallest horizontal dimension of the OWC model. This gives a maximum valid angular frequency of $\omega_{max} \sim 11$ rad/s. Other considerations may, however, imply that the parameters are inaccurate for even lower angular frequencies. One feature suggesting this, is the several minor peaks present in the frequency-domain results (see e.g. figure 3.7). These resonances are associated with internal oscillation modes (see appendix B). Hence, the interior water surfaces do not oscillate as horizontal, rigid pistons. This means that model I will not be valid at these frequencies. As for model II, the radiation admittance will usually be over-estimated at these internal resonance frequencies. This is because the radiation admittance is a function of the volume flux, and this flux is calculated from the measured chamber excursion. Since the surface do not act as a rigid piston at the frequencies of these interior oscillations, the real volume flux caused by the oscillations will be smaller than the value derived from elevation measurements, if the water-level gauge does not happen to be in a node of the interior standing wave. Hence, the hydrodynamic parameters may be incorrect at these interior resonance frequencies.

The obviously incorrect negative values of Y_d in the range of 4 - 8 rad/s (see section 3.2.2) suggest that the other hydrodynamical parameters also may be unreliable in this frequency range. The negative values may however be a result of the interior sloshing in chamber no. 2 (see figure 3.5), which has been a significant problem only for the diagonal element of $\mathbf{Y}$.

Waves with wavelengths greater than twice the flume width, will generate no cross waves in the flume. However, the pressure step function in this experiment does in principle generate waves of all frequencies. Some of these wave components may have given rise to cross waves in the flume. As shown in table B.1 in appendix B, wave periods shorter than 2.44 s can lead to cross waves. This corresponds to angular frequencies greater than 2.58 rad/s. In fact, the resonance frequency of the system ($\omega_0 \approx 2.1$ rad/s) lays between the first two cross-wave modes ($\omega_1 = 2.58$ rad/s and $\omega_2 = 4.00$ rad/s). This might be the main reason that the measurements of the radiated waves have been hampered with large unaccuracy. In this work, however, we have used only the excursion of the interior water surfaces as input to our derivation of the hydrodynamical parameters. We assume that possible feedback of cross waves to the oscillations in the chambers, have been of small importance.

If we neglect possible influence from cross waves, it should in principle be possible to absorb all incident wave energy by means of a single water column, provided that the oscillation of the column is optimally controlled. This means that the matrix $\mathbf{G}$, which consists of the real parts of the elements of $\mathbf{Y}$, should be singular for $\omega < 2.58$ rad/s. (Using the rigid-piston description (model I), the corresponding radiation resistance matrix must be singular in the same frequency interval [65].) In our case, where $G_{11} = G_{22}$, this means that G_{11}, G_{22}, G_{12} and G_{21} should all be equal for $\omega < 2.58$ rad/s. This is not the case for our experimental results, but the deviation from equality is within limits of uncertainty.

By dividing the water surface excursion in each chamber by the corresponding surface level at $t = 0$, we get non-dimensionalised functions. If the system is linear, such functions obtained from runs with different initial levels should be equal. However, comparison of the different runs shows that the non-dimensionalised functions do to some extent depend on the initial levels, and hence, on the initial applied pressure. This dependency shows how nonlinear loss effects come into play (see figure 3.14).

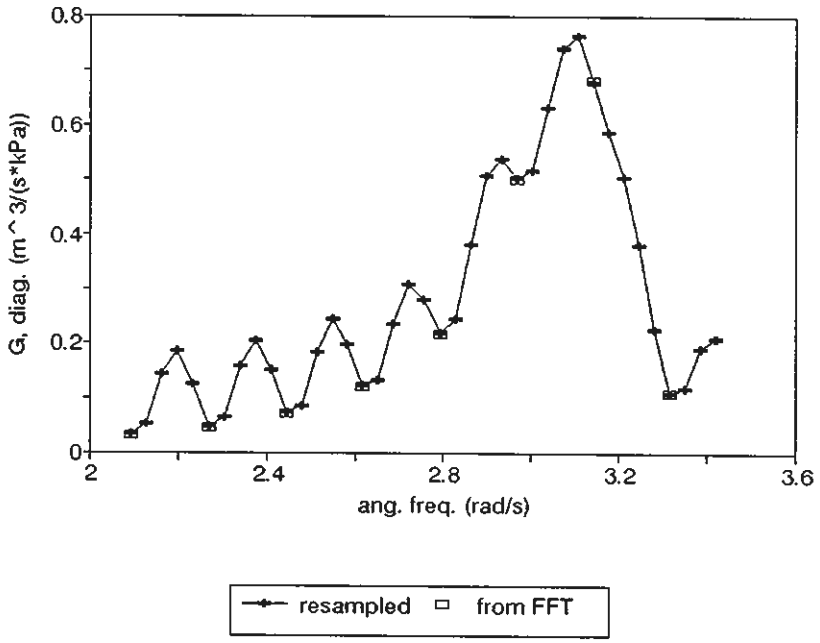

Figure 3.11: The real part of the radiation admittance $Y_d(\omega)$. Corrected spectrum including intermediate points for frequencies in the vicinity of the main peak. The points marked as small rectangels represent the same values as given by the dotted curve shown in figure 3.12.a.

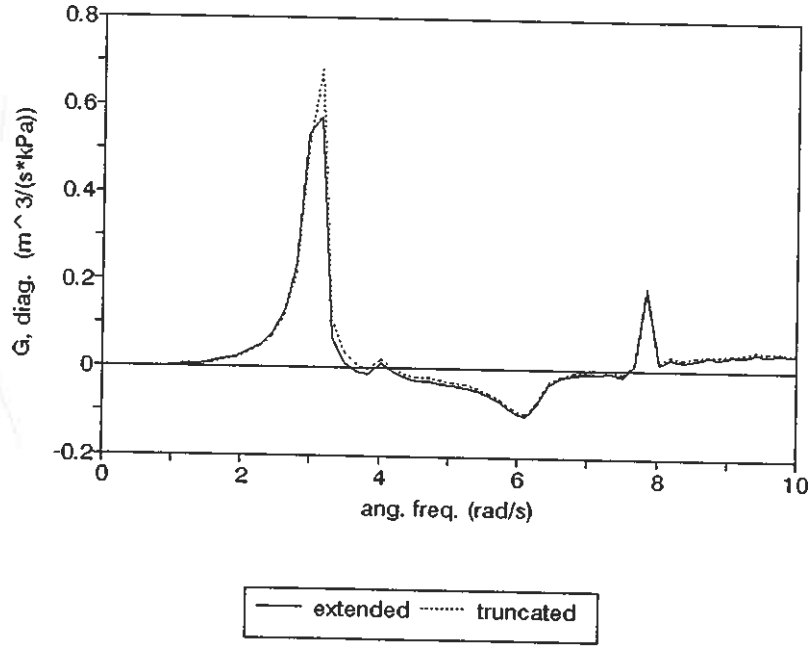

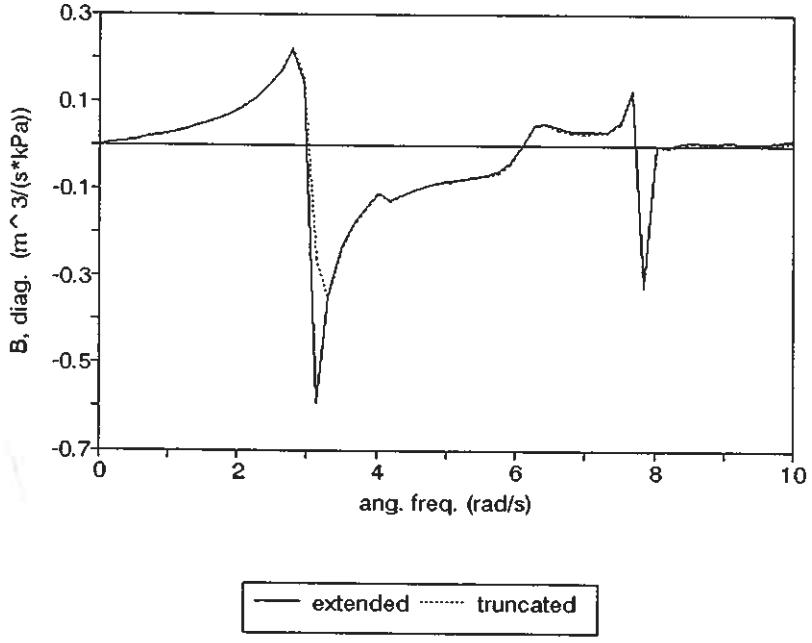

Figure 3.12: The diagonal element $Y_d(\omega)$ of the radiation admittance matrix, drawn with and without corrections due to assumed extensions: a) real part, b) imaginary part.

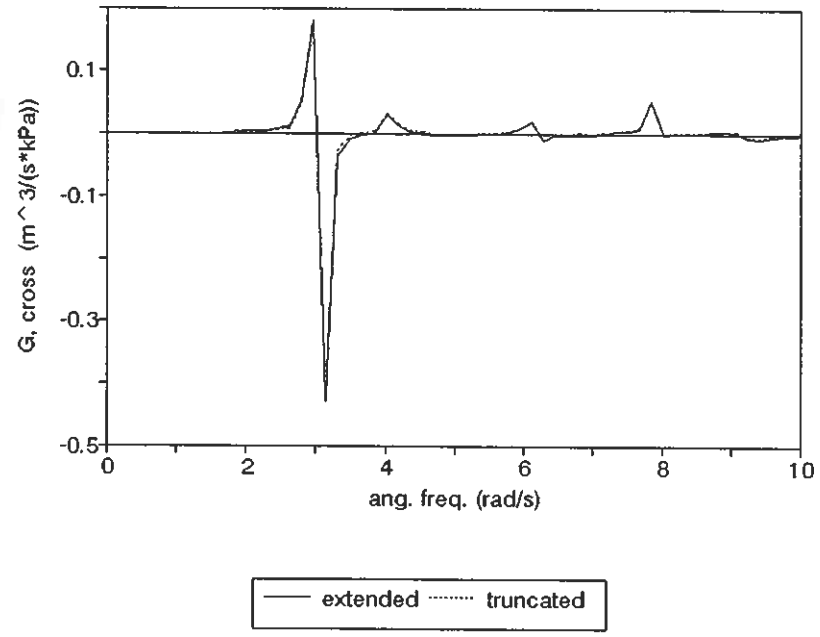

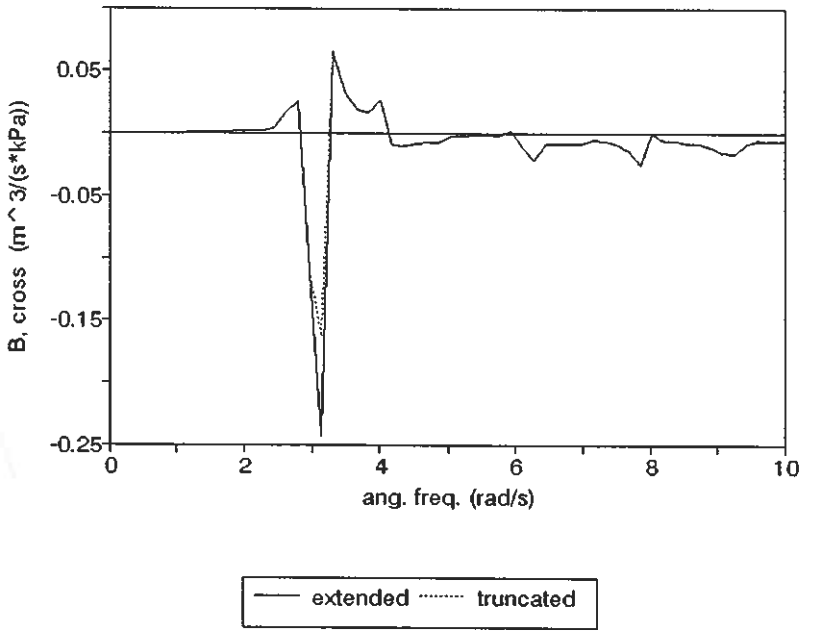

Figure 3.13: The off-diagonal element $Y_x(\omega)$ of the radiation admittance matrix, drawn with and without corrections due to assumed extensions: a) real part, b) imaginary part.

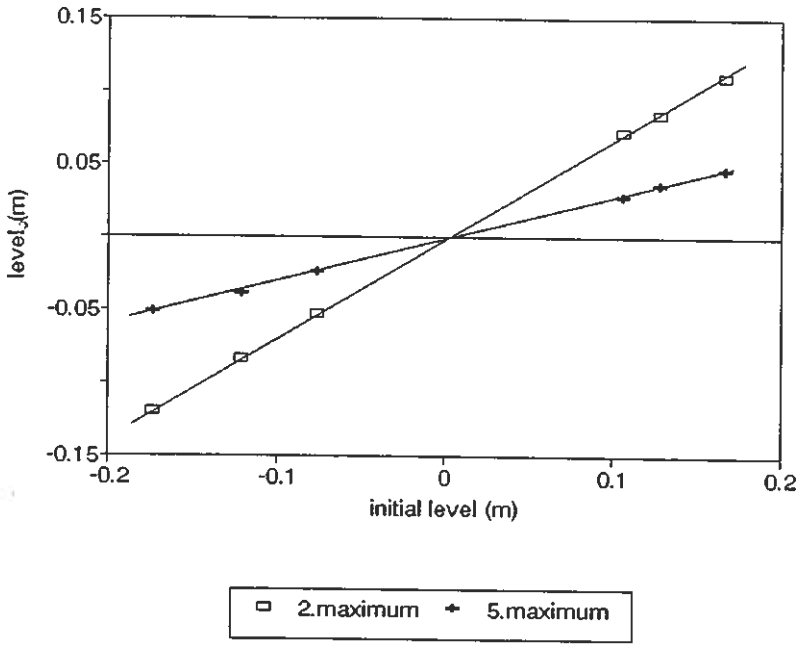

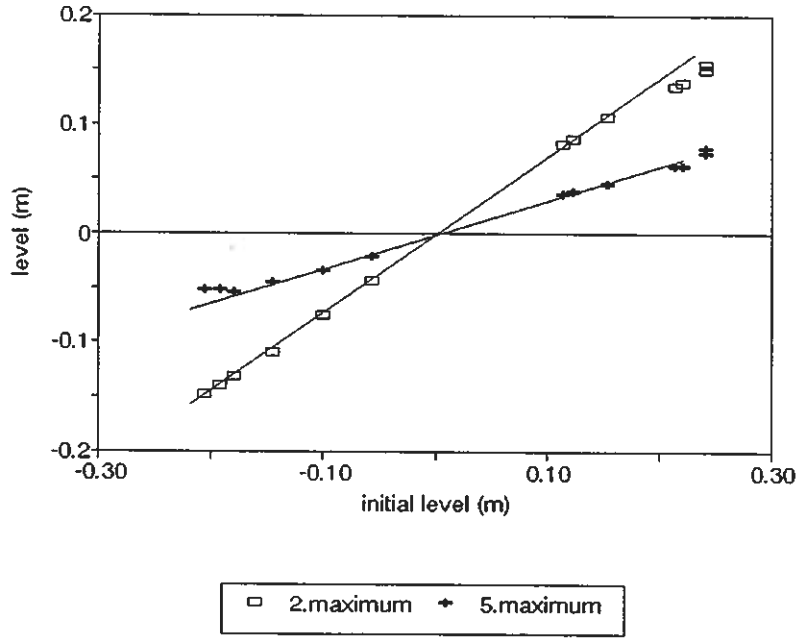

Figure 3.14: Water level at the 2nd and 5th maximum of the oscillation as a function of the initial level: a) single OWC, b) twin OWC, chamber no. 2. Deviation from a straight line is due to non-linearity.

Chapter 4

Small-scale two-dimensional experiments for determining loss parameters for a single OWC

When investigating wave energy converters of the OWC type, it is of interest to quantify the energy loss in the water, that is, loss due to viscous friction and vortex shedding. The amount of losses due to vortex shedding will depend on the so-called Keulinger-Carpenter number, which is proportional to the ratio of the water oscillation amplitude to the radius of curvature at the edges of the structure. In the present work we have attempted to minimise the nonlinear loss by using relatively small incident waves.

In a previous work [66] the radiation resistance and loss resistance for a phase-controlled buoy system have been determined experimentally for one wave frequency. In the present work we use a similar method to determine these quantities for a small-scale model of a single two-dimensional OWC in a fixed structure. However, we use no phase control, the air chamber is open, and we investigate the system at several wave frequencies.

Another part of this work considers a transient wave radiated from the OWC model. The transient wave is made by applying a stationary pressure in the air chamber, and then suddenly open the chamber towards the atmosphere. The method is similar to the one described in chapter 3. Relatively large experimental uncertainty has made it difficult to retrieve useful information from measurements of the transient radiated wave. However, by using a relation depending on the chamber oscillation only, we have succeeded in determining a value for the loss resistance in good agreement with the result from the experiment with incident wave.

4.1 Theory

In this chapter we consider a single two-dimensional OWC model in scale 1:30, placed in a narrow wave channel. The origin is chosen to be at the front wall of the model, and positive x direction is defined to be in the direction of an incident wave.

The linear loss mechanisms in our system are most easily described in terms of a loss resistance. Hence, we choose to describe the the system in terms of the rigid piston model

(model I) throughout this chapter. Another convenient advantage by using model I, is that the diffracted wave is known, at least approximately. With model I, the interior water surface is assumed to be held fixed for the diffraction problem. Since the OWC is not moving, we may assume, at least as an approximation, that the water in the OWC mouth at $x = 0$, has a zero horizontal velocity component. Then the diffracted wave is equal to the wave reflected from a fixed vertical wall at $x = 0$. We observe that there is no evanescent (near-field) contribution to this diffracted wave.

4.1.1 Diffracted and radiated wave

We consider a regular incident wave $\eta_i(x,t) = Re\{\hat{A}e^{j(\omega t - kx)}\}$. Here, $\hat{A}$ denotes the complex amplitude of the wave at $x = 0$, ω is the angular frequency, and k is the angular repetency. In a similar way we define the wave reflected from the model:

$$\eta_s(x,t) = (\hat{\eta}_d(0,\omega) + \hat{\eta}_{r,I}(0,\omega))\, e^{j(\omega t + kx)} + \eta_{nf}(x,t) \tag{4.1}$$

Here, $\hat{\eta}_d(0,\omega)$ is the complex amplitude of the diffracted wave at $x = 0$, that is, the wave which would be reflected if the OWC was held fixed. Correspondingly, $\hat{\eta}_{r,I}(0,\omega)$ is the complex amplitude of the far-field part of the radiated wave, which is the contribution caused by the oscillatory motion of the OWC. Finally, $\eta_{nf}(x,t)$ is the near-field part of the radiated wave, which is negligible at the position of the wave gauges.

The complex amplitudes may be written as follows:

$$\hat{\eta}_i(0,\omega) = |\hat{A}|e^{j\phi_i} \tag{4.2}$$

$$\hat{\eta}_s(0,\omega) = |\hat{\eta}_s|e^{j\phi_s} \tag{4.3}$$

$$\hat{\eta}_d(0,\omega) = |\hat{\eta}_d|e^{j\phi_i} \tag{4.4}$$

$$\hat{\eta}_{r,I}(0,\omega) = |\hat{\eta}_{r,I}|e^{j\phi_s} \tag{4.5}$$

where the ϕ-s are termed *phase constants*. In our system we choose the origin ($x = 0$) to be at the front wall of the OWC. Unless stated otherwise, all waves are refered to the origin. Further, we choose $\phi_i \equiv 0$ at the origin. Hence, all other phases will be relative to ϕ_i. We also introduce a complex *diffraction factor*:

$$\Gamma_d \equiv |\Gamma_d|e^{j\alpha} = \frac{\hat{\eta}_d}{\hat{A}} \tag{4.6}$$

Hence, $|\Gamma_d| = |\hat{\eta}_d|/|\hat{A}|$ and $\alpha = \phi_d - \phi_i$.

When the OWC is held fixed, there is no radiated wave in the flume, that is, $\eta_{r,I}(x,t) + \eta_{nf}(x,t) = 0$. Then we have $\hat{\eta}_d = \hat{\eta}_s$, by equation (4.1). We also have assumed that a fixed two-dimensional OWC in a plane wall will act as a totally reflecting wall, that is, $|\hat{\eta}_s| = |\hat{A}|$. This results in $|\Gamma_d| = 1$. For this case of total reflection the endwall must be at an anti-node. In other words, the incident wave and the reflected wave must be in phase at the origin, that is, $-kx + \phi_i = kx + \phi_d$ for $x = 0$. Having already chosen $\phi_i \equiv 0$, we obtain that $\phi_d = 0$, and hence, $\alpha \equiv \phi_d - \phi_i = 0$.

4.1.2 Open chamber. Power loss and loss resistance

Inserting the diffraction factor Γ_d into equation 4.1, and using $\phi_i = 0$ for $x = 0$, we obtain

$$\hat{\eta}_{r,I}(0,\omega) = \hat{\eta}_s(0,\omega) - \Gamma_d \hat{A} = |\hat{\eta}_s| e^{j\phi_s} - |\hat{A}| \tag{4.7}$$

Hence, the radiated wave may easily be derived from the measured quantities $\hat{\eta}_s$ and $\hat{A}$. Note that in order to avoid near-field contributions from the radiated wave, $\hat{\eta}_s(x,\omega)$ has to be measured some distance $|x|$ from the OWC, and a corresponding correction of the phase has to be made, to find $\hat{\eta}_s(0,\omega)$.

Since there is no power take-off in the open chamber, we may find the power loss in the system directly, by calculating the difference between the incident wave power and the wave power returned "upstream" from the OWC:

$$P_f = P_i - P_s = J_i d - J_s d = \frac{\rho g^2 D d}{4\omega}(|\hat{A}|^2 - |\hat{\eta}_s|^2) \tag{4.8}$$

Here, P_f, P_i and P_s denotes the lost power, the incident wave power and the reflected wave power (including radiated power), respectivily. Further, $D(kh) = \tanh kh + kh/(\cosh^2 kh)$ is the depth function (2.3), d is the width of the flume, ρ is the mass density of water, and g is the acceleration of gravity. Further, J_i is the power transport (power per unit width of the wave front) associated with the incident wave (2.4), and J_s is the power transport associated with the wave returned upstream from the OWC.

The power associated with radiation from the OWC may be expressed as

$$P_{r,I} = \frac{1}{2} R_{r,I} |\hat{u}|^2 = \frac{1}{2} R_{r,I} \omega^2 |\hat{s}|^2 \tag{4.9}$$

Here, $\hat{u}$ is the complex amplitude of the oscillation velocity of the interior water surface, and $\hat{s}$ is the corresponding complex amplitude of the water surface excursion. Further, $R_{r,I}$ is the radiation resistance (2.9). The radiated power may alternatively be written as

$$P_{r,I} = J_{r,I} d = \frac{\rho g^2 D d}{4\omega} |\hat{\eta}_{r,I}|^2 \tag{4.10}$$

Here, $J_{r,I}$ denotes the power transport associated with the radiated wave. Equating (4.9) and (4.10), we obtain

$$R_{r,I} = \frac{\rho g^2 D d}{2\omega^3} \frac{|\hat{\eta}_{r,I}|^2}{|\hat{s}|^2} \tag{4.11}$$

Further, the following expression results from a well known reciprocity relation [67,68] between the radiation resistance and the amplitude of the excitation force:

$$R_{r,I} = \frac{|\hat{F}_{e,I}|^2}{8 d J_i} = \frac{\omega |f_{e,I}|^2}{2\rho g^2 D d} \tag{4.12}$$

In this expression $\hat{F}_{e,I} = \hat{A} f_{e,I}$ is the excitation force, which is the force from the incident wave on the OWC, if it is held fixed. Now, combining (4.11) and (4.12), we get

$$|\hat{s}| = \frac{|\hat{f}_{e,I}|}{\omega R_{r,I}} |\hat{\eta}_{r,I}| \tag{4.13}$$

Hence, assuming that linear theory is applicable, this expression gives the linear relationship between the radiated wave and the interior water surface excursion. If the incident wave is large, we should expect experimental deviation from the linear relation of equation (4.13).

Assuming that power is extracted by means of some power take-off device, the useful power can be written as

$$P_u = P_{e,I} - P_{r,I} - P_f = \frac{1}{2}|\hat{F}_{e,I}||\hat{u}|\cos\gamma - \frac{1}{2}(R_{r,I} + R_f)|\hat{u}|^2 \tag{4.14}$$

where $P_{e,I}$ is the *excitation power* in terms of the rigid-piston description. Further, R_f is the *loss resistance*, that is, the resistance associated with the frictional losses in the system. We assume a linear relationship between the friction force and the velocity. Hence, R_f is independent of the amplitude. The angle γ is the phase difference between the excitation force and the oscillation velocity of the OWC. For our OWC in a reflecting wall, the excitation force coefficient $f_{e,I} = \hat{F}_{e,I}/\hat{A}$ is a real function of ω . Hence, γ equals the phase difference between the incident wave and the oscillation velocity of the OWC. In our case, no power take-off is applied, and the useful power P_u is zero. Hence, we obtain from eq. (4.14):

$$|\hat{s}| = \frac{|\hat{f}_{e,I}|\cos\gamma}{\omega(R_{r,I} + R_f)}|\hat{A}| \tag{4.15}$$

where we have used that $\hat{u} = j\omega\hat{s}$ and $\hat{F}_{e,I} = \hat{f}_{e,I}\hat{A}$. This equation expresses a linear relationship between the incident wave and the water surface excursion in the chamber.

By measuring the incident wave and the excursion in the chamber, and calculating the far-field radiated wave as shown in equation (4.7), we may express the excursion amplitude as a function of the radiated wave (4.13), and as a function of the incident wave (4.15). Hence, by deriving the slope of the graphs obtained from these linearity tests, we may find $|\hat{s}|/|\hat{\eta}_{r,I}|$, $|\hat{s}|/|\hat{A}|$ and $|\hat{\eta}_{r,I}|/|\hat{A}|$. An experimental value for the radiation resistance $R_{r,I}$ can then be obtained from equation (4.11).

Further, combining the equations (4.13) and (4.15), we find the loss resistance:

$$R_f = R_{r,I}\left(\frac{|\hat{\eta}_{r,I}|}{|\hat{A}|}\cos\gamma - 1\right) \tag{4.16}$$

4.1.3 Transient radiated waves

In this section we introduce a method which, in principle, allows us to determine the radiation impedance $Z_{r,I}$, as well as the loss resistance R_f, by means of a transient experiment.

According to theory, time series obtained from a transient experiment, should through Fourier analysis, give information of the parameters of the system for all frequencies. (Note however that the rigid-piston description is not applicable at high frequencies.) Using the rigid-piston descripton of the OWC, we introduce:

$$Z_w = Z_{r,I} + R_f \tag{4.17}$$

where $Z_{r,I}$ is the radiation impedance and R_f is the loss resistance. Hence, the friction may be included in the model description by modifying equation (2.5) as follows:

$$\tilde{F} = \tilde{F}_{e,I} - Z_w \tilde{u} \tag{4.18}$$

where the tilde denotes the Fourier transform of a general time function (not necessarily periodic), and F is the total force acting on the interior water surface. Since the water buoyancy contributes to the total force, we may write

$$\tilde{F} = S_k(\tilde{p} + \rho g \tilde{s}) \tag{4.19}$$

Remembering that the hydrodynamic added mass is included in $Z_{r,I}$, and hence in Z_w, a combination of equations (4.18) and (4.19) is just the equation of motion for the massless rigid piston of our assumed model I.

In a transient experiment there is no incident wave, and consequently, the excitation force $F_{e,I}$ is zero. Then, measuring the dynamic chamber pressure p and the water surface excursion s, and using the relation $\tilde{u} = j\omega\tilde{s}$, we may calculate Z_w as a function of ω.

The interior water surface excursion may be expressed as follows:

$$s(t) = s_-(t) + s_+(t) \tag{4.20}$$

where

$$s_-(t) = \left\{ \begin{array}{ll} s_0 & , t < 0 \\ s_0/2 & , t = 0 \\ 0 & , t > 0 \end{array} \right\} = s_0(1 - H(t)) = s_0 H(-t) \tag{4.21}$$

and

$$s_+(t) = \left\{ \begin{array}{ll} 0 & , t < 0 \\ s_0/2 & , t = 0 \\ s(t) & , t > 0 \end{array} \right. \tag{4.22}$$

Here, s_0 is the stationary chamber level before the valve is opened. Further, $H(t)$ is the Heaviside step-function. The vertical velocity of the interior water surface is defined as $u(t) = ds(t)/dt$. It should be noted that as a result of this definition, $s(t)$ and $u(t)$ are continuous functions, while $s_+(t)$ and $u_+(t) = ds_+(t)/dt$ are discontinuous.

The dynamic chamber pressure may be be expressed similarily

$$p(t) = \left\{ \begin{array}{ll} p_0 & , t < 0 \\ p_0/2 & , t = 0 \\ 0 & , t > 0 \end{array} \right\} = p_0(1 - H(t)) = p_0 H(-t) \tag{4.23}$$

where p_0 is the stationary chamber pressure before the valve is opened.

When performing the Fourier analysis, we use an FFT algorithm to find the transform $\tilde{s}_+(\omega) = \mathcal{F}\{s_+(t)\}$. The transform $\tilde{s}_-(\omega) = \mathcal{F}\{s_-(t)\}$, however, may be found theoretically from equation 4.21. Hence, we get [63]:

$$\tilde{s}_- = s_0(\pi\delta(\omega) + j/\omega) \tag{4.24}$$

The transform of the oscillation velocity becomes $\tilde{u} = \tilde{u}_- + \tilde{u}_+ = j\omega(\tilde{s}_+ + \tilde{s}_+)$, by definition. Considering $\omega > 0$ only, we may ignore the Dirac delta-function in eq. (4.24). The pressure is treated similarily.

Combining the above equations (4.18) to (4.24), we derive

$$Z_w(\omega) = \frac{-\rho g S_k}{j\omega - s_0/\tilde{s}_+(\omega)} \quad \text{where} \quad \omega \neq 0 \tag{4.25}$$

We now consider the power associated with an outgoing wave from the OWC model. We assume that there is no incident wave. First, we restrict the problem to the case of a regular outgoing wave. Combining eqs. (4.9) and (4.10), we find

$$\frac{1}{2} R_{r,I} |\hat{u}|^2 = J_{r,I} d = \frac{\rho g^2 D(kh) d}{4\omega} |\hat{\eta}_{r,I}|^2 \tag{4.26}$$

When the wave is irregular, we have to replace the complex amplitudes of the regular quantities with the Fourier transforms of the corresponding irregular quantities. Hence, we obtain

$$R_{r,I}(\omega) = \frac{\rho g^2 D(kh) d}{2\omega} \frac{|\tilde{\eta}_{r,I}(\omega)|^2}{|\tilde{u}(\omega)|^2} \tag{4.27}$$

From eq. (4.17) we get

$$R_f = Re\{Z_w(\omega)\} - R_{r,I}(\omega) \tag{4.28}$$

Hence, inserting eqs. (4.25) and (4.27) into (4.28) gives the loss resistance R_f. Note that R_f should be independent of ω (see section 4.3). Having derived Z_w found in equation (4.25), we may also calculate the hydrodynamic added mass of the system (cf. (2.6) and (4.17)):

$$m_{r,I} = \frac{Im\{Z_w\}}{\omega} \tag{4.29}$$

Considering the interior water surface as a massless rigid piston, all of the inertia in our oscillating system is included in this quantity. (We neglect the inertia of the oscillating air.)

Now, we introduce an alternative method for determining the loss resistance R_f, by considering the equation of motion in the time domain:

$$m_{r,I}(\infty) \frac{d^2 s_+}{dt^2}(t) + k_r(t) * \frac{ds_+}{dt}(t) + R_f \frac{ds_+}{dt}(t) + \rho g S_k s_+(t) = 0 \tag{4.30}$$

where $k_r(t) = \mathcal{F}^{-1}\{Z_{r,I}(\omega) - j\omega m_{r,I}(\infty)\}$. Integrating (4.30) from zero to infinity, we first consider the convolution term. The radiation force, and hence, k_r, have to be a causal function. Due to this fact, we have that [69]:

$$k_r(t) = 2\mathcal{F}^{-1}\{R_{r,I}(\omega)\} \quad \text{when} \quad t \geq 0 \tag{4.31}$$

Note that this expression is not valid for negative t. From eq. (4.31) we obtain

$$R_{r,I}(\omega) = \frac{1}{2} \int_0^\infty k_r(t) e^{j\omega t} dt \tag{4.32}$$

Further, knowing that $R_{r,I}(0) = 0$, we find from (4.32):

$$\int_0^\infty k_r(t) dt = 0 \tag{4.33}$$

The integral of the convolution term then becomes

$$\begin{aligned}\int_0^\infty k_r(t) * \frac{ds_+}{dt}(t)dt &= \int_0^\infty \int_0^t k_r(t-\tau)u_+(\tau)d\tau dt \\ &= \int_0^t u_+(\tau)\left(\int_0^\infty k_r(t-\tau)dt\right)d\tau \end{aligned} \tag{4.34}$$

The inner integral in the last expression in (4.34) may be written

$$\int_0^\infty k_r(t-\tau)dt = \int_{-\tau}^\infty k_r(t')dt' = \int_{-\tau}^0 k_r(t')dt' + \int_0^\infty k_r(t')dt' \tag{4.35}$$

The first term in (4.35) is zero due to causality. The second term is also zero, from (4.33). Hence, it follows that the integral in equation (4.34) also have to be zero:

$$\int_0^\infty (k_r(t) * \frac{ds_+}{dt}(t))dt = 0 \tag{4.36}$$

Inserting this result into equation (4.30), we get

$$R_f s_+(0^+) = \rho g S_k \int_0^\infty s_+(t)dt - m_{r,I}(\infty)\frac{ds_+}{dt}(0^+) \tag{4.37}$$

Using that $s_+(0^+) = -p_0/\rho g$ and $ds_+(0^+)/dt = 0$, we finally obtain

$$R_f = -\frac{\rho^2 g^2 S_k}{p_0}\int_0^\infty s_+(t)dt \tag{4.38}$$

It should be noted that the only input to this relation, is the excursion of the interior water surface.

4.2 Experiments and results

The aim of these experiments has been to quantify the power losses related to the linear performance of a single two-dimensional OWC, and to find the mechanical resistance associated with these losses.

4.2.1 Setup and measurements

The experiments have been performed in a 0.33 m wide and 12 m long wave flume, which is equipped with a wavemaker in one end and an absorbing beach in the other (see figure 4.1). Due to a feedback system, the wavemaker is able to account for reflections at the wavemaker paddle, and hence, maintain the desired incident wave with constant frequency and amplitude. The OWC model has the same width as the flume, which means that the experiment is two-dimensional (2D). The horizontal extension of the model in the direction of wave propagation is 0.32 m. The barrier draft is 0.20 m. At the lower end the barrier has a radius of curvature equal to 0.05 m, and the barrier thickness is 0.10 m. The natural frequency of the OWC model is 0.67 Hz (determined experimentally as

the frequency for which the ratio of the amplitude of the excursion in the open chamber, to the amplitude of the incident wave has its maximum).

In the first part of the experiment, a regular incident wave is sent towards the 2D single-chamber OWC, where the air chamber is open to the atmosphere. The frequency and the amplitude of the incident wave are varied from run to run. The measurements include the water surface excursion inside the chamber as well as the wave elevation at three different positions in the flume outside the OWC. The three two-wire gauges used to measure the wave elevation are placed in a row along the longitudinal direction of the flume. This arrangement makes it possible to obtain experimental values for the incident and reflected waves, as well as for an estimate of the measurement uncertainty. The time of registration for each run has been $T_{reg} = 51.2$ s. The experimental setup is shown in figure 4.1.

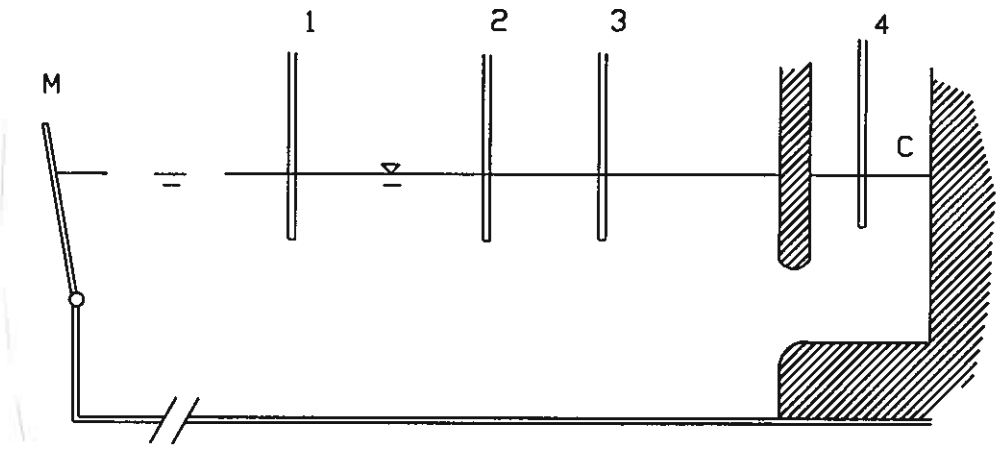

Figure 4.1: Setup for small-scale 2D experiments on an OWC with open air chamber. Four two-wire gauges are used to measure water surface elevations. M: wave maker, 1-4: water elevation gauges, C: air chamber. The gauges 1-3 are placed 3.3 m, 2.7 m and 1.5 m from the OWC model, respectivily.

In the second part of these experiments a transient radiated wave *from* the OWC model is considered, made by means of a pressure step inside the chamber. No incident wave is present in this case. The model is in this case sited in the opposite end of the flume and turned in the opposite direction. Hence, the radiated waves are attenuated by means of the absorbing beach, and not by means of the wavemaker paddle, as in the case of the incident wave experiment. The pressure step is achieved by establishing a stationary pressure in the closed chamber, and then suddenly open an air valve, shortly after starting the data aquisition. The initial stationary chamber pressure is varied from run to run, and both negative and positive pressures are applied. The method and setup of this part of the experiment is similar to the work described in chapter 3. It has turned out, however, that the measurement of the radiated wave is too inaccurate to provide reliable experimental information by using the equations (4.25), (4.27), (4.28) and (4.29). Still, an estimate of the loss resistance is derived from measurements of the water surface excursion in the chamber only, using the relation (4.38).

4.2.2 Incident wave experiment

The power loss is derived using the wave power relation (4.8). Figure 4.2 shows the amount of power loss (in percent) as a function of the incident wave for different frequencies. As shown in this figure, between 10 and 25 % of the incident wave power is lost for all frequencies except 0.4 Hz, depending on the wave frequency and the amplitude of the incident wave. For the frequency $f = 0.4$ Hz, the loss is between 5 and 30 %.

The water excursion in the chamber is plotted as a function of the incident wave and the radiated wave, respectively, in figure 4.3. The experimental points seem to fit a straight line through the origin, except for a few points corresponding to large amplitudes. This gives support to our assumption that the loss resistance is independent of the wave amplitude (for sufficiently small amplitudes). The radiation resistance, and hence, also the loss resistance, has been calculated from the slopes of the graphs, as explained in section 4.1.2. The slopes have been calculated by means of linear regression of all the measured data. However, the decision of how large wave amplitudes that should be investigated in the experiment, is of course based on a subjective judgement.

The loss resistance is found to be in the range of 2 - 6 Ns/m. These results are shown in figure 4.4.

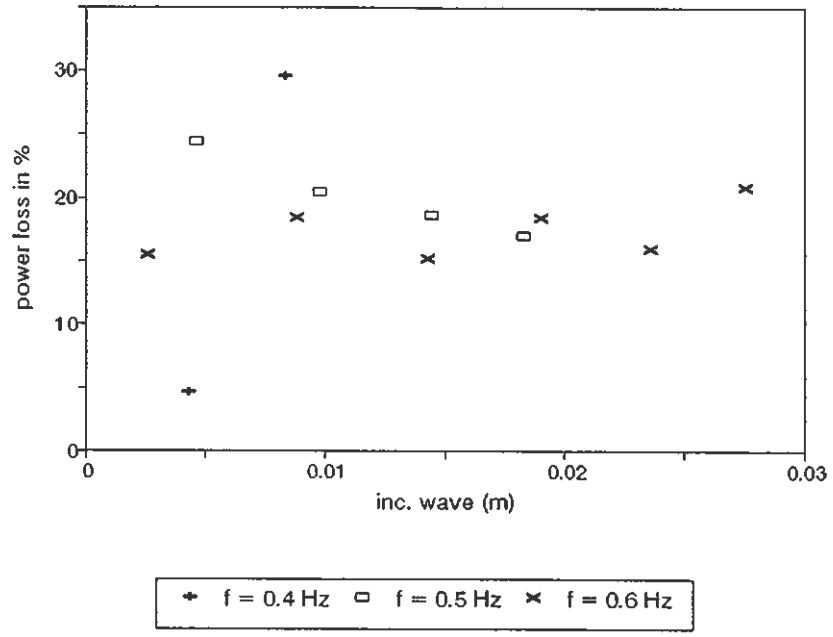

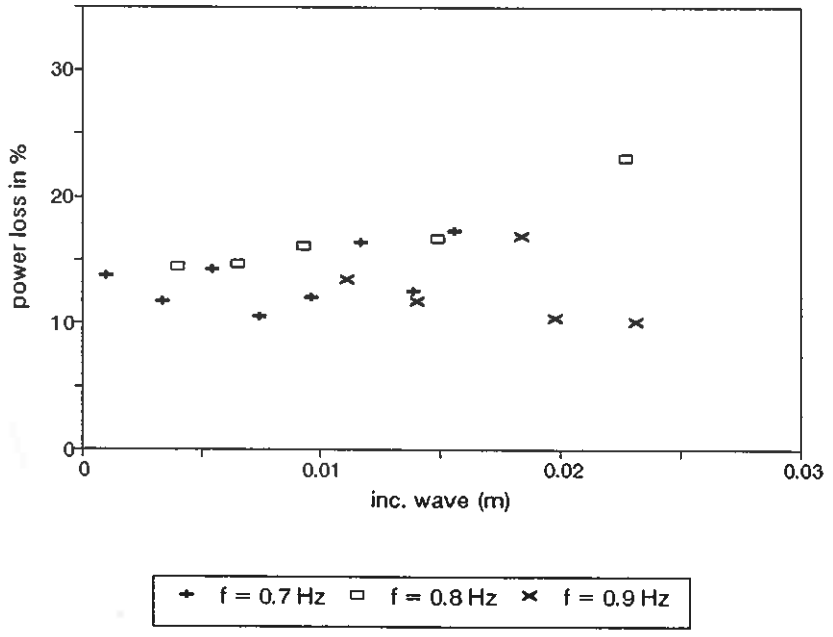

Figure 4.2: Loss in percent as a function of the incident wave amplitude for different wave frequencies: a) 0.4 Hz, 0.5 Hz and 0.6 Hz, b) 0.7 Hz, 0.8 Hz and 0.9 Hz.

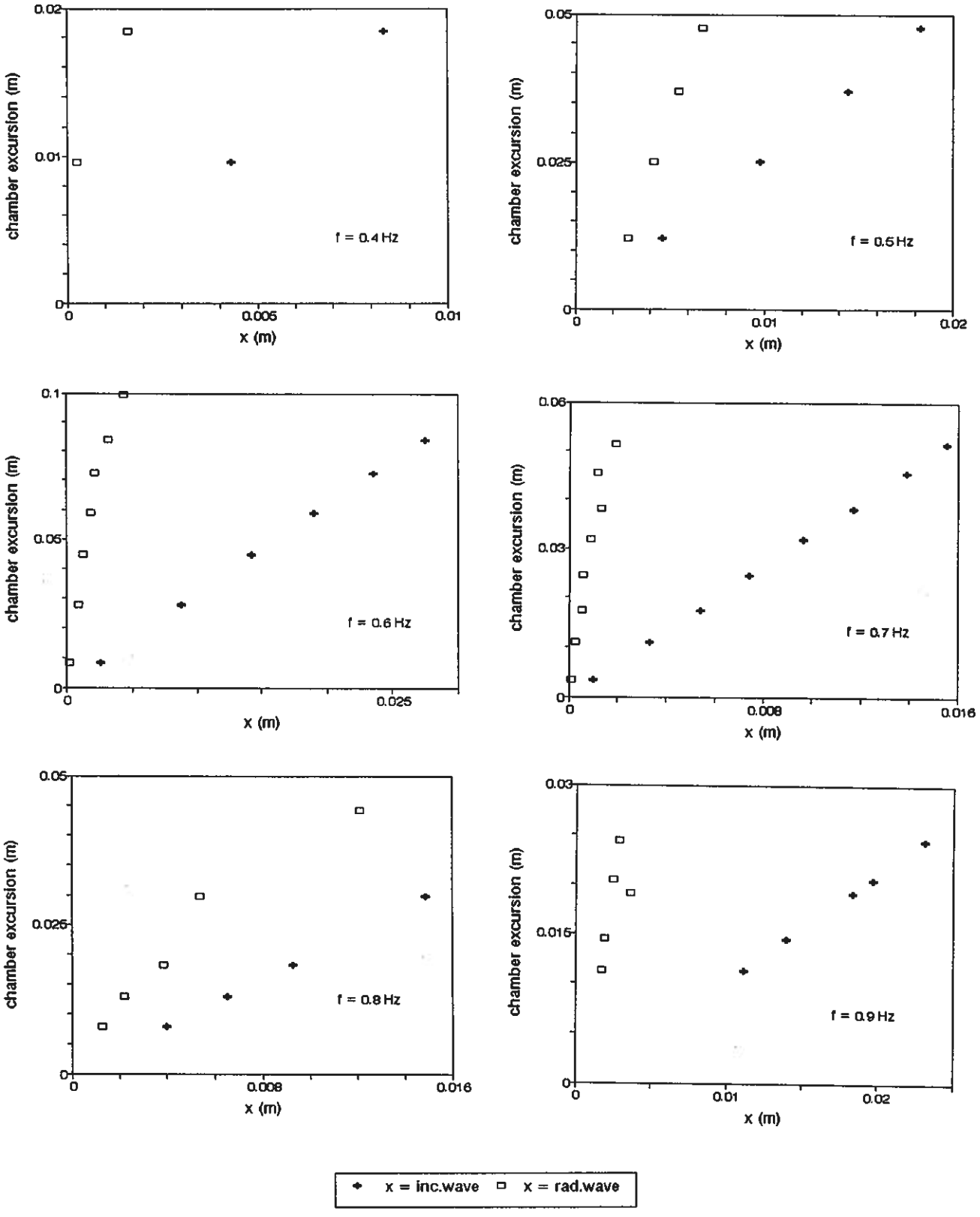

Figure 4.3: Chamber excursion amplitude as a function of the incident wave amplitude and the radiated wave amplitude. Each diagram corresponds to a different wave frequency. From top left to bottom right: a) 0.4 Hz, b) 0.5 Hz, c) 0.6 Hz, d) 0.7 Hz, e) 0.8 Hz, f) 0.9 Hz.

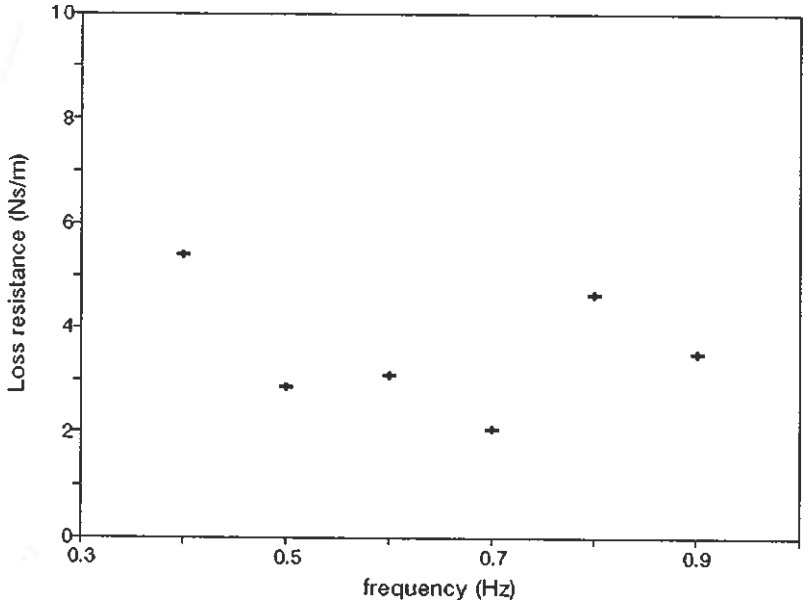

Figure 4.4: Loss resistance calculated for different wave frequencies.

4.2.3 Transient radiated wave experiment

The measurements have been hampered with large uncertainties, especially what the radiated wave is concerned. Hence, results obtained through the relations (4.25), (4.27), (4.28) and (4.29) have turned out to be inconclusive.

However, the loss resistance R_f have been calculated from equation (4.38). In this relation, R_f is calculated directly from the measured water surface excursion in the chamber. It is reasonable to assume that the relative uncertainty has been somewhat smaller in this quantity than in the radiated wave. Hence, eq. (4.38) provides an approximate check of the result obtained in section 4.2.2. According to eq. (4.38), the water surface excursion in the chamber should be integrated from $t = 0$ to $t = \infty$. In practice, however, we cannot integrate further than to $t = T_{reg}$. In order to determine whether it is sufficient to include time values up to $t = T_{reg}$, we derive the sequence

$$R_n = -\frac{\rho^2 g^2 S_k}{p_0} \int_0^{t_n} s_+(t)dt \qquad , n = 1, 2, ... \tag{4.39}$$

where t_n denotes the instant for zero-crossing no. n. By plotting experimental values of R_n as a function of n, we can check whether the solution converges towards a constant value. This is shown in figure 4.5. Figure 4.6 shows the details for the last values in figure 4.5. Since the series R_n has a somewhat alternating behaviour, we try to obtain a better convergence by calculating the quantity $R_{n/2}$ defined as $R_{n/2} = (R_{n+1} + R_n)/2$. This quantity is plotted as a function of n in the figures 4.7 and 4.8. Figure 4.8 shows the details for the last values of n. As we can see, we obtain the result $R_f \sim 2$ Ns/m, which agrees reasonably with the result obtained in section 4.2.2. However, the uncertainty has probably been considerable, so the result has to be regarded as an approximation only.

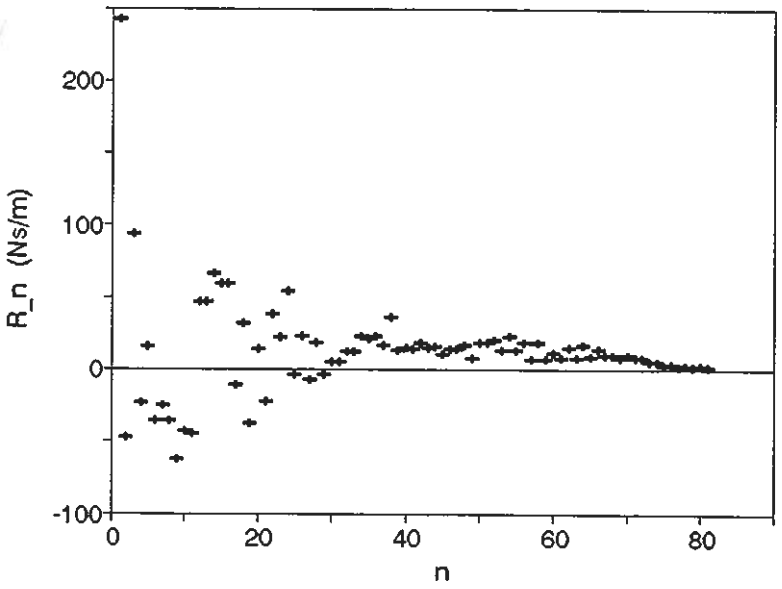

Figure 4.5: Partial integral approximation R_n of the loss resistance, as a function of number n of zero-crossings in the chamber excursion.

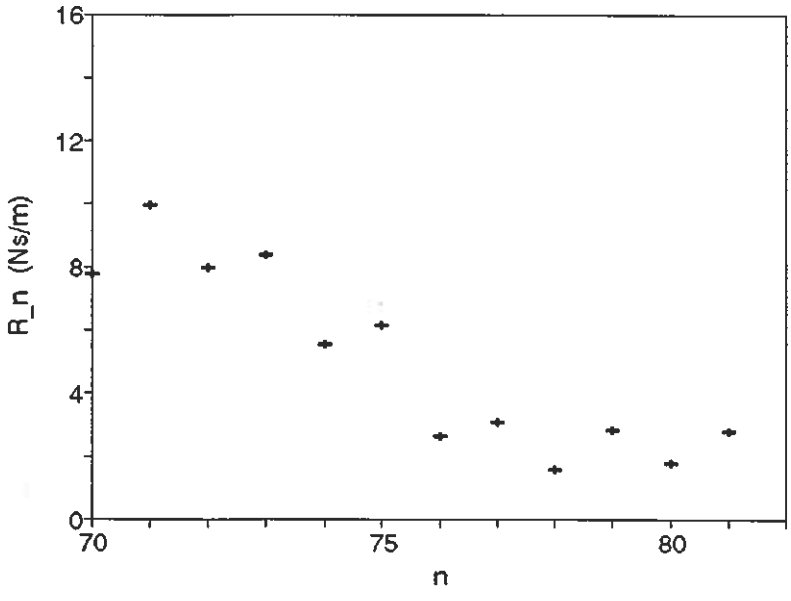

Figure 4.6: Partial integral approximation R_n of the loss resistance, as a function of number n of zero-crossings in the chamber excursion. Detail view of the last values of n.

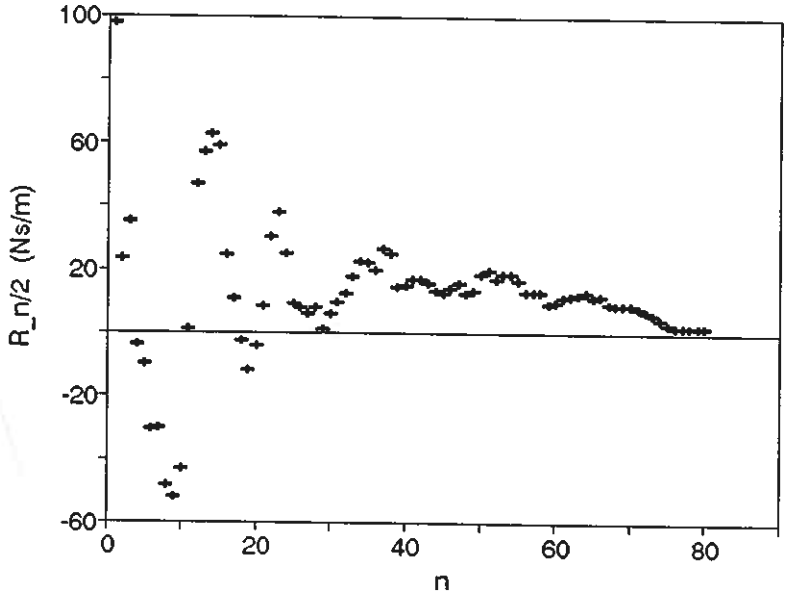

Figure 4.7: Averaged approximation $R_{n/2}$ of the loss resistance, as a function of number n of zero-crossings in the chamber excursion.

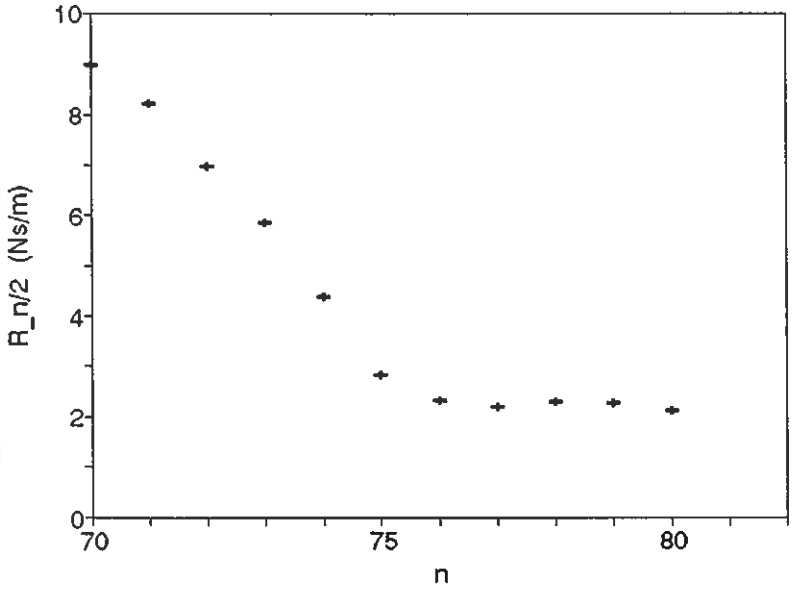

Figure 4.8: Averaged approximation $R_{n/2}$ of the loss resistance as a function of number n of zero-crossings in the chamber excursion. Detail view of the last values of n.

4.3 Discussion

As well as the radiation force, also the frictional loss force has to be a real, causal function of time. Since we have assumed a linear relationship between the friction force and the velocity, causality implies that the Kramers-Kronig relations (also called the Hilbert transforms) have to be satisfied [70]. Defining a *loss impedance* $Z_f = R_f + jX_f$, and requiring that $X_f = 0$ (that is, the loss mechanisms which are present in the system do not represent storage of energy, and do not cause any phase lag), the Kramers-Kronig relations state:

$$X_f(\omega) = 0 \qquad \text{for all } \omega \tag{4.40}$$

$$\Downarrow$$

$$R_f(\omega) - R_f(\infty) = 0 \tag{4.41}$$

Since $R_f(\infty)$ has to be a constant, we see that eq. (4.41) implies that R_f is independent of the wave frequency. Hence, the spread of the data in figure 4.4 has to be a result of experimental uncertainty. The average loss resistance may thus be written: $R_f = (3.6 \pm 1.2)$ Ns/m.

Since the lost power (4.8) is proportional to the difference between two not very different quantities, the relative uncertainty of the power loss may sometimes become large. Hence, it is not clear from the present investigation how the relative power loss depends on the wave frequency and the amplitude of the incident wave. Assuming, however, that the performance of the OWC has been within the linear region, which seems to be confirmed in figure 4.3, the relative loss should be independent of the incident wave amplitude. Hence, we take the spread of the results for each frequency in figure 4.2 as an approximate measure of the uncertainty in the relative power losses. Of course, the total uncertainty may be larger than the standard deviation of the obtained results. The average relative loss and the standard deviation is given in percent for each wave frequency in table 4.1. As seen from figure 4.2, the spread of the result for the frequency $f = 0.4$ Hz is larger than for the other frequencies. This is probably because the amplitude of the interior water surface has been very small at this particular frequency. Hence, the experimental uncertainty has been relatively large in this case.

Table 4.1: Losses in percent of the incident power, for each wave frequency.

frequency (Hz):	0.4	0.5	0.6	0.7	0.8	0.9
power loss (%):	17.1	20.2	18.3	13.6	18.2	12.6
std. dev. (%):	17.8	3.2	3.2	2.4	4.3	2.8

The results from the transient experiment are too inaccurate to provide useful information through the equations (4.25), (4.27), (4.28) and (4.29). The main reason for this inaccuracy is that the elevation of the radiated wave at this scale becomes very small. Hence, the absolute uncertainty of the measurements has been almost of the same order of magnitude as the elevation itself. Further, because the wave elevation has been so small, the reflections from the end of the flume may have been significant, in spite of the

absorbing beach. Since the flume is so short, the data acquisition could not be terminated before the reflection reached the wave gauges. However, using the measured water surface excursion in the chamber as the only input, the relation (4.39) have permitted an alternative way of calculating the loss resistance R_f. This result has turned out to be in good agreement with the result obtained from the incident wave experiment. The figures 4.5 - 4.8 show, however, that it is not obvious for what value of n the sequence $\{R_n\}$ in (4.39) should be terminated. Hence, the interpretations of these results is partly a matter of subjective judgement.

4.4 Conclusion

Assuming that the system is linear, we have determined the viscous losses and the loss resistance associated with a regular incident wave towards a single 2D OWC, with its chamber open to the atmosphere. The power loss averaged over the different investigated wave amplitudes, have been found to be in the range of 13 - 20 % of the incident wave power, depending on the wave frequency (see table 4.1). The loss resistance has been found to be in the range of 2.5 - 5.0 Ns/m. The uncertainty is estimated from the spread in the experimental data, and no uncertainty has been determined for each individual measurement. However, the approximately linear relationship found between the chamber excursion and the incident wave, and between the chamber excursion and the radiated wave, indicates a reasonably good agreement with linear theory, for the range of amplitudes investigated.

We have also performed experiments considering transient waves radiating from the 2D OWC model. These experiments have only provided an approximate check of the loss resistance obtained in section 4.2.2. The theory presented in section 4.1.3 shows that this kind of experiment may provide the loss resistance (due to two different methods of calculation), as well as the radiation resistance and the hydrodynamical added mass as functions of the wave frequency. It is, however, neccesary to achieve a better experimental accuracy in order to obtain reliable results at this model scale.

It would be of great importance to investigate whether the obtained power loss might be reduced by altering the inlet geometry of the model. Earlier work [54] has suggested that the shaping of the mouth and eventual harbour of the system, as well as the radius of curvature of the wall edges, are crucial to how much of the incident wave power that will be lost due to viscous effects. In future work, it will also be important to consider nonlinear loss effects, since a small OWC power plant may encounter wave states leading to nonlinearity a substantial part of the time.

Chapter 5

System equivalent diagrams for a single OWC

In this chapter we show how the the hydrodynamical description of a single OWC may be carried out in terms of symbolic diagrams, where the dynamic elements of the system are represented by its mechanical or electric equivalent elements. In a mechanical equivalent diagram, the reactive parts of the system will hence be described as springs and masses, whereas the parts converting or dissipating active power will be described in terms of mechanical resistances.

Likewise, an analog electric equivalent will contain inductances and capacitances symbolising the reactive elements, and electric resistances accounting for the active power conversion or dissipation in the system.

A mechanical equivalent diagram is presented for model I (the rigid-piston description), and analog electric diagrams are presented for both model I and model II. The relations connecting the electric equivalents for model I and model II, are based on the conversion formulas presented in section 2.1.1.

The equations in this chapter are presented in terms of a harmonic incident wave. However, the relations may easily be generalised to the case of a nonharmonic incident wave, by replacing the complex amplitudes with Fourier transforms. It is implied that the systems are assumed to be linear and time invariant.

5.1 Equivalent diagrams of model I

The rigid-piston description model (model I) is based on the fundamental relation (see eqs. (4.18) and (4.19)):

$$\hat{F}_{tot} = f_{e,I}\hat{A} - Z_w\hat{u} - \rho g S\hat{s} = Z_l\hat{u} \tag{5.1}$$

Here, $Z_w = Z_{r,I} + R_f$, where R_f is the loss resistance. The symbol $S = S_1 + S_2 = 2S_k$ is the total interior water surface area when the system acts as a single chamber. The term $-\rho g S\hat{s}$ represents the buoyancy force. Assuming linearity, the total force $\hat{F}_{tot}$ is considered to be proportional to the oscillation velocity amplitude of the interior water surface. This is shown in the last term in (5.1), where the proportionality coefficient Z_l is the mechanical load impedance. The term $f_{e,I}\hat{A}$ is the excitation force (proportional

to the amplitude $\hat{A}$ of the incident wave at $x = 0$), and $Z_{r,I}\hat{u}$ is the radiation force (proportional to the vertical velocity amplitude $\hat{u}$ of the oscillation in the chamber).

The radiation impedance $Z_{r,I}$ may be written: $Z_{r,I} = R_{r,I} + j\,X_{r,I} = R_{r,I} + j\omega m_{r,I}$. As mentioned earlier, $R_{r,I}$ is the radiation resistance, $X_{r,I}$ is the radiation reactance, and $m_{r,I}$ is the hydrodynamical added mass. Here, the interior water surface is regarded as a massless rigid piston, and all inertia due to the water is included as added mass. Hence, we may treat the system as an oscillating body on which different forces are acting. Some of these forces are due to stiffness, which may be symbolised by springs, while other forces are due to different mechanical resistances. As a first step, we express all forces in terms of complex mechanical impedances. The radiation impedance, which is described above, is one such impedance. Water friction may be included in the system by replacing $R_{r,I}$ by $R_{r,I} + R_f$, where R_f represents the loss resistance associated with friction in the water. Another contribution to the impedance in the system is due to the water buoyancy (hydrostatic stiffness). Lastly, we must include the load impedance, Z_l. The inertia of the system is exposed to the sum of the forces represented by these impedances, implying a parallel coupling in a mechanical diagram (figure 5.1).

The impedance due to buoyancy involves reactive power only, and must hence be entirely imaginary. It may be symbolised by a spring of stiffness $S_h = \rho g S$, and hence, the impedance becomes $Z_h = S_h/j\omega$. The load impedance, however, is partly due to the power take-off, and partly due to air compressibility in the chamber. As described in appendix C, the pneumatic admittances due to power take-off and air compressibility should be added to form the total pneumatic load admittance. Since a sum of admittances corresponds to a parallell coupling of impedances, this results in a mechanical load impedance of the form

$$Z_l = \left(\frac{1}{R_l} + \frac{1}{j X_l}\right)^{-1} = \frac{R_l\, j X_l}{R_l + j\, X_l} \tag{5.2}$$

Here, the mechanical load resistance R_l is due to the power take-off, while the mechanical load reactance X_l is a result from the air compressibility. Now, utilising that $\hat{F}_{tot} = S\hat{p}$ (cf. eqs. (2.23) and (4.18)), and that $\hat{Q} = S\hat{u} = \Lambda\hat{p}$ (cf. eqs. (2.22) and (2.49)), we obtain from eq. (5.1):

$$Z_l = S^2/\Lambda \tag{5.3}$$

Combining eqs. (5.2) and (5.3), and using that $\Lambda = G_l + j\omega V_0/\gamma p_a$ (see eq. (C.2)), we find that $R_l = S^2/G_l$, where G_l is the pneumatic load conductance due to the power take-off, and $X_l = S_{pn}/(j\omega)$, where $S_{pn} = \gamma S^2 p_a/V_0$ [58]. Hence, we obtain the mechanical equivalent diagram shown in figure 5.1.

Now we may identify the forces acting on the inertia in figure 5.1. The force acting on the uppermost branch, representing the hydrodynamical stiffness S_h, may be written

$$Z_h\hat{u} = \frac{S_h}{j\omega}\,\hat{u} = S_h\hat{s} = \rho g S\hat{s} \equiv -\hat{F}_s \tag{5.4}$$

that is, the buoyancy force. Further, the force acing on the middle branch is

$$R_r\hat{u} + R_f\hat{u} = -Re\{\hat{F}_r\} - \hat{F}_f \tag{5.5}$$

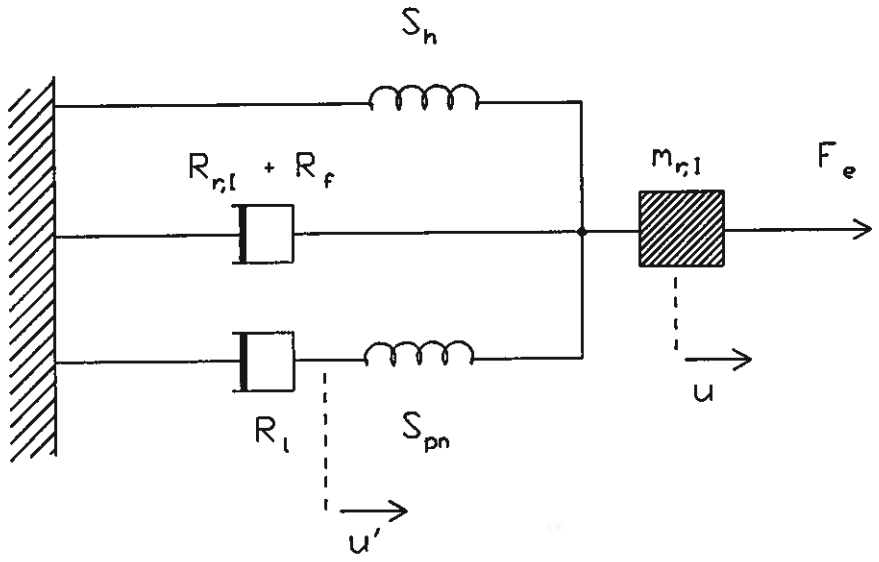

Figure 5.1: Mechanical equivalent of the rigid-body model (model I). Here, u is the velocity of the water surface, while u' is the velocity of the air at the power take-off. The rest of the symbols are defined in the text.

These are the active component of the radiation force and the force due to frictional loss. The last branch represents the load impedance $Z_l = R_l + S_{pn}/j\omega$. Hence, the force on this branch is

$$Z_l \hat{u} = \hat{F}_{tot} \tag{5.6}$$

by (5.1). From figure 5.1 we see that the sum of the forces on the inertia should be equal to $m_{r,I} j\omega \hat{u}$, by Newton's law of motion. Hence, we have

$$-\hat{F}_s - Re\{\hat{F}_r\} - \hat{F}_f + \hat{F}_{tot} = j\omega m_{r,I}\hat{u} + \hat{F}_e \tag{5.7}$$

Utilising that $j\omega m_{r,I} = Im\{Z_r\}$, we obtain

$$\hat{F}_{tot} = \hat{F}_e + \hat{F}_r + \hat{F}_f + \hat{F}_s \tag{5.8}$$

which is the total balance of forces in the system. To be prudent, it should be mentioned that the components $R_{f,I}$ and $m_{r,I}$ in figures 5.1 and 5.2 are dependent on the wave frequency.

The system may also be represented by an analog electric curcuit. Associating the mechanical impedances in the system with electric impedances, we see that the velocity u corresponds to an electric current, and the forces correspond to electric voltages. Further, by comparing the imaginary parts of a mechanical impedance and of an electric impedance, we see that the oscillating mass corresponds to an inductance, and a mechanical stiffness corresponds to the reciprocal of a capacitance [71].

With $\hat{F}_{e,I}$ as the driving force, we may regard $Z_m = \hat{F}_{e,I}/\hat{u}$ as the total mechanical impedance of the system. Since adding forces corresponds to a parallell coupling of

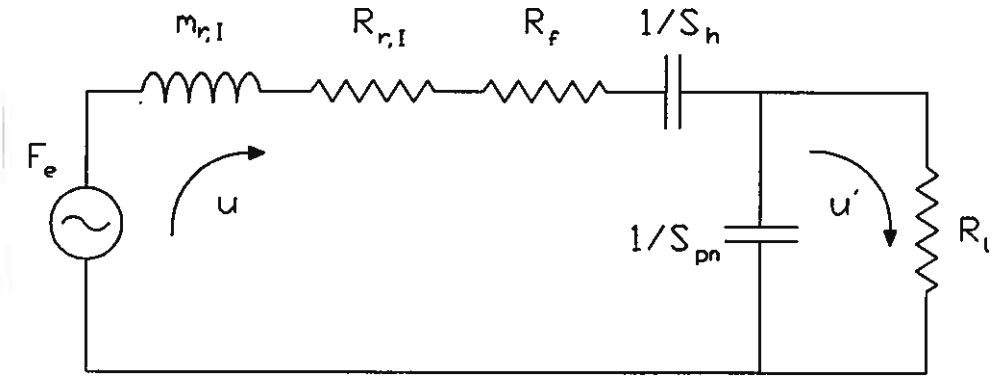

Figure 5.2: Analog electrical equivalent of model I.

impedances in the mechanical diagram, we see that a parallel coupling transforms into a serial coupling and vice versa when moving from a mechanical equivalent to an electric equivalent.

Hence, an electrical equivalent diagram may be represented as shown in figure 5.2. The excitation force $F_{e,I}$ is represented by a voltage source.

5.2 Analog electric equivalent diagram of model II

Using the transformation formulas derived in section 2.1.1, we may establish an electric equivalent scheme based on the applied-pressure description model (model II). Of cource, we may use the electric equivalent found in section 5.1 and then just transform the expressions from model I to model II. We find it more convenient, however, to implement the hydrodynamical parameters for the applied-pressure model directly, using the analogy between the hydrodynamical radiation admittance and the concept of an electric admittance. Consequently, we develope an electric equivalent curcuit based on the relation $I = Y_E U$, where I is the electric current, Y_E is the electric admittance, and U is the electric voltage. Hence, this circuit will contain a current source.

According to the applied-pressure model, a single OWC is described in terms of the relation (see equations (2.13) to (2.15)):

$$\hat{Q} = q_e \hat{A} - Y\hat{p} \tag{5.9}$$

Here, $\hat{Q}$ is the total volume flux. The term $q_e\hat{A}$ is the excitation volume flux, and $-Y\hat{p}$ is the radiation volume flux. It should be noted from eqs. (2.45) and (2.46) that if the radiation impedance $Z_{r,I}$ is replaced by $Z_w = Z_{r,I} + R_f$, the effect of friction in the water will correspond to a modification of both q_e and Y. The effect of linear frictional losses on the dynamics of model II is more closely considered in section 5.3.

The term $\hat{Q}_e = q_e\hat{A}$ represents the driving current of the system. Analogous to the former scheme, we may consider $Y_m = \hat{Q}_e/\hat{p}$ as the total pneumatic admittance of the circuit. Hence, the pressure $\hat{p}$ corresponds to the voltage drop across the total curcuit. The total volume flux in the chamber may be expressed $\hat{Q} = \Lambda\hat{p}$, where Λ is the load admittance. This results in the preliminary diagram shown in figure 5.3.

Now, we will determine the real parts and imaginary parts of each impedance in figure 5.3, and also, what parts should be coupled in series or what parts should be coupled in parallel. First, we consider the impedance $1/Y$. From model I, we have

$$Z' = Z_{r,I} + \rho g S/j\omega = R_r + j(\omega m_{r,I} - \rho g S/\omega) \tag{5.10}$$

where R_r accounts for the radiated energy, while the terms $\omega m_{r,I}$ and $-\rho g S/\omega$ are associated with kinetic and potential energy. The radiaton admittance of model II may be formulated similarily

$$Y = G + jB = G + j(B_p - B_k) \tag{5.11}$$

where B_k and B_p are the radiation susceptances defining the kinetic and potential energy associated with reactive power due to the radiated wave [72]. In analogy with an electric admittance, we may write

$$Y = G + j(\omega C_p - \frac{1}{\omega L_k}) \tag{5.12}$$

where C_p and L_k are analogs of a capacitance and an inductance, respectively. Hence, we have

$$B = \omega C_p - \frac{1}{\omega L_k} \tag{5.13}$$

or, from (5.11):

$$B_p = \omega C_p \tag{5.14}$$

$$B_k = \frac{1}{\omega L_k} \tag{5.15}$$

It should be remembered that C_p and L_k are dependent on the frequency.

From equation (2.46), we have for sufficiently low frequencies

$$Y = \frac{S^2}{Z'} = \frac{S^2}{|Z'|^2} Z'^* \tag{5.16}$$

where $Z' = Z_{r,I} + \rho g S/j\omega$. Hence, we obtain

$$B = Im\{Y\} = \frac{S^2}{|Z'|^2}(\frac{\rho g S}{\omega} - \omega m_{r,I}) \tag{5.17}$$

Comparing eqs. (5.13) and (5.17), we find that for low frequencies

$$C_p = \frac{\rho g S^3}{\omega^2 |Z'|^2} \tag{5.18}$$

and

$$L_k = \frac{|Z'|^2}{m_{r,I}\,\omega^2 S^2} \tag{5.19}$$

Since the terms G, B_k and B_p should be added to form the radiation admittance Y (see (5.11)), the corresponding electric curcuit elements should be coupled in parallel.

Now, we define a load impedance for model II, $Z_\Lambda = 1/\Lambda$, using the relation

$$\Lambda = G_l + jB_l \tag{5.20}$$

where G_l is due to the power take-off, and $B_l = \omega V_0/\gamma p_a$ is due to air compressibility (see section 3.1.2 and appendix C) [58]. Hence, we have a load impedance with its real and imaginary parts in parallell:

$$Z_\Lambda = \left(\frac{1}{R_\Lambda} + \frac{1}{jX_\Lambda}\right)^{-1} = \frac{R_\Lambda\, jX_\Lambda}{R_\Lambda + jX_\Lambda} \tag{5.21}$$

leading to

$$R_\Lambda = \frac{1}{G_l} \tag{5.22}$$

and

$$X_\Lambda = -\frac{1}{B_l} = -\frac{\gamma p_a}{\omega V_0} \tag{5.23}$$

Analog to a capacitance we may introduce a parameter C_Λ, which represents the air compressibility. Using the relation $jX_\Lambda = 1/(j\omega C_\Lambda)$, analogous to the relation between capacitance and its electric reactance, we obtain

$$C_\Lambda = \frac{V_0}{\gamma p_a} \tag{5.24}$$

Now we have defined all hydrodynamical parameters in terms of analog electric circuit elements, and we obtain the final analog electric equivalent diagram shown in figure 5.4.

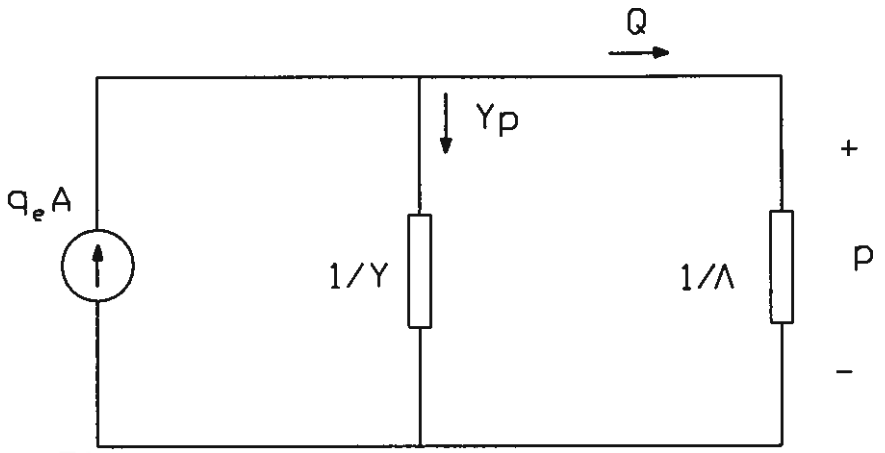

Figure 5.3: Simplified analog electric equivalent of model II.

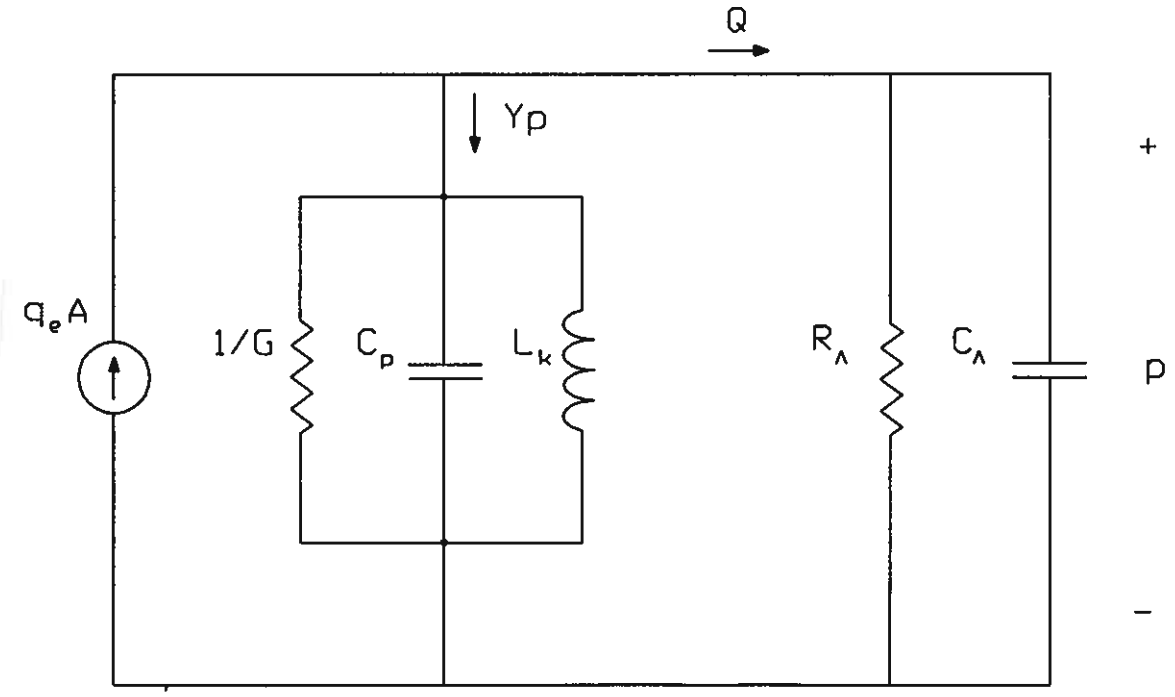

Figure 5.4: Analog electrical equivalent of model II. The parameters are defined in the text.

5.3 Loss parameters in model II

As mentioned in section 4.3, frictional losses in model I may be described in terms of a mechanical resistance R_f. Assuming causality and linearity, R_f is independent of both the frequency and the wave amplitude. Hence, the loss force may easily be described both in the frequency domain and the time domain, as $\hat{F}_f(\omega) = -R_f\hat{u}(\omega)$ and $F_f(t) = -R_f u(t)$, respectively. Still assuming the loss to be linear, we now wish to establish a similar description of the losses in terms of model II.

We define a loss parameter G_f from the definition

$$Y' = \left(\frac{1}{Y} + \frac{1}{G_f}\right)^{-1} = \frac{YG_f}{Y + G_f} \tag{5.25}$$

where Y' is the radiation admittance with losses included. This definition is consistent with the sum $Z_w = Z_{r,I} + R_f$ in model I.

For sufficiently low frequencies, we may utilise the conversion formulas between model I and model II obtained in section 2.1.1. Hence, we obtain from eq. (2.46)

$$Y' = \frac{S^2}{Z_{r,I} + R_f + \rho g S/j\omega} \tag{5.26}$$

and

$$Y = \frac{S^2}{Z_{r,I} + \rho g S/j\omega} \tag{5.27}$$

Inserting (5.26) and (5.27) into (5.25), we find

$$G_f = \frac{S^2}{R_f} \tag{5.28}$$

We see that G_f is a real constant. However, the excitation volume flux coefficient will also be influenced by the loss effects, and as shown below, this quantity will be dependent on Y. Combining eqs.(2.45) and (2.48) with no losses included, we obtain

$$q_e = \frac{f_{e,I}Y}{S} \tag{5.29}$$

and similarily, *with* losses included,

$$q'_e = \frac{f_{e,I}Y'}{S} \tag{5.30}$$

Now, combining (5.29) and (5.30), we find

$$q'_e = q_e\frac{Y'}{Y} = q_e\frac{G_f}{Y + G_f} \tag{5.31}$$

Utilising the definition

$$\frac{1}{q'_e} = \frac{1}{q_e} + \frac{1}{q_{e,f}} \tag{5.32}$$

where $q_{e,f}$ may be termed the *loss excitation volume flux coefficient*, we insert (5.32) into (5.31) and obtain

$$q_{e,f} = q_e \frac{G_f}{Y} \tag{5.33}$$

An analog electric equivalent diagram of model II with loss included, is shown in figure 5.5.

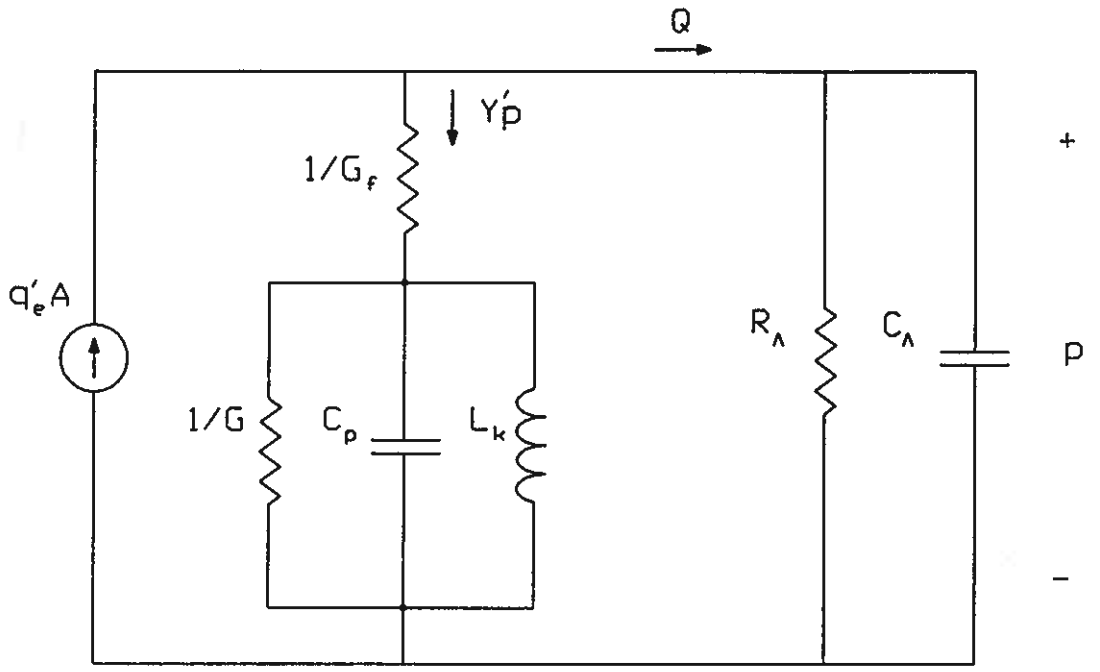

Figure 5.5: Electrical equivalent of model II, with loss included.

In order to determine whether the obtained loss parameters seem reasonable, we consider the excitation problem and the radiation problem separately. With losses included, the excitation problem becomes

$$\hat{Q}' = q_e' \hat{A} = q_e \frac{G_f}{Y + G_f} \hat{A} = \hat{Q}_e \frac{G_f}{Y + G_f} \tag{5.34}$$

Since $Re\{Y\}$ is always positive, we see from (5.34) that $|\hat{Q}'| \leq |\hat{Q}|$. This is in agreement with our expectations, since losses should reduce the volume flux in the chamber due to an incident wave. The radiation problem with losses may be formulated

$$\hat{Q}' = -Y'\hat{p} = -\frac{YG_f}{Y + G_f} \hat{p} = \hat{Q}_r \frac{G_f}{Y + G_f} \tag{5.35}$$

Similar to what we find above, we obtain from (5.35) that $|\hat{Q}'| \leq |\hat{Q}|$. This is also reasonable, since losses should reduce the system's ability to radiate waves.

It should be noted that the conversions between model I and model II do only apply for frequencies sufficiently low for the rigid-piston approximation to be valid. Hence, the expression (5.28) is not valid for high frequencies. However, we may still use the

parameters G_f and $q_{e,f}$ as defined above, but they would in general have to be determined directly, by some kind of experiment. We do also assume that G_f is a real constant in any case, for the same reasons that R_f is a real constant (see section 4.3), that is, there is no reactive power associated with the viscous loss mechanisms, and the radiation problem is causal [70].

5.4 Computations on mechanical equivalents

A computer program has been worked out, utilising the mechanical equivalent diagram of model I (see figure 5.1). Hence, given the dimensions of a single OWC, as well as the load conductance and the amplitude and period of a regular, incident wave, the program calculates the quantities of the equivalent in figure 5.1. Hence, we may obtain the excitation force coefficient $f_{e,I}$ and the radiation impedance $Z_{r,I}$ (cf. eq. (5.1)). By means of the conversion relations (2.45 - 2.46), also the applied-pressure parameters may be calculated, that is, the excitation volume flux coefficient q_e and the radiation admittance Y. The program derives other quantities as well, such as the pneumatic power, the oscillation velocity of the interior surface, and also, provided a loss resistance is properly chosen, the power loss and the useful power.

It should be noted that in addition to being a simplification of the dynamic system, the model has other features calling for caution when comparing with experiments. Firstly, the power take-off in the program is considered to be linear, that is, the load conductance is a constant which is chosen from the keyboard before each run. In the experiments, the orifices constitute a nonlinear power take-off, and the load conductance will hence be a function of the instantaneous chamber pressure. Thus, the calculated useful power will only be an approximation to the experimental value.

Secondly, the hydrodynamical added mass, which in the rigid-piston description includes the total inertia of the system, is assumed to be a constant in the program, given by the dimensions of the system. This is also an approximation, since this quantity in reality will depend on the wave period.

These simplifications make it interesting to compare such equivalents to experiments. Hence, if the agreement is reasonable, we know that such a simplified description may be a sufficient basis for further investigations.

The computations performed by means of this equivalent program have been carried out in to parts. In the first part we calculated the absorption width of the system. Figure 5.6 shows the absorption width calculated by the program for different load conductances, compared to corresponding experimental results for a single OWC without phase control. The experimental results have been obtained from the incident wave experiment described in chapter 2. Because of the nonlinearity of the orifices, the load conductance have been varying as a function of time during the experiments, even within each run. Hence, we cannot associate a fixed value of the load conductance to the entire experimental curve in figure 5.6. In order to compare, the computations by means of the equivalent program have been carried out for different load conductances, chosen within the same range of variation as in the experiments. According to figure 5.6, the results from the computations seem to agree reasonably with experiments. The input parameters during

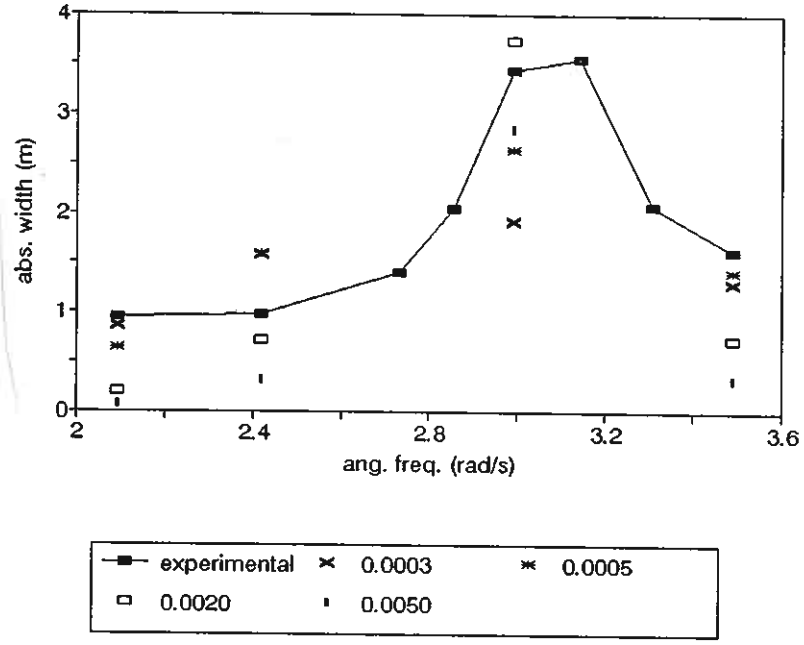

Figure 5.6: The absorption width $d_{abs} = P/J$ as a function of angular frequency, calculated for different values of the load conductance (in $m^3/(s\,Pa)$). Results calculated by the equivalent circuit program are compared to experimental results. Lines are drawn between the experimental values in order to improve readability.

this part of the calculations were: an incident wave with amplitude of 0.05 m and angular frequencies in the range of 2.1 - 3.5 rad/s, and load conductances in the range of 0.0003 - 0.0050 $m^3/(s\,Pa)$ for each frequency.

In the second series of computations, we calculated the modulus of the radiation admittance through the conversions formulas (2.45 - 2.48) described in section 2.1.1. Figure 5.7 shows these calculated quantities for different loss resistances. The results calculated by the program are here compared to results from the transient experiment in chapter 3. The loss resistance R_f of the model OWC in this experiment is not known. However, based on the value of R_f found for the case of the smaller-scale experiment in chapter 4, we have assumed a reasonable range of loss resistances, and performed the computations for different values of R_f within this range. The results shown in figure 5.7 show that the loss resistance is of small importance for other frequencies than the resonance frequency. The peak value of the experimental result seem to coincide with a loss resistance of about $R_f = 20$ kg/s. The agreement between calculations and experimental results for the total range of investigated wave frequencies, seems to be good. During this calculation series, the input parameters still included an incident wave with an amplitude of 0.05 m and angular frequencies in the range of 2.1 - 3.5 rad/s. The load conductance being of no concern for the radiation problem, was set to zero. However, the loss resistance R_f was varied in the range og 0 - 100 Ns/m for each wave frequency.

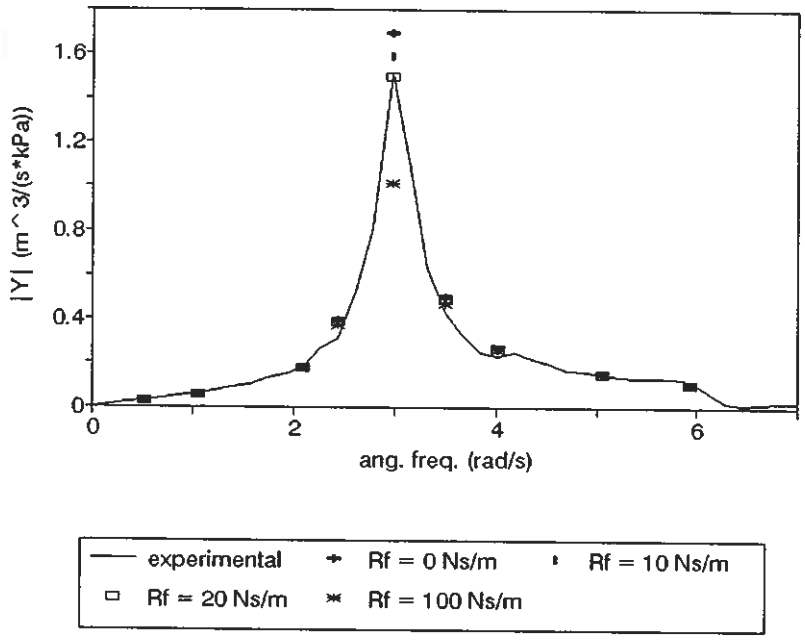

Figure 5.7: The modulus of the radiation admittance as a function of angular frequency, calculated for different values of the loss resistance. Results calculated by the equivalent curcuit program are compared to experimental results. Lines are drawn between the experimental values in order to improve readability.

5.5 Conclusion

In this chapter we have shown how we may develop relatively simple equivalent diagrams of the dynamics of a single OWC, by utilising the analogy between the dynamic elements of the system and corresponding elements of a mechanical mass-spring system or an analog electric circuit. Moreover, we have shown how the conversion between the two hydrodynamical description models previously presented in section 2.1.1, is being reflected through the interrelated quantities describing the two electric equivalent diagrams.

A crucial point in this investigation have been to point out how linear power loss may be modelled in terms of the applied-pressure model. It should be noted, however, that the derived expressions for the loss parameters G_f and $q_{e,f}$ are valid only for sufficiently low frequencies. For higher frequencies, these parameters may still be used to describe loss effects, but will probably have to be determined by means of separate experiments.

The calculation program mentioned in section 5.4 has been based on our model I. The conversion formulas in the program may however be utilised to investigate how loss effects influence the results in terms of both the description models, provided that the wave frequency is not too high.

We have also shown how the load conductance may be varied in the program, thereby allowing a direct comparison with experiments using a linear power take-off. Hence, the program may provide an approximate suggestion of the optimum load conductance of a real OWC. The calculation program may of course be improved by implementing a better approximation of the hydrodynamical added mass, than just a constant determined by the geometry of the system.

The work in this chapter may be generalised by developing similar equivalent diagrams for the twin OWC. Further, if the loss parameters for model II can be determined experimentally for high frequencies, a corresponding calculation program, based directly on the applied-pressure description may also be developed.

Chapter 6

General conclusion

In this thesis we have presented two hydrodynamical description models for a twin OWC. One model is an approximation regarding the interior water surfaces as horizontal, rigid pistons. The other model is a more accurate description, defined in terms of the dynamic air pressure and the volume flux of air in the chambers. We have shown how we can convert the system description from one model to the other, provided that the rigid-piston model is valid as a reasonable approximation.

We have investigated discrete phase control of a twin OWC model in regular incident waves, by means of operable air valves. The physical model was constructed with some of its main dimensions to be in scale 1:10, compared to the full-scale plant previously built by Kværner Brug [14]. A set of criteria for a satisfactory control strategy has been presented. We do not know, however, whether this strategy is optimum or somewhat suboptimum. The pneumatic power has been increased by a factor of 3 for a wave period of 3.0 s, compared to results with the system acting as a single OWC without phase control. The corresponding increase factor for a wave period of
3.5 s, was 1.7. The resonance period of our system is approximately 2.1 s.

Further, we have performed experiments considering a transient wave radiating from the same OWC model. This wave was produced by means of an initial stationary pressure applied to one of the chambers. From these experiments the impulse response matrix has been determined, and hence, hydrodynamical parameters in the frequency domain, as well. A time-domain mathematical model is presented, with the experimentally determined impulse response matrix implemented as convolution integral kernels. This model provides the possibility to perform time-domain simulations of the system.

In another experiment, carried out in scale 1:30, we have been considering a single two-dimensional OWC in a narrow wave channel. Here also, both incident waves and transient outgoing waves have been investigated. The aim of this work, was to determine linear power losses associated with friction in the water, and the loss resistance describing these losses. The amount of lost power relative to the incident power has been found to be in the range of 13 - 20 %, depending on the wave period. The loss resistance has been found to be in the range 2.5 - 5.0 Ns/m.

Finally, we have presented equivalent diagrams for a single OWC, describing the system in terms of a symbolic mechanical or electric oscillation system. Such diagrams constitute simple bases for theoretical computations of hydrodynamical parameters. One

of the equivalent diagrams is implemented in a computer program, and compared to experimental results. This comparison shows a good agreement.

The chapters 2 to 5 of the thesis consider various experimental and theoretical aspects related to OWCs. The chapters are interrelated through some common items. One such item is a general survey of the hydrodynamic theory of OWCs, which has been presented in several ways. The two different hydrodynamical description models was presented in section 2.1.1 and was later utilised in the construction of the equivalent diagrams in chapter 5. A more general outline of the hydrodynamics was presented in the frequency domain, in chapter 2, and also in the time domain, in chapter 3.

An experimental investigation of phase control was carried out directly in chapter 2. However, the hydrodynamical parameters and the time-domain mathematical model obtained in chapter 3 allows such an investigation to be accomplished through simulation, as well.

Another important feature in this work, has been to determine parameters describing viscous losses in the system. This has been carried out experimentally in chapter 4, but it has also been discussed theoretically in chapter 2, in connection with the conversion formulas between the hydrodynamical description models, and by implementing these loss parameters in our equivalent diagrams in chapter 5.

The equivalent diagrams and programs developed in chapter 5, and the time-domain simulation model suggested in chapter 3, are expected to provide powerful tools for investigating the hydrodynamics of OWC systems, as well as various strategies for phase-controlling such a system.

Before the achieved results can be transfered to a full-scale OWC power plant, some reservations have to be made. Firstly, a real power plant will be equipped with an air turbine for power take-off, while the results in this thesis have been obtained using orifices. The relationship between the dynamic air pressure and the volume flux will be different in turbines and in orifices. Secondly, there will be an electric generator connected to the turbine in a real power plant. Such elements have been neglected during these experiments. Furthermore, the larger dimensions will cause air compressibility to be of greater importance in the full-scale case than in the model scale. Finally, and probably most inportant, a real power plant will be exposed to irregular waves, making it neccesary to predict the incident wave some seconds into the future, in order to make phase control possible [46,47,48].

Comparing a full-scale twin OWC with phase control to a conventional single OWC without control, but with the same overall size, we see that we can probably achieve a substantial increase in the useful power, provided that wave prediction and a good strategy for the control can be realised. It is, however, important to identify the additional costs associated with the control system. Obviously, the air valves will increase the total construction costs. Further, the gauges and electronic curcuits providing the prediction and control, will represent extra expenses. However, assuming that the control strategy is implemented as a software algorithm, these parts will constitute a small portion of the total costs, and in particular so if plants are mass produced in the future.

The results in this thesis suggest that the controlled system may need a physically smaller turbine than the system without phase control. This may represent an economical advantage. Further, the controlled system requires that an extra wall is built into the

structure, dividing the chamber in two parts. This may represent an extra cost, but it is also possible that such a wall will make the total structure more rigid. Hence, the total material costs of the structure may even be reduced.

The next steps towards an eventual full-scale power plant, should be development of methods for wave prediction, and tests of phase control in irregular seas. Further, it is an aim to utilise a simulation program based on the time-domain model derived in the present work. Such simulations provide a useful check of the obtained results, as well as a tool for extensive test series of different control strategies.

Bibliography

[1] Ross, D.: *Energy from the Waves*, 2nd edition, Pergamon Press, 1981. pp. 1-4.

[2] Stahl, A.W.: The utilization of the power of ocean waves. Meeting of the American Society of Mechanical Engineers, San Fransisco (1892). Vol. XIII, pp. 438-506.

[3] Leischman, J.M. and Scobie, G.: The development of wave power - a techno-economic study. Economic Assessment Unit, National Engineering Laboratory (NEL), Glasgow, Scotland, UK (1976).

[4] Palme, A.: Wave motion turbine. Power 52 (1920). pp. 700-701.

[5] Masuda, Y.: Study of wave activated generator and future view as an island power source. 2nd Int. Ocean Development Conference (1972). Preprints 2, pp. 2074-2090.

[6] Whittaker, T.J.T., Robinson, R.W., Murray, M.A.: Hydrodynamic study of an oscillating water column wave energy converter. Int. Conference of Future Energy Concepts (1981), IEE Conf.,Pub. 192, pp. 143-146.

[7] Moody, G.W., Elliott, G.: The development of the NEL breakwater wave energy converter. 2nd Int. Symposium of Wave Energy Utilization, Trondheim, Norway (1982). Proceedings, pp. 421-451.

[8] French patent application filed 1952-04-11. See GB patent specification 741, 494 published 1955-12-07.

[9] Budal, K. and Falnes, J.: Proposals for conversion of the energy in ocean waves. Internal report, 1974, Division of Experimental Physics, University of Trondheim.

[10] Moody, G.: The NEL oscillating water column: recent developments. 1st. Symposium of Wave Energy Utilization, Gothenburg, Sweden (1979). Proceedings, pp. 283-297.

[11] Lewis, A.: private communication, 1983.

[12] Falcão, A.F. De O. and Sarmento, A.J.N.A.: Wave generation by a periodic surface pressure and its application in wave-energy extraction. 15th Int. Cong. Theor. Appl. Mechanics, Toronto, Canada (1980).

[13] Masuda, Y.: An experience of wave power generator through tests and improvement. *Hydrodynamics of Ocean-Wave Energy Utilization*, Evans, D.V. and Falcão, A.F. de O. (editors), IUTAM Symposium, Lisbon, Portugal (1985), Springer Verlag, Berlin, 1986, pp. 445-452.

[14] Malmo, O.: Private communication, 1986.

[15] Raju, V.S., Ravindran, M., Koola, P.M.: Energy from sea waves - the Indian wave energy programme. 3rd Symposium on Ocean Wave Energy Utilization, JAMSTEC, Japan (1991). Proceedings, pp. 405-413.

[16] Zheng, W.: Experimental research and parameters optimization of prototype OWC wave power device. Int. Conference on Ocean Energy Recovery, Hawaii, USA (1989).

[17] Ohno, M., Funakoshi, H., Saito, T.: Interim report on the second stage of field experiments on a wave power extracting caisson in Sakata port. Internation Symposium on Ocean Energy Development, Muroran, Hokkaido, Japan (1993). Proceedings, pp. 173-182.

[18] Raju, V.S., Ravindran, M., Koola, P.M.: Experiences on a 150 kW wave energy pilot plant. European Wave Energy Symposium, Edinburgh, Scotland, UK (1993). Proceedings, pp. 277-282.

[19] Yu, Z., Jiang, N., You, Y.: Power output of an offshore OWC wave power station at Dawanshan Island. European Wave Energy Symposium, Edinburgh, Scotland, UK (1993). Proceedings, pp. 271-276.

[20] Whittaker, T.J.T., McIwaine, S.J., Raghunathan, S.: A review of the Islay shoreline wave power station. European Wave Energy Symposium, Edinburgh, Scotland, UK (1993). Proceedings, pp. 283-288.

[21] Falcão, A.F. de O., Whittaker, T.J.T., Lewis, A.W.: Joule II preliminary action: European pilot plant study. European Wave Energy Symposium, Edinburgh, Scotland, UK (1993). Proceedings, pp. 247-257.

[22] Masuda, Y.: Wave power electric generation study in Japan. 1st International Symposium on Wave and Tidal Energy, BHRA, Bedford, England (1978). Proceedings, vol. 1, paper B6, pp. B85-B92.

[23] Whittaker, T. and Wells, A.: Experiences with a Hydropneumatic Wave Power Device. 1st International Symposium on Wave and Tidal Energy, BHRA, Bedford, England (1978). Proceedings, pp. B4-57.

[24] Malmo, O. and Reitan, A.: Development of the Kværner multiresonant OWC. *Hydrodynamics of Ocean-Wave Energy Utilization*, Evans, D.V. and Falcão, A.F. de O. (editors), IUTAM Symposium, Lisbon, Portugal (1985), Springer Verlag, Berlin, 1986, pp. 57-67.

[25] *Norske Bølgekraftverk*, Ministry of Petroleum and Energy, Norway, 1987.

[26] Sarmento, A.J.N.A., Gato, L.M.C. and Falcão, A.F. de O.: Wave energy absorption by an OWC device with blade-pitch controlled air turbine. 6th Int. Offshore Mech. and Arctic Engineering Symposium, Houston, USA (1987). Proceedings, pp. 465-473.

[27] Miyazaki, T., Yokomizo, H., Hotta, H. and Washio, Y.: A fundamental research of air flow phase control for improving on wave power absorption. *Journal of the Kansai Society of Naval Architects*, No.188, 1983.

[28] Hotta, H., Miyazaki, T., Washio, Y. and Aoki, Y.: Fundamental study of phase control for air flow to improve on wave power absorption. *Journal of the Kansai Society of Naval Architects*, No.194, 1984.

[29] Greenhow, M.J.L., Rosen, J.H. and Reed, M.: Control strategies for the Clam wave energy device. *Applied Ocean Research*, Vol.6 (4), 1984, pp. 197-206.

[30] Hoskin, R.E., Count, B.M., Nichols, N.K. and Nicol, D.A.C.: Phase control for the oscillating water column. *Hydrodynamics of Ocean Wave-Energy Utilization*, Evans, D.V. and Falcão, A.F. de O. (editors), IUTAM Symposium, Lisbon, Portugal (1985). Springer Verlag, Berlin, 1986, pp. 257-268.

[31] Jefferys, R. and Whittaker, T.: Latching control of an oscillating water column device with air compressibility. *Hydrodynamics of Ocean Wave-Energy Utilization*, Evans, D.V. and Falcão, A.F. de O. (editors), IUTAM Symposium, Lisbon, Portugal (1985). Springer Verlag, Berlin, 1986, pp. 281-291.

[32] Iversen, L.C.: Numerical simulation of a phase controlled oscillating water column. Technical report, Institutt for eksperimentalfysikk, NTH, Trondheim, 1983.

[33] Budal, K.: Private communication, 1982.

[34] Evans, D.V.: Wave power absorption by systems of oscillating surface pressure distributions. *Journal of Fluid Mechanics, 114*, 1982, pp. 481-499.

[35] Falnes, J.: A short note on the relation between rigid-piston and applied-pressure descriptions of OWCs. Unpublished note, Institutt for fysikk, NTH, Trondheim, 1992.

[36] Evans, D.V.: A theory for wave-power absorption by oscillating bodies. *Journal of Fluid Mechanics*, vol. 77, part 1, 1976, pp. 1-25.

[37] Evans, D.V.: Ibid. section 4.

[38] Evans, D.V.: Power from water waves. *Ann. rev. Fluid Mech.*, 13, 1981, pp. 157-187.

[39] Budal, K. and Falnes, J.: Interacting point absorbers with controlled motion. *Power from Sea Waves*, Count, B. (editor), Academic Press, London, 1980, pp. 381-399.

[40] Falnes, J.: Small is beautiful: How to make wave energy economic. European Wave Energy Symposium, Edinburgh, Scotland, UK (1993). Proceedings, pp. 367-372.

[41] Budal, K. and Falnes, J.: Optimum operation of improved wave power converter. *Marine Science Communications, 3*, 1977, pp. 133-150.

[42] Salter, S. et. al.: The Architecture of Nodding Duck Wave Power Generators. *The Naval Architect*, January, 1976, pp. 21-24.

[43] Falnes, J. and Budal, K.: Wave power conversion by point absorbers. *Norwegian Maritime Research*, Vol. 4, No. 6, 1978, pp. 1-11.

[44] Budal, K., Falnes, J., Hals, T. and Onshus, T.: Model experiment with a phase-controlled point absorber. 2nd International Symposium on Wave and Tidal Energy, 1981, Cambridge, UK.

[45] Budal, K., Falnes, J., Iversen, L.C., Lillebekken, P.M., Oltedal, G., Hals, T., Onshus, T.: The Norwegian wave-power buoy project. 2nd Int. Symposium of Wave Energy Utilization, Trondheim, Norway (1982). Proceedings, pp. 323-344.

[46] Naito, S. and Nakamura, S.: Wave energy absorption in irregular waves by feed-forward control system. *Hydrodynamics of Ocean-Wave Energy Utilization*, Evans, D.V. and Falcão, A.F. de O. (editors), IUTAM Symposium, Lisbon, Portugal (1985), Springer Verlag, Berlin, 1986, pp. 269-280.

[47] Perdigão, J.N.B.A. and Sarmento, A.J.N.A.: A phase control strategy for OWC devices in irregular seas. *The 4th. International Workshop on Water Waves and Floating Bodies*, Grue, J. (editor), Øystese, Norway (1989), pp. 205-209.

[48] Sarmento, A.J.N.A., Gato, L.M.C. and Falcão, A.F. de O.: Turbine-controlled wave energy absorption by oscillating water column device. *Ocean Engineering*, 1990, Vol. 17, No. 5. pp. 481-497.

[49] Falnes, J: Radiation impedance matrix and optimum power absorption for interacting oscillators in surface waves. *Applied Ocean Research*, 1980, Vol. 2, No. 2, pp. 75-80.

[50] See e.g. Gerhart, M. and Gross, J.: *Fundamentals of Fluid Mechanics*, Addison-Wesley, 1985. pp. 485-486.

[51] Oltedal, G. and Bøe, T.: Bølgekraftverk modellforsøk - enkammer og tokammer svingende vannsøyle. Technical report, Marintek, Trondheim, 1991.

[52] Sarmento, A.J.N.A.: Wave flume experiments on two-dimensional oscillating water column wave energy devices. *Experiments in Fluids*, 1992, 12, pp. 286-292.

[53] Sarmento, A.J.N.A. and Falcão, A.F. de O.: Wave generation by an oscillating surface-pressure and its application in wave-energy extraction. *Journal of Fluid Mechanics*, 1985, Vol. 150, pp. 467-485.

[54] Lillebekken, P.M.: Private communication, 1994.

[55] Falnes, J.: Vurdering av energitap ved opning av ventil med trykkskilnad over. Unpublished note, NTH, 1989.

[56] Sarmento, A.J.N.A.: Semi-empirical simulation of a 0.3 MW OWC power plant. 3rd Symposium on Ocean Wave Energy Utilization, JAMSTEC, Japan (1991). Proceedings, pp. 385-393.

[57] Sarmento, A.J.N.A.: Private communication, 1992.

[58] See e.g. Gerhard, P.M. and Gross, R.J.: *Fundamentals of Fluid Mechanics*, Addison-Wesley, 1985, pp. 668-675.

[59] Falnes, J.: *Surge excitation force vector and radiation impedance matrix for a rigid-piston model of a double OWC in a wave channel.* School of Mathematics, University of Bristol, 1987.

[60] See e.g. Burden, R. and Faires, J.D.: *Numerical Analysis*, 5th edition, PWS-Kent, 1993, pp. 56-58 and 553-557.

[61] See e.g. Papoulis, A.: *The Fourier integral and its applications*, McGraw-Hill, 1962, pp. 18-20.

[62] Ibid., pp. 50-52.

[63] Ibid., pp. 36-40.

[64] Ursell, F.: The decay of the free motion of a floating body. *Journal of Fluid Mechanics*, 1964, Vol. 19, pp. 305-319.

[65] Falnes, J.: Wave-power absorption by an array of attenuators oscillating with unconstrained amplitudes. *Applied Ocean Research*, 1984, Vol. 6, pp. 16-22.

[66] Budal, K., Falnes, J., Kyllingstad, Å. and Oltedal, G.: Experiments with point absorbers. First symposium on Wave Energy Utilisation, Gothenburg, Sweden (1979). Proceedings, pp. 253-282.

[67] Newman, J.N.: The excitation force on fixed bodies in waves. *Journal of Ship Research*, Vol.6 (3), 1962, pp. 10-17.

[68] Newman, J.N.: The interaction of stationary vessels with regular waves. 11th. Symposium on Naval Hydrodynamics, London, UK (1976). Proceedings, pp. 491-501.

[69] See e.g. Papoulis, A.: Op. Cit., pp. 213-215.

[70] Ibid., pp. 198-201.

[71] Olson, H.F.: *Dynamical analogies*, 2nd. edition, D. Van Nostrand Co., 1958.

[72] Falnes, J. and McIver, P.: Surface wave interactions with systems of oscillating bodies and pressure distributions. *Applied Ocean Research*, 1985, Vol. 7, No. 4, pp. 225-234.

[73] Brendmo, A.: Waves. Dokumentasjon og brukerveiledning. Technical report, NTH, Trondheim, 1992.

[74] Lillebekken, P.M.: Strålingsresistans og tilleggsmasse til svingende vannsøyle i bølgetank. Technical report, Institutt for fysikk, NTH, Trondheim, 1993.

[75] Falnes, J.: Surge excitation force vector and radiation impedance matrix for a rigid-piston model of a double OWC in a wave channel. Technical report, AM 87 - 05, School of Mathematics, University of Bristol, 1987.

[76] Falcão, A.F. de O., Pontes, M.T., Sarmento, A.J.N.A. and Jacob, J.M.Q. de B.: Demonstration Wave Power Plant in the Azores: Preliminary studies. World Renewable Energy Congress, Reading, UK (1990).

Appendix A

Uncertainty and error calculation

A.1 Uncertainty in measurements

The water depth have been varying about 0.005 - 0.010 m from day to day during the experiements. This is of negligible significance for dispersion. However, it has caused the submergence of the barrier wall, and hence, the effective length of the water column to undergo the same absolute variation. This, in turn, has caused the resonance frequency ($\omega_0 \approx 3.1$ rad/s) to vary. The reconance frequency is approximately given by the expression $\omega_0 = \sqrt{g/l}$, where $l \approx 1$ m is the effective length of one water column. The variation in ω_0 then becomes $\Delta\omega_0 = \omega_0 \Delta l/(2l) \approx 0.016$ rad/s, a relative variation of less than 1 %. Since our measurements are performed at frequencies relatively far from reconance, we regard this source of uncertainty to be insignificant.

Two pressure transducers have been used throughout the experiments, also in the case of a single OWC. Hence, the difference between the two measurements in the single-chamber case, has been used to estimate the uncertainty involved. On this basis, a relative error of 5 % has been assumed in the twin-chamber case.

Variations in results between apparently similar runs of the incident wave experiment, give reason to believe that the conditions in the flume have not been completely stationary. This means that the time elapsed from the start of the wavemaker to the start of data acquisition, may have been an important parameter in the experiments. The exact phase of the incident wave when the acquisition starts, may also have mattered. There are several possible reasons for such non-stationary conditions. Firstly, the wavemaker itself may induce long-lived transients during startup. Secondly, the oscillations in the OWCs create a radiated wave which also needs a certain time to develope to a stationary state. Another phenomenon which may cause such problems, is cross waves in the flume (see appendix B). Because of the chosen wave period and the small flume width in setup B, cross waves have probably been a minor problem in this case, compared to setup A. However, the radiated wave from the OWCs contains higher harmonics which may give rise to a certain amount of cross waves in any case. A comparison of the elevations measured with the gauges 3 and 4 at setup B (figure 2.5), shows a certain difference between the incident wave measured at the left and right side of the flume (see figures A.1 and A.2). This difference may be partly due to cross waves, but is probably also a result of the nonsymmetrical near-field part of the wave radiated from the OWCs.

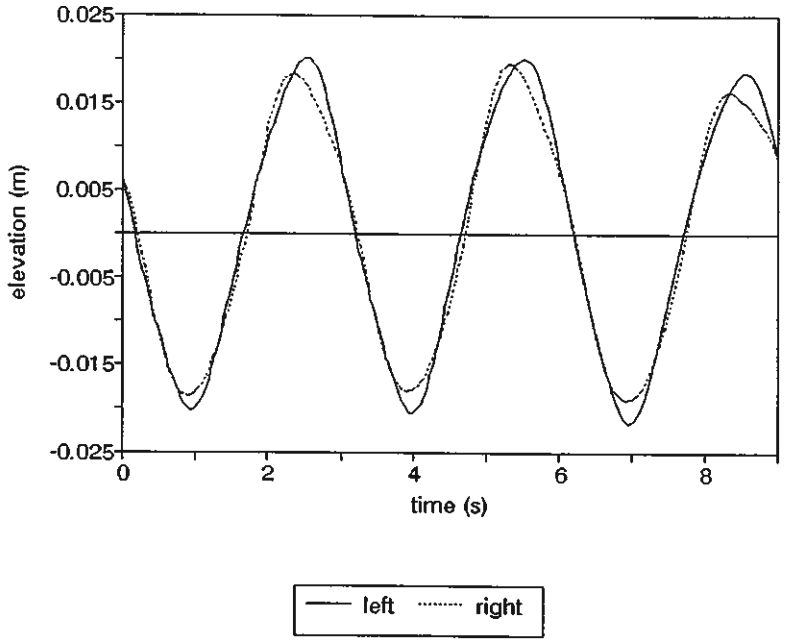

Figure A.1: Elevation of the incident wave measured near the endwall flush with the OWC mouth, and a quarter of a flume width from the left and right sidewalls, respectively (cf. wave gauges no. 3 and no. 4 in figure 3.4.).

Cross waves have probably been more important during the transient wave experiments, since then principally all wave frequencies will be present in the flume, due to the pressure step. This has made it difficult to obtain reliable measurements of the radiated wave. Besides, the elevation amplitude of this wave has been small, making the relative uncertainty large. For this reason, the radiated wave has not been used to calculate the excitation volume flux coefficient q_{e1}. Instead, this quantity is obtained partly on a theoretical basis (see section 3.1.2).

The dominating source of uncertainty when measuring wave elevation, is assumed to be the surface tension, which gives an absolute error of about 0.5 mm. Error due to calibration is assumed to be of minor importance in this case. In the case of the incident wave experiment, the incident and reflected waves have been calculated by a separate program, from the elevation measured by the three gauges 5, 6 and 7 [73]. In this program, the error mentioned above, as well as uncertainties in the phase, has been taken into consideration. Hence, the program has calculated the error in the incident and reflected wave, by means of ordinary error calculation methods. These calculations give an absolute error of about 0.5 mm in both the incident and reflected wave. Further, this leads to a relative uncertainty of approximately 2 - 5 % in the incident power, and about 5 - 20 % in the absorbed power, depending on the absolute value of the incident power, as well as the performance of the OWC. The uncertainty in the absorption width and the pneumatic capture width is found to be in the range of 5 - 20 % and 2 - 10 %, respectively.

The volume flux has been derived from measurements of the water elevation in the

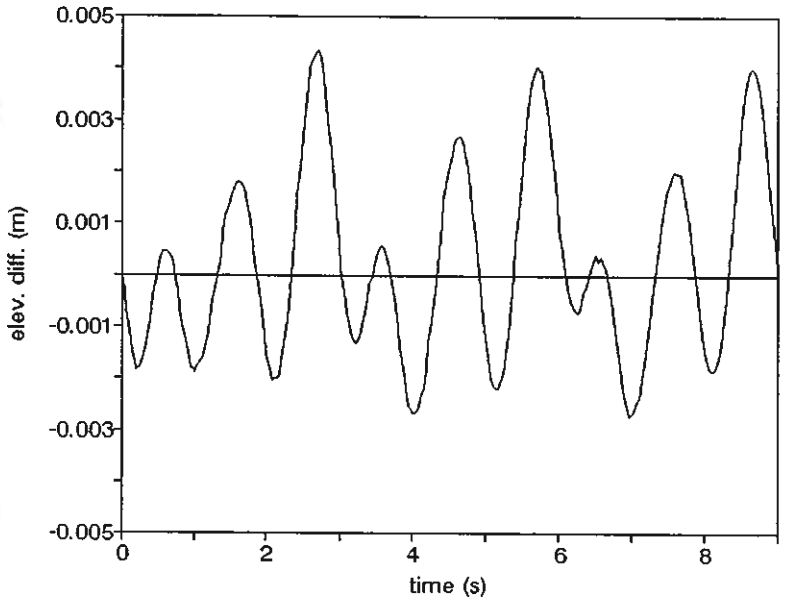

Figure A.2: Difference between elevations measured a quarter of a flume width from the left and right sidewalls, respectively. That is, $\eta_3 - \eta_4$, where η_3 is the elevation measured with gauge no. 3, and η_4 is the elevation measured with gauge no. 4 in figure 3.4.

chambers, using the expression $Q_k = S_k ds_k(t)/dt$. This expression does give the correct result only if the surface oscillate as a horizontal rigid piston. If, however, standing waves occur on the interior surface, and the location of the wave gauge does not coincide with a node, these waves will contribute to the measured chamber excursion. They do not, however, result in a net volum flux of air in the chamber. Hence, such waves may lead to an error in the derived pneumatic power (see appendix B). In the incident wave experiment, when phase control is applied, such interior modes may be excited every time a valve opens or closes, because the pressure steps contain all frequencies. FFT analysis of the chamber excursions show, however, that there is almost no oscillations present at these interior mode frequencies. Hence, the occasional sloshing which has been observed during the experiments, is probably a result of transients occuring only in short periods after the opening and closing of the valves. In the case of the transient wave experiment, such irregular behaviour of the interior surface has only been important for large initial chamber pressures. The interior oscillations mentioned here, should be regarded as additional error sources when considering the measurements of the chamber excursions. An estimate based on visual observations suggests that the total absolute error in these measurements is about 3 mm.

The relatively large uncertainty in the obtained experimental results for absorption widths and capture widths, as well as the poor reproducibility, have made it impossible to determine the sensitivity of the power output with respect to the valve operation instants. In other words, we do not know to what extent the valve control instants have to be changed in order to produce significant changes in the power output.

A.2 Error calculations

It is here shown how the absolute error in the quantities involved have been computed by means of the general expression of standard deviation,

$$\Delta f = \sqrt{\sum_{i=1}^{n} \left(\frac{\partial f}{\partial x_i} \Delta x_i \right)^2} \tag{A.1}$$

where $f = f(x_1, x_2, ..., x_n)$. The symbol Δ here denotes an absolute error, while δ means a relative error.

Uncertainty in measured quantities:

Elevation outside the chambers (no. 3-7):	$\Delta\eta = 0.5$ mm
Elevation in the chambers: (no. 1-2)	$\Delta\eta_k = 3$ mm
Dynamic pressure in the chambers:	$\delta p_k = 0.05$

Uncertainty in converted quantities:

The values and uncertainties in the incident and reflected wave have been derived by means of a computer program [73]. The error calculation formulas which are used in this program, are equivalent to those shown below. Including the uncertainty in the calibration factors, we have found that the absolute error in the incident wave and the reflected wave are, respectivily: $\Delta\eta_i = 0.5$ mm, $\Delta\eta_{r,I} = 0.5$ mm.

Incident energy transport:

$$\Delta J = \frac{\rho g^2 D}{2\omega} |\hat{A}| \, \Delta|\hat{A}| \tag{A.2}$$

Power absorbed from the waves:

$$\Delta P = \frac{d\rho g^2 D}{2\omega} \sqrt{(|\hat{A}| \, \Delta|\hat{A}|)^2 + (|\hat{\eta}_s| \, \Delta|\hat{\eta}_s|)^2} \tag{A.3}$$

Absorption width:

$$\Delta d_{abs} = 2d \frac{|\hat{\eta}_s|}{|\hat{A}|} \sqrt{(\Delta|\hat{\eta}_s|)^2 + \left(|\hat{\eta}_s| \, \Delta|\hat{A}|/|\hat{A}| \right)^2} \tag{A.4}$$

Pneumatic capture width:

$$\Delta d_{pn} = \frac{1}{T_{reg} J} \sqrt{(\Delta W_{pn})^2 + (W_{pn} \Delta J/J)^2} \tag{A.5}$$

In the single-chamber case, the average pneumatic power is given by the expression $P_{pn}(\omega) = \hat{Q}(\omega)\hat{p}^*(\omega)/2$, where $Q(t)$ and $p(t)$ are assumed to be approximately sinusoidal time functions. Hence, we may derive the relative error in the average pneumatic power:

$$\delta P_{pn} = \sqrt{(\delta p)^2 + (\Delta s/|\hat{s}|)^2} \tag{A.6}$$

where p and s is the pressure and the excursion in the chamber, respectively.

In the double-chamber case, the time functions can no longer be regarded as sinusoidal functions, so we calculate the uncertainty from the time series:
Pneumatic power at instant t_i:

$$\Delta P_{pn,i} = S_k \sqrt{\sum_{k=1}^{2} [(u_{k,i}\Delta p_k)^2 + (p_{k,i}\Delta u_k)^2]} \tag{A.7}$$

where u_1, u_2, p_1 and p_2 are time functions. The index i indicates instant t_i, and k is the column number. In this calculation we assume that Δu_k is significant only when the oscillation of the surface changes its direction, that is, when u_k is zero. This follows from the assumption that the only significant error source in this variable, is the surface tension. At every other instant, the uncertainty in the pressure is assumed to dominate.

From the results with setup A, no time-series has been available for the present study, and an approximate uncertainty in the pneumatic power is calculated by equation (A.6). Then the amplitudes in the one-chamber case are replaced with the standard deviations multiplied by $\sqrt{2}$.

The uncertainty in the vertical velocity of the surfaces in the chambers (when u_k is zero) is:

$$\Delta u_k = \sqrt{2}\,\Delta \eta_k / t_s \tag{A.8}$$

where η_k is the elevation in chamber no. k and t_s is the sampling period.

The uncertainty in the accumulated pneumatic work during the registration period is:

$$\Delta W_{pn} = t_s \sqrt{\sum_{i=1}^{N} (\Delta P_{pn,i})^2} \tag{A.9}$$

where $P_{pn,i}$ is the pneumatic power at instant t_i, and N is the number of samples.

The uncertainty in the load conductance in the single-chamber case is:

$$\Delta G_{nl} = \frac{\omega S_k}{|\hat{p}|} \sqrt{(\Delta s)^2 + (|\hat{s}|\,\Delta|\hat{p}|/|\hat{p}|)^2} \tag{A.10}$$

Appendix B

Cross waves in a flume and internal oscillation modes in an OWC

Cross waves may exist in a flume, provided that $n\lambda \leq 2d$ (see (B.7)). Here, n is a positive integer, λ is the wavelength, and d is the flume width. This means that cross waves are very likely to occur in the wider flume in setup A. In setup B, we should expect no cross waves to arise if the flume width is smaller than half the wavelength. As seen from table B.1, this means that cross waves should not occur if $T > 2.44$ s. However, due to the phase control, the wave radiated from the model contains several higher frequency components. These wavelengths may satisfy the inequality (B.7), and cross waves may thus be possible.

The cross waves affect the radiation admittance, and hence, the energy absorption of the system. Using the rigid-piston description, the counterpart of the radiation admittance is the radiation impedance (which includes the radiation resistance and the added mass). P.M.Lillebekken has measured how these parameters vary with the wave period in the tank at setup A [74]. He has also carried out theoretic calculations based on a work by Falnes [75], for comparison. An extract of these results are included in the figures B.1 - B.3. As shown in these figures, the hydrodynamic parameters vary most drastically at frequencies close to the cross wave modes, that is, when $n\lambda \approx 2d$.

In a wave flume, a progressive wave in the x direction (along the flume) will be of the form

$$\hat{\eta}_i = (Ae^{-ik_y y} + Be^{ik_y y})e^{-ik_x x} \tag{B.1}$$

Here, $k_x^2 + k_y^2 = k^2$, and the angular repetency $k = 2\pi/\lambda$ is the solution of the dispersion equation: $\omega^2 = gk\tanh(kh)$. The wave potential may be written

$$\hat{\Phi} = -\frac{g}{i\omega}e(kz)\hat{\eta}_i \tag{B.2}$$

where

$$e(kz) = cosh(kh - kz)/cosh(kh) \tag{B.3}$$

The boundary conditions on the flume walls are $\partial\hat{\Phi}/\partial x = 0$ where $x = \pm d/2$, and d is the flume width. This results in

$$k_y = \frac{n\pi}{d} \tag{B.4}$$

where n is a non-negative integer. Hence,

$$k_x = \sqrt{k^2 - (n\pi/d)^2} \tag{B.5}$$

In order to have a propagating wave in the x direction, k_x have to be real and non-zero, which gives

$$k > n\frac{\pi}{d} \tag{B.6}$$

or, equivalently,

$$d > n\frac{\lambda}{2} \tag{B.7}$$

where λ is the wavelength. This means that if the flume width is smaller than half the wavelength, the inequality (B.7) is satisfied only for $n = 0$. This mode corresponds to a wave with no variation in the x direction, that is, no cross waves can exist in the flume.

The first five cross wave modes for both wave flumes are given in table B.1.

Table B.1: Cross wave modes represented by their corresponding wave periods in seconds.

n	Setup B	Setup A
1	2.44	3.58
2	1.57	2.53
3	1.27	2.07
4	1.10	1.79
5	0.98	1.60

Most of the time it is a reasonable assumption to regard the interior water surfaces in the chambers as massless, rigid pistons. However, it is possible that standing waves may arise on these surfaces, provided that the boundary conditions are satisfied on the chamber walls. Following the same line of arguments as above, we define:

$$k_m = m\frac{\pi}{d_x} \tag{B.8}$$

$$k_n = n\frac{\pi}{d_y} \tag{B.9}$$

$$k_{nm} = \sqrt{k_m^2 + k_n^2} \tag{B.10}$$

where n and m are positive integers, and d_x and d_y are the the horizontal extensions of one chamber in the x and y direction, respectively. Further, k_m and k_n are the corresponding angular repetencies. Inserting k_{nm} into the dispersion equation, we have

$$\omega_{nm} = \sqrt{g k_{nm} \tanh(k_{nm} h)} \tag{B.11}$$

The corresponding internal resonance periods are given by

$$T_{nm} = \frac{2\pi}{\omega_{nm}} \tag{B.12}$$

The wave period of the incident wave will rarely or never fulfil the condition $T = T_{nm}$. However, the opening and closing of the valves will cause the chamber pressure to resemble a step function in short periods. This will temporarily excitate several higher frequencies in the chambers. Hence, we conclude that such interior oscillations may be present to some extent, as long as discrete phase control is applied.

The periods of the first interior modes are given in table B.2. Because of the almost quadratic cross section of the chambers (x: 0.496 m, y: 0.500 m), the corresponding modes in each direction have approximately equal resonance periods.

Table B.2: Wave periods (in seconds) of interior oscillation modes.

n m	0	1	2	3
0	-	0.800	0.566	0.462
1	0.796	0.671	0.534	0.450
2	0.564	0.533	0.475	0.421
3	0.460	0.448	0.420	0.388

Another type of interior oscillations, appearing as short transients, may result from the operation of the air valves. Each time a valve opens or closes, the dynamic pressure closely resembles a step function in a short time interval. Hence, essentially all frequencies will be excited. Even though only the frequencies satisfying the boundary conditions mentioned above will last as standing waves, other frequencies may exist as short-lived disturbances.

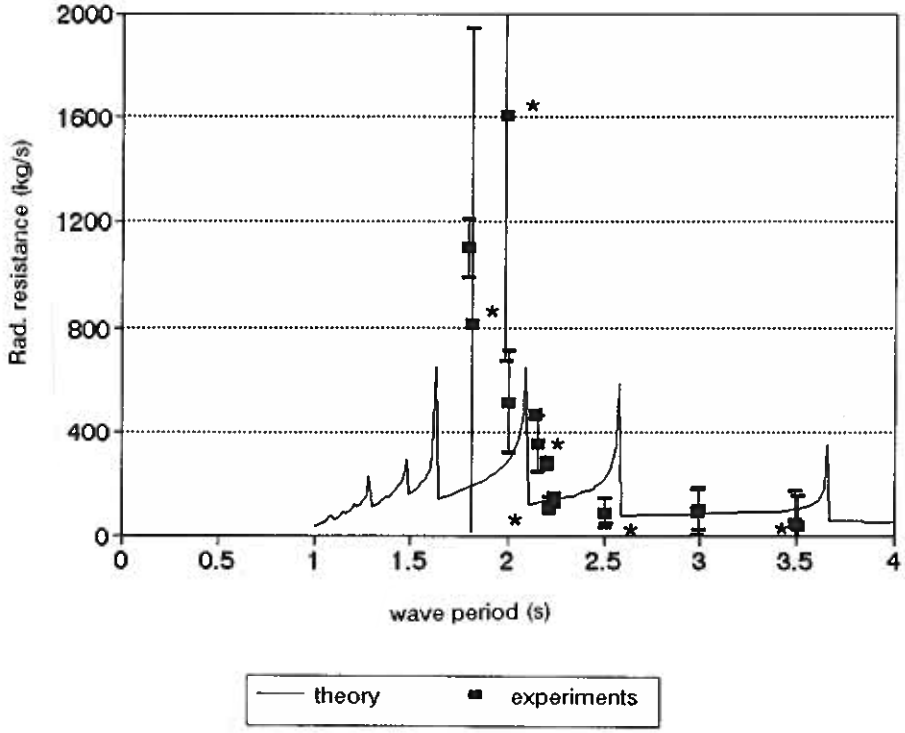

Figure B.1: Experimental and theoretical radiation resistance. No losses are included in the theoretical results. The experimental results are from setup A, and are marked with points in the figure. The theoretical results are marked with a continuous line. Uncertainty is marked with bars.

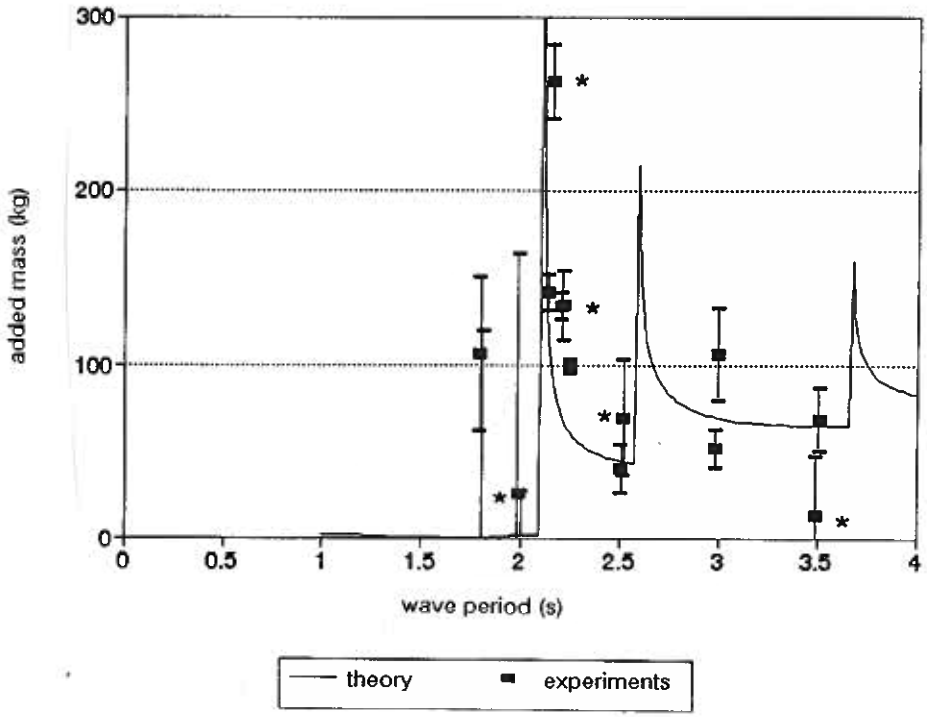

Figure B.2: Experimental and theoretical added mass. Experimental results from setup A. Uncertainty is marked with bars.

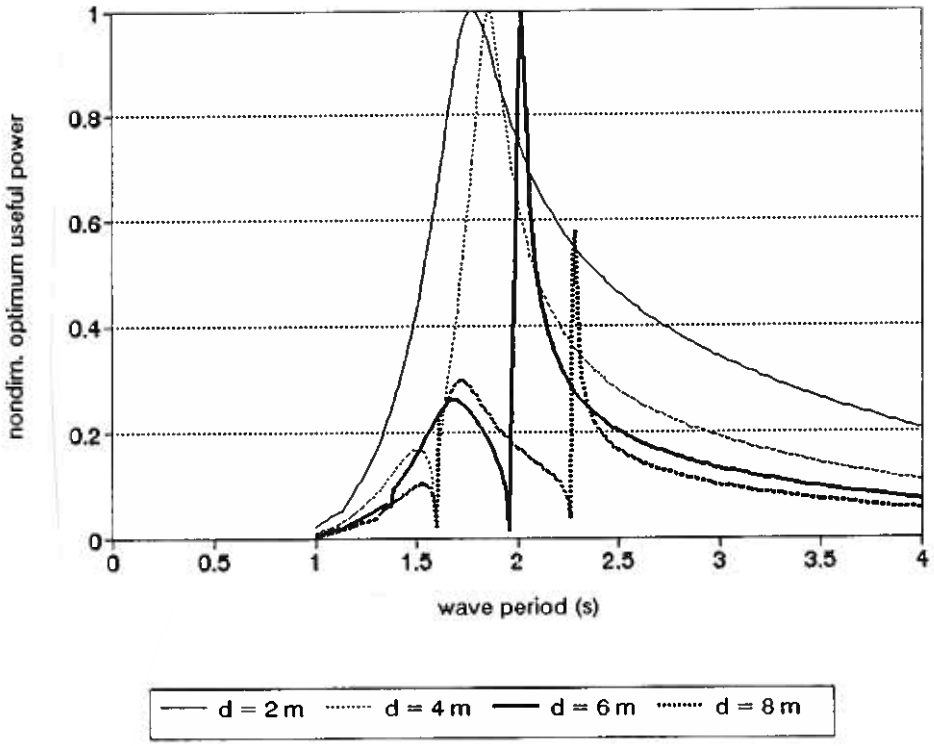

Figure B.3: Normalised optimum energy output (energy output/incident energy). Theoretical results for a symmetrically placed model in a wave flume of width d.

Appendix C

Load conductance

The expressions presented here, regard the single OWC. In the twin-chamber case, the quantities involved may be expressed by means of vectors and matrices. However, due to the discrete phase control, the quantities will not be harmonic functions. This makes the relations more complicated, and it will no longer be possible to derive the load admittance simply by means of complex amplitude considerations. This complication is, as we shall see, also true for the single-chamber case, if the load damper is nonlinear.

C.1 Linear damper

C.1.1 In the frequency domain

Assuming a linear damper, that is, the load admittance $\Lambda(\omega)$ is not a function of $\hat{p}(\omega)$, the volume flux through the turbine may be expressed

$$\hat{Q}(\omega) = \Lambda(\omega)\hat{p}(\omega) \tag{C.1}$$

where, for a given ω, the load admittance Λ is a complex number, which may be written

$$\Lambda(\omega) = G_l(\omega) + j\omega\frac{V_0}{\gamma p_a} \tag{C.2}$$

The imaginary part is a result of air compressibility, and follows from the linearisation of the adiabatic equation $pV^\gamma = const.$ The real part G_l, which is due to the power take-off, e.g. a turbine, is here termed the *load conductance*. Further, $V_0 = 0.322$ m^3 is the average volume of the air chamber, $\gamma = C_p/C_V = 1.4$ is the adiabatic constant (the ratio of specific heat with constant pressure, C_p, to that of constant volume, C_V), and $p_a = 101.3$ kPa is the absolute atmosphere pressure. It has been assumed that heat conduction is negligible. For a 3.0 s wave period, we have $\omega = 2\pi/3$ rad/s, and hence, $Im\{\Lambda\} \approx 0.0048$ m^3/(s kPa). The load conductance is typically in the range of 0.1 - 2 m^3/(s kPa) for the 1:10 model scale experiments. Hence, the imaginary part may be neglected in the present work.

For the single-chamber case, we have (see section 2.2.2):

$$\hat{Q} = S\hat{u} = j\omega S\hat{s} \tag{C.3}$$

where $S = S_1 + S_2$ is the total area of the interior oscillating surface. Assuming the hydrodynamic relations to be linear, we may write

$$|\hat{Q}| = \omega S|\hat{s}| \propto |\hat{p}| \tag{C.4}$$

Hence,

$$G_l \approx |\Lambda| = \frac{|\hat{Q}|}{|\hat{p}|} = const. \tag{C.5}$$

that is, G_l is independent of $\hat{p}$.

C.1.2 In the time domain

Transforming equation (C.1) into the time domain, we obtain

$$Q(t) = \lambda_l(t) * p(t) \tag{C.6}$$

where $\lambda_l(t)$ is the inverse Fourier transform of $\Lambda(\omega)$. Hence,

$$\lambda_l(t) = \frac{1}{2\pi}\int_{-\infty}^{\infty}(G_l(\omega) + j\omega\alpha)e^{j\omega t}\,d\omega = \frac{1}{2\pi}\int_{-\infty}^{\infty}G_l(\omega)e^{j\omega t}\,d\omega + \alpha\frac{d\delta(t)}{dt} \tag{C.7}$$

Here, we have substituted $\alpha = V_0/\gamma p_a$ in order to increase readability. The load conductance G_l may in general be some function of ω. It is reasonable to assume that this function approaches zero for high frequencies. If we make the rough simplification that G_l is a non-zero constant for $-\omega_m < \omega < \omega_m$, and zero otherwise, we may write

$$\begin{aligned}\frac{1}{2\pi}\int_{-\infty}^{\infty}G_l(\omega)e^{j\omega t}\,d\omega &\approx \frac{G_l}{2\pi}\int_{-\omega_m}^{\omega_m}e^{j\omega t}\,d\omega \\ \approx \frac{G_l}{2\pi}\int_{-\infty}^{\infty}e^{j\omega t}\,d\omega &= G_l\delta(t)\end{aligned} \tag{C.8}$$

Combining the equations (C.7) and (C.8) with (C.6), we obtain the approximation:

$$Q(t) \approx G_l p(t) + \frac{V_0}{\gamma p_a}\frac{dp(t)}{dt} \tag{C.9}$$

where the last term may be neglected in our scaled-down model experiments.

A reasonable value for the limit angular frequency ω_m may be obtained by requiring that the wavelengths for accoustic waves should be much larger than the typical dimensions of the orifice.

A linear damper may be constructed for experimental purposes, either by means of a rotating device, or simply by letting the air pass through a suitable energy-absorbing material [76]. If the pressure amplitude is not to large, a Wells turbine may also be considered to be a linear damper.

C.2 Nonlinear damper

For the sake of experimental simplicity, orifices have been used as load damping in the present work. These are, however, nonlinear elements. Hence, the volum flux through the orifice, $\hat{Q}$, is not a linear function in $\hat{p}$. In fact, we have [50]:

$$Q_{or}(t) = \mu d_b^2 C_b \frac{p(t)}{\sqrt{|p(t)|}} \tag{C.10}$$

Here, μ is a factor depending on the orifice, d_b is the orifice diameter, $C_b = (\pi/4)\sqrt{2/\rho_a} \approx 1.02 \times 10^{-3}$ $m^{3/2}kg^{-1/2}$, ρ_a being the air density, and $p = p_2 - p_1$ is the pressure drop through the orifice. The factor μ (which is typically in the range of 0.6 to 1.0, depending on orifice geometry and streaming conditions) is determined by calibration as described below [51].

The instantaneous orifice power may be derived from equation (C.10):

$$P_{or}(t) = Q_{or}(t)p(t) = \mu d_b^2 C_b |p(t)|^{3/2} \tag{C.11}$$

Considering a single OWC with no phase control, and assuming that the orifice diameter is small, the pressure may be considered to be approximately sinusoidal:

$$p(t) = |\hat{p}|cos(\omega_0 t) \tag{C.12}$$

Equation (C.10) then gives

$$Q_{or}(t) = \frac{\mu d_b^2 C_b}{\sqrt{|\hat{p}|}} \frac{cos(\omega_0 t)}{\sqrt{|cos(\omega_0 t)|}} \tag{C.13}$$

If, on the contrary, the orifice diameter is large, the volume flux may be considered to be approximately sinusoidal, while the chamber pressure is defined by equation (C.10). In the general case, both the chamber pressure and the volume flux will be nonharmonic functions.

C.3 Calibration of the orifices

At MTS, the orifice coefficient was calibrated by means of a separate experiment carried out as follows [51]: The system was run as a single OWC without any phase control. The incident wave amplitude was small, in order to ensure the oscillating interior surface to be smooth and horizontal. This was checked visually. The excursion and the dynamic pressure in the chamber were measured, and the air volume flux through the orifice, $Q_{or}(t) = S\,u(t)$ was derived (air compressibility is neglected). Then $\mu(t)$ was determined from the expression

$$\mu(t) = \frac{|Q_{or}|}{d_b^2 C_b \sqrt{|p_{or}|}} \tag{C.14}$$

which follows from equation (C.10). The average value of the resulting time-series is usually close to 0.7. The calculated average value was used in the experiments at setup A. At setup B, we have for simplicity assumed $\mu = 0.7$ throughout the entire experiment.

Calibration by means of wind tunnell experiments, would probably provide for more accurate determination of the orifice coefficient. However, equipment for this type of calibration has not been available.

Appendix D

Orifice energy

In addition to the pneumatic capture width, previously mentioned in section 2.2.1, we may also introduce an *orifice capture width* defined as

$$d_{or} = W_{or}/(JT_{reg}) \tag{D.1}$$

where W_{or} is the accumulated orifice energy during the registration period T_{reg}. This quantity may be derived by integrating the orifice power in equation (C.11):

$$W_{or} = \int_0^{T_{reg}} P_{or}dt = \mu d_b^2 C_b \int_0^{T_{reg}} |p_{or}|^{3/2} dt \tag{D.2}$$

The difference between W_{pn} and W_{or} is the energy lost through the valves. As argued in section 2.3.3, this quantity should resemble the energy losses found in equation (2.77). For many runs, however, it turns out that the measured difference between W_{pn} and W_{or} differs significantly from the value found in eq. (2.77). Hence, this difference is assumed to be largely a result of measurement uncertainty. Because of this, we have chosen to present only one of these quantities in our results. In addition to the uncertainty in the chamber volume fluxes (see section A), there may be a considerable error in the orifice factor μ (see appendix C). The calibration results in a time-series, suggesting that μ is a function of time. The theory also assumes certain simplifications, i.e. that the pressure drop is small. In reality, μ may vary somewhat with the volum flux. This causes an error in the orifice power. During the experiments at NHL, μ was simply assumed to be equal to 0.7 (see appendix C). Hence, we regard the uncertainty in W_{or} to be the larger, and the results presented in the main text of this report are given in terms of the pneumatic capture width d_{pn}.